Summer 2019

Design and characterization of a strong positron source at the MSTR beam port

Raed Atiah Alsulami

Department: Nuclear Engineering and Radiation Science

DESIGN AND CHARACTERIZATION OF A STRONG POSITRON SOURCE AT THE MSTR BEAM PORT

by

RAED ATIAH ALSULAMI

A DISSERTATION

Presented to the Faculty of the Graduate School of the

MISSOURI UNIVERSITY OF SCIENCE AND TECHNOLOGY

In Partial Fulfillment of the Requirements for the Degree

DOCTOR OF PHILOSOPHY

in

NUCLEAR ENGINEERING

2019

Approved by:

Shoaib Usman, Advisor

Joseph Graham, Co-Advisor

Carlos Castano

Ayodeji Alajo

Safwan Jaradat

ABSTRACT

For many years, slow positron sources have found uses in diverse fields including medical physics, nuclear physics, biology, surface science, exotic atom research and space science. The purpose of this work is to design and optimize a reactor-based positron source at the Missouri University of Science and Technology Reactor (MSTR) beam port and quantify its intensity. Monte Carlo simulations using the MCNP6 code were used to model the positron production and moderation processes at the MSTR beam port. The thermal neutron flux at the beam port was determined experimentally and used in the source definition of the radiation transport simulations. The source comprised a Cd (n,γ) converter with a tungsten foil grid acting as both pair production target and positron moderator. This work provides rigorously calculated moderator efficiency tabulations for tungsten foil moderators over a relevant range of positron energies and incidence angles. To optimize the positron source for MSTR, slow positron extraction yields were simulated over a range of foil thickness, grid lengths, foil-to-foil pitch sizes, and extraction voltages. A 3 cm in length by 0.2 cm in pitch tungsten grid with 10 μm thick foils was found to maximize the rate of positron extraction in an extraction potential range of 100 to 300 V while longer and narrower grids are more efficient at higher extraction potentials. In its current core configuration, the MSTR would provide a comparatively weak source of positrons. However, several methods for increasing positron yield are suggested including: reconfiguring the core, increasing reactor power, and placing the positron source inside the beam tube.

ACKNOWLEDGMENTS

I would like to thank the King Abdulaziz City of Science and Technology (KACST) program for providing graduate tuition and financial support for my PhD program.

I would like to thank my advisor Dr. Shoaib Usman for his support and guidance during my research. I am also grateful to my co-advisor Dr. Joseph Graham for his tremendous efforts, excellent cooperation, valuable guidance and support through my study. Dr. Joseph Graham guided me and provided me with the tools that I needed to choose the right direction to complete my dissertation.

I would also like to thank my dissertation committee members: Dr. Ayodeji Alajo, Dr. Carlos Castano and Dr. Safwan Jaradat for their input and valued comments throughout the project.

I also would like to thank my family for their support and continued patience during my studies. My success would not be possible without them. Finally, there are my friends and I am grateful to them for supporting me and encouraging me to complete my dissertation. I would like to thank my friend Mubarak Albarqi for supporting me during my research.

TABLE OF CONTENTS

Page

LIST OF ILLUSTRATIONS

LIST OF TABLES

1. INTRODUCTION

1.1. OVERVIEW

In 1920 Paul Dirac formulated a relativistic quantum mechanical theory for electrons and other spin ½ particles encapsulated within the famous Dirac Equation. In 1930, in order to rationalize a seemingly absurd consequence of his Equation – that there are an infinite number of negative energy electron states at every point in the universe – Dirac postulated that such states were filled in accordance with the Pauli Exclusion Principle forming a so-called "Dirac sea" of electrons. The background negative charge that this sea creates can be ignored in other electrodynamics calculations by choosing appropriate boundary conditions. Excitation of a filled negative energy level would produce an unoccupied negative energy state (analogous to a hole in semiconductor physics) which would behave like an electron in most respects apart from having a positive rather than negative charge. This quasi-particle was named a positron. Later on, with the advent of quantum field theory, the Dirac sea concept would be abandoned and the positron would be understood as the antimatter companion of the electron arising as a fundamental excitation of the same spinor field rather than as a quasi-particle "hole". The positron has the same mass and spin (½) as the electron but opposite charge and magnetic moment [1].

The positron was experimentally observed in 1932 by Charles D. Anderson in his cloud chamber experiments [2]. In 1933, Blackett and Occhialini observed electron-positron pair production from cosmic rays [3]. High energy photons can transform into short lived electron positron pairs. The lifetime of such virtual pairs is limited by the

Heisenberg uncertainty principle. In the presence of a strong electric field however, the electron positron pairs can exchange momentum and energy with the electric field to obey the conservation of energy and momentum thus becoming stable matter antimatter pairs. Such a strong field can typically only be found next to the nucleus of a high-Z element though other charged particles (e.g. atomic electrons) as well as manmade fields (e.g. lasers) can also mediate pair production. Therefore, positrons can be produced when high energy photons interact with dense matter. The minimum energy of the photon that can transform into an electron-positron pair is 1.022 MeV. This is exactly the sum of the rest mass energies of the electron and positron (511 keV each).

Positrons are also created through β+ decay of certain radionuclides. In contrast to pair production, which is a consequence of quantum electrodynamics only, β+ decay occurs due to the weak force. The process can be written as

$$p \rightarrow n + \beta^+ + \nu_e \tag{1}$$

Equation 1 is not energetically favorable for an isolated proton and therefore never occurs on its own. β+ decay is energetically favorable for proton rich nuclei and for certain even A nuclei near the stability line in the chart of the nuclides (e.g. ^{64}Cu).

$$^A_Z X \rightarrow {}^A_{Z-1}X + \beta^+ + \nu_e \tag{2}$$

Being closely related to the same underlying weak process, β+ decay and electron capture are competitive decay modes with positron emission tending to dominate for lower mass nuclei and electron capture tending to dominate for higher mass nuclei. Thus positron emission is most often observed in light proton rich nuclei.

In isolation, positrons are stable particles. When injected into matter, the positron quickly finds an electron and annihilates with it forming annihilation photons. Electron-

positron annihilation is the inverse process of pair production. Most often, two annihilation photons are formed approximately 180° apart from each other although three photon and higher order processes can also rarely occur [4]. The two-photon annihilation process can be described by the reaction

$$e^+ + e^- \rightarrow 2\gamma \quad (1)$$

The probability of annihilation depends on the local electron density while the angular correlation of the annihilation photons is sensitive to the electron momentum distribution in matter [5]. These two facts make positrons unique probes of the atomic scale structure of many materials.

1.2. USES OF POSITRONS

Positrons have been used in many applications in the fields of medicine, physics, chemistry and material sciences [6, 7]. In medical physics, positrons are used in Positron Emission Tomography (PET) to image cancerous tumors. PET is an imaging technique that detects annihilation photons from positrons emitted by a radiotracer molecule [8]. In solid state physics, materials science and organic chemistry, Positron Annihilation Spectroscopy (PAS) is used to characterize small volume defects such as vacancies and nanometer sized voids, as well as electron band structure and bonding arrangements. PAS is one of the most important non-destructive techniques for atomic level structure [9-11]. Figure 1.1 compares PAS with other microstructural characterization techniques used in materials research [12]. PAS is complimentary to other techniques in that it can probe a wide variety of sub-nm features from surface scale to macroscopic depths.

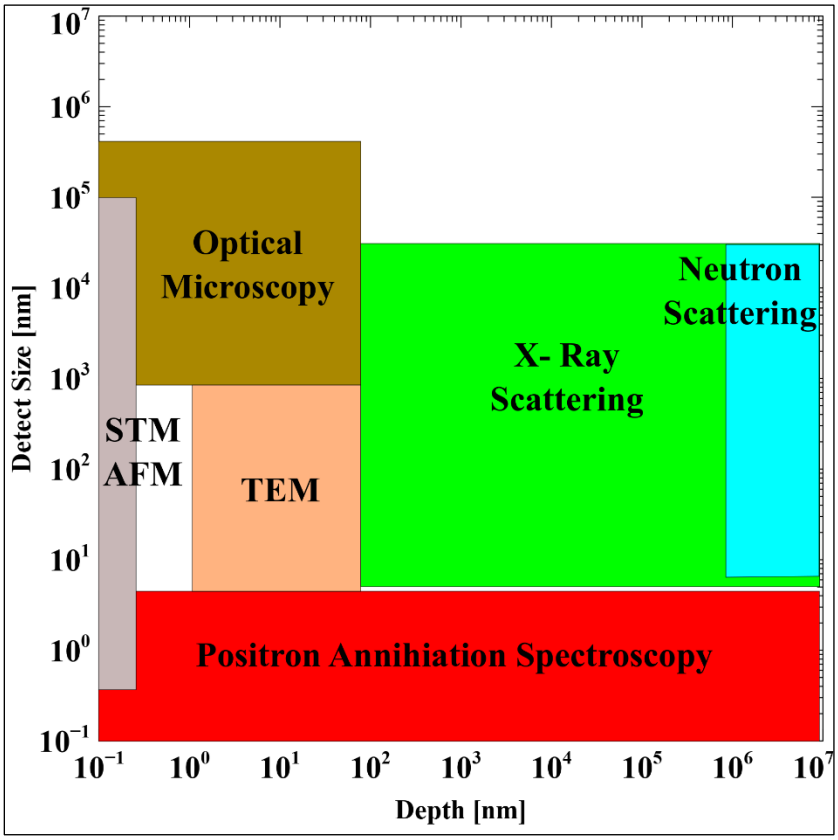

Figure 1.1. The Comparison Between PAS and Other Techniques [12].

PAS encompasses a number of different techniques that all rely on detecting annihilation photons emitted from electron positron annihilation events in the specimen of interest. The three major PAS techniques are: Positron Annihilation Lifetime Spectroscopy (PALS), Doppler Broadening of Annihilation Radiation (DBAR) and Angular Correlation of Electron Positron Annihilation Radiation (ACAR). DBAR and ACAR relate to the momentum distribution of electrons in matter while the Positron Lifetime technique gives information about the electron density [3].

Since the rate of electron positron annihilation goes as the density of electrons (and positrons) a positron tends to survive longer in open volume defects such as

vacancies, voids and pores. Different components of the positron lifetime can be measured using two detectors with high timing resolution set up in a start stop timing circuit. Histograms of timing events are used in PALS to determine the relative concentrations of various defects.

ACAR makes use of the fact that electrons in matter are not truly stationary but rather reside in orbitals with some momentum distribution. The annihilation photons are not emitted at exactly 180° but rather at nearly 180° with some small angular deviation that accounts for conservation of electron and positron momentum. Such angular deviations can be used to obtain information about a material's electronic structure.

The same electron momentum effects that give rise to small angular deviations in annihilation radiation also results in slight Doppler broadening of the 511 keV annihilation photons. In DBAR, a high energy resolution detector (e.g. high purity germanium) is used to measure changes in the amount of Doppler broadening. This information can also be correlated with the presence of defects in the material.

1.3. POSITRON PHYSICS

As mentioned above, positrons have the same mass as electrons but with opposite (positive) charge. In matter, positrons are short lived and annihilate through interaction with electrons usually producing two 511 keV γ-rays [1, 4]. When energetic positrons are implanted in a material they undergo a similar scattering and stopping processes as electrons. A beam of fast positrons incident a material can undergo backscattering or else be transmitted or stopped within the material. Two important factors that affect backscattering and transmission are the thickness of the material and the atomic number

of the material [3]. Positrons that stop undergo a combination of radiative (Bremsstrahlung) and inelastic collisions in the form of positron impact ionization, excitation or electron hole production and plasmon scattering. These processes contribute to the radiative and electronic stopping powers. The stopping process occurs within 10^{-11} which is shorter than the mean lifetime of positrons (10^{-9}-10^{-10} s) [13, 14]. A stopped positron comes into thermal equilibrium with the electrons and nuclei of the system. The energy distribution of stopped positrons can be approximately described by the Boltzmann distribution at the temperature of the material. In fact, the positron, being a fermion, should be described by Fermi-Dirac statistics but the density of positrons in ordinary matter is taken to be extremely low. At this point the positron is termed a thermal positron. Thermal positrons subsequently diffuse in matter through positron-phonon interactions.

The positron implantation profile or the positron depth profile is defined as the probability that a positron is slowed to thermal energies as a function of depth from the surface of a material. A theoretical description of the positron depth profile is given by the Makhovian profile [15]:

$$p(E,z) = \frac{m\,Z^{m-1}}{Z_o^m} \exp\left(-\left(\frac{Z}{Z_o}\right)^m\right) \tag{4}$$

Z is the distance from the surface. A typical parameterization of the Makhovian profile uses m=2. Z_o is the depth of the profile maximum (the mode of the distribution). It is related to the mean implantation depth $\bar{Z}$ by

$$\bar{Z} = \frac{\sqrt{\pi}}{2}\, Z_o = AE^n \tag{5}$$

A is a constant that depends on the density of the material, E is the incident positron energy and n =1.62. A typical approximation for A is

$$A \sim \frac{40 \text{ nm keV}^{-n} \text{ g cm}^{-3}}{\rho} \tag{6}$$

ρ is the density of material [13].

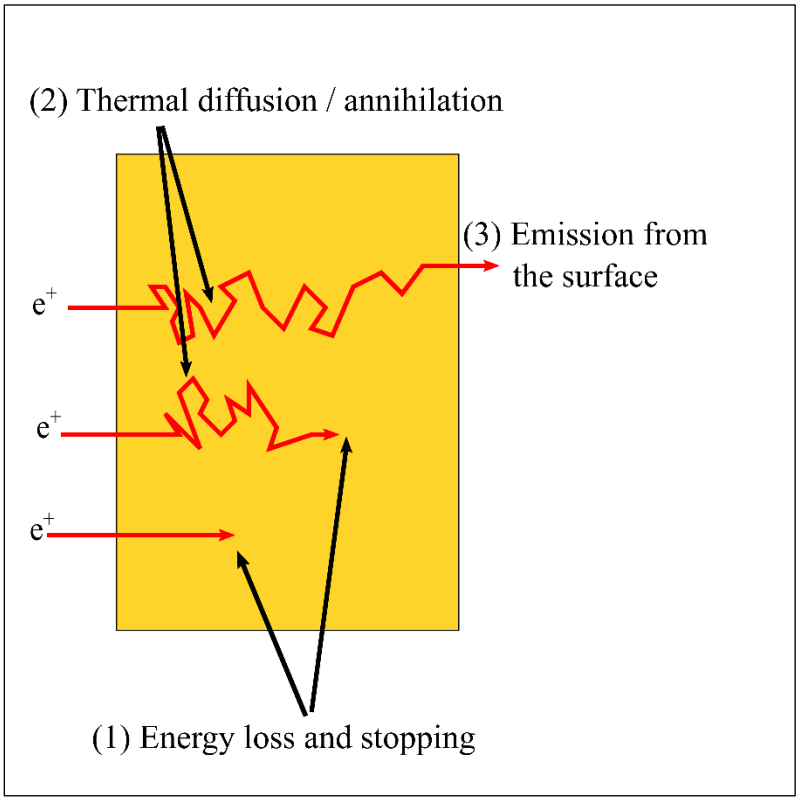

Figure 1.2. The Process of Positron Moderation.

The thermalized positron has one of two fates. Except in exceptionally thin materials, most thermal positrons will encounter an electron and annihilate. A small fraction of positrons may diffuse to a free surface and be emitted (see Figure 1.2). The rate of positron diffusion and annihilation is encapsulated through the positron diffusion

length, L_+. This length measures the mean distance a positron is able to diffuse before annihilating. L_+ is related to the positron diffusion coefficient, D_+, and mean lifetime, τ, through the following formula [16]:

$$L_+ = (\tau\, D_+)^{\frac{1}{2}} \tag{7}$$

The diffusion length depends on the material in question and amount of defect within the material.

A positron moderator is a material or device which is designed for the specific purpose of slowing down positrons to thermal energies and re-emitting them from the surface as slow positrons. Fast positrons are difficult to control and steer [17]. Slow positrons are easier to control than fast positrons because one can more easily ignore the initial velocity contributions in their trajectories. Charged particles are controlled using either electrostatic devices, magnetostatic devices or a combination of both. The Lorentz force is

$$\boldsymbol{F} = q(\boldsymbol{E} + \boldsymbol{v} \times \boldsymbol{B}) \tag{8}$$

In order to control charged particles with electrostatic devices, the electric field portion of the Lorentz force must be large enough that the velocity component(s) due to work done by the electric field is large compared to the initial velocity of the positron. Thus for fast positrons with energies on the 100 keV to 10 MeV scale, impractically large electric fields are needed to control the motion of the charged particle. Although magnetic fields cannot do work on charged particles, the velocity dependence in the magnetic component of the Lorentz force makes magnetostatic devices well suited to deflecting and focusing charged particles. For non-monoenergetic and non-monodirectional fast charged particles, however, the same term gives rise to a wide range

of forces which result in many uncontrolled particle trajectories. For this reason, magnetostatic devices are unsuitable for controlling fast positrons, unless those positrons are already monoenergetic and monodirectional (i.e. positron beam). For positron sources it therefore becomes useful to first moderate the positrons to low energies. Subsequent extraction and acceleration with electrostatic devices can be used to define a mostly monoenergetic and monodirectional beam, after which magnetostatic optics can be used for bending and focusing.

At the surface of the moderator, or indeed any material, the positron will undergo one of three fates (in addition to annihilation): (1) it is emitted into the vacuum by the work function of the material, (2) it combines with an electron forming a neutral positronium atom which may also escape into the vacuum, (3) it becomes trapped in a surface state. The definition of the positron work function in solid is the lowest energy required to remove a positron from a point inside the solid to point in the vacuum [10, 18]. It is like the definition of the work function for electrons apart from the difference in sign. The positron work function ϕ_+can be described as a sum of a surface and a bulk terms [18]

$$\phi_+ = -\Delta - \mu_+ \tag{9}$$

Δ is the surface dipole energy and μ_+ is the internal chemical potential (Fermi level) of a positron. The surface dipole energy originates from the electric double layer that forms on the surface when electrons spill out into the vacuum. The expression for ordinary electrons is similar apart from a positive sign in front of the dipole energy term. The presence of the negative dipole term in Equation 9 is significant in that it allows the positron work function to be negative when the dipole energy is larger than the chemical

potential. When the work function is negative, spontaneous positron emission from the surface is possible. Figure 1.3 shows the energy levels of a positron and electron within a metal surface. In the case of the electron, the work function is always positive, meaning that it will take energy to remove electrons from the metal surface. In accordance with the photoelectric effect an energy quanta equal to the work function will just enough energy to liberate the electron but give it no kinetic energy. In the case of the positron, if the work function is negative, the positron is able to spontaneously fall down the potential energy hill into the vacuum, converting the extra work function energy , ϕ_+, into kinetic energy, typically a few eV. It is important to mention, however, that once emitted, the positron can no longer be considered a thermal positron. The velocity and energy distribution of the emitted slow positrons do not obey Boltzmann statistics.

The probability of a thermal positron being emitted from the surface increases exponentially as the positron work function becomes more negative [19]. Another possibility for the positron at the surface is that it picks up and binds to a loosely bound electron forming a positronium (Ps) atom. Positronium exists in two states: para-positronium (p-Ps) with a lifetime of 0.1244 ns and ortho-positronium (o-Ps) with a lifetime of 138.6 ns [20, 21] Since these exotic atoms are both neutral and short lived, extraction of positrons from Ps is not practical. Another possible fate for the positron is trapping at a surface image potential. When a charged particle is near the surface of a conductor, an opposite image charge forms within the conductor and creates an electric dipole field between the charge in vacuum and the image charge. The image charge does not actually exist as a particle but the notion of an image charge is useful in correctly describing the electric field within vacuum. The dipole field created by a positron in

vacuum and its image creates an attractive potential near the surface. Thus in addition to the negative work function which allows the positron to escape, a negative potential also forms just outside the surface which is also capable of trapping the positron (see Figure 1.4).

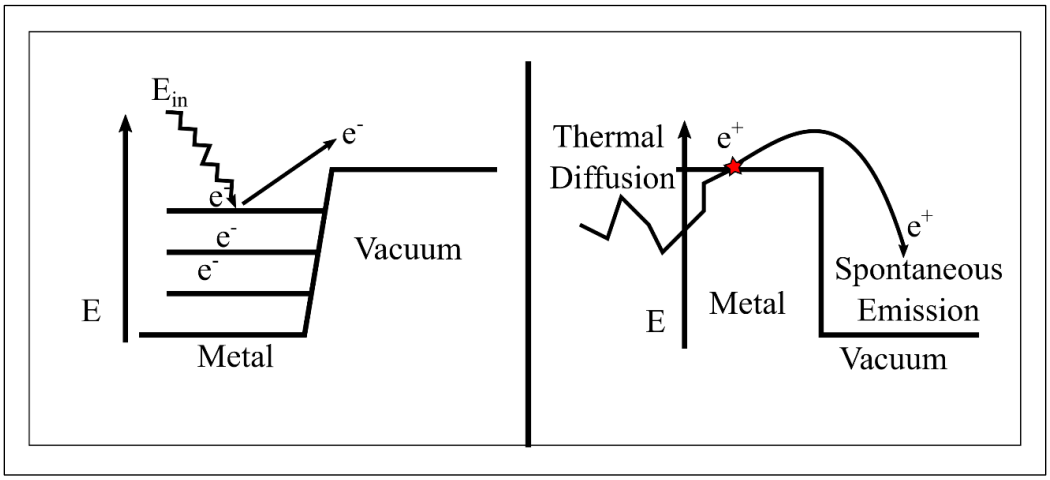

Figure 1.3. Electron and Positron with Work Function.

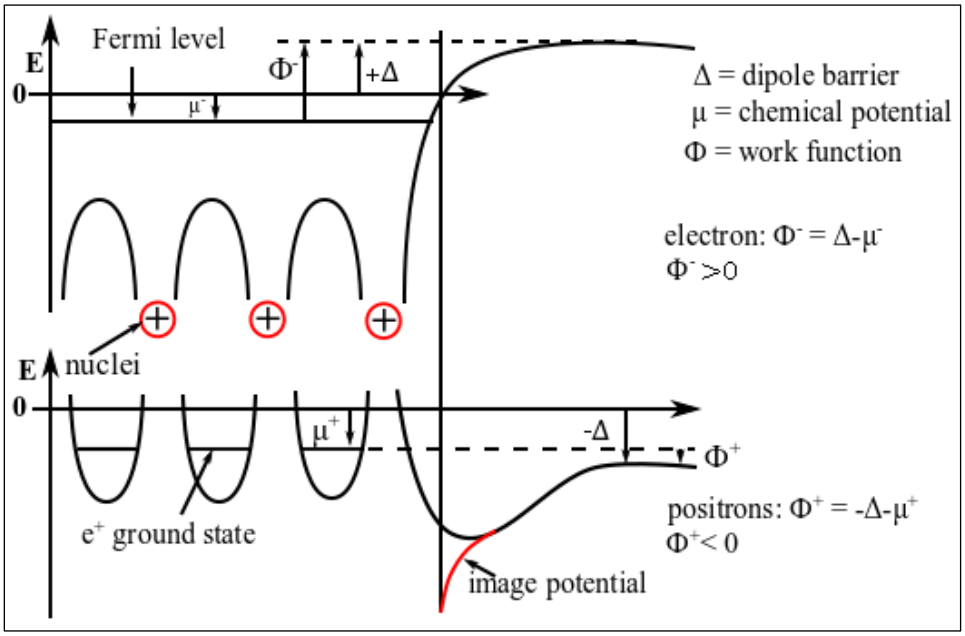

Figure 1.4. The Bulk and Surface Potential for Electrons (top) and Positrons (below) and the Negative Work Function Which Allows the Positron to Escape [22].

1.4. ARTIFICIAL POSITRON SOURCES

1.4.1. Positrons from Radioactive Sources. Positrons are produced by positive beta decay in a large number of radionuclei. Nuclei in the proton rich upper half of the chart of nuclides tend to undergo electron capture and β+ decay, though only those nuclei near the stability line have half-lives long enough to be practical. Examples of β+ emitters include ^{64}Cu, ^{58}Co, ^{22}Na and ^{18}F. Some even-odd nuclei such as ^{64}Cu can undergo both e.c./β+ and β- . Positrons are produced with a broad continuous energy spectrum rather than discrete energy spectrum [4]. This is a consequence of the kinematics of beta decay, in which energy is shared among three particles: the daughter nucleus, the beta and the electron neutrino/antineutrino. Figure 1.5 shows the positron spectrum for ^{18}F which has a typical spectrum for β+ emitters.

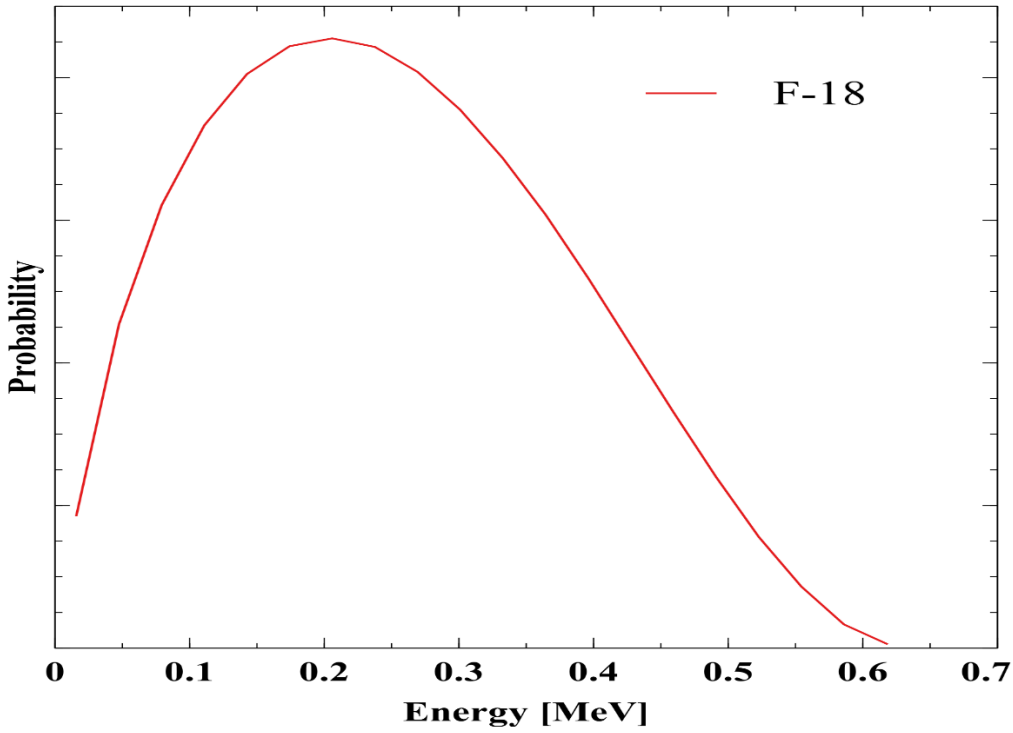

Figure 1.5. The Positron Spectrum for ^{18}F [23].

^{58}Co has been used to produce positrons for high intensity sources such as those used in positron diffraction experiments [19]. The half-life of ^{58}Co is 71 days and therefore provides a high activity source. The half-life of ^{22}Na on the other hand, is 2.6 years and is a commonly used source for PAS measurements. ^{64}Cu has a half-life of 12.8 hours and can be produced from neutron radiative capture of ^{63}Cu in a nuclear reactor. The short half-life demands that a ^{64}Cu-source must produced at a nearby nuclear reactor [14].

1.4.2. Pair Production. Positron-electron pairs are created when high energy gamma radiation (with energy greater than 1.022 MeV) is incident on high-Z elements such as W, Ta or Pt [14]. Low-Z or medium-Z elements will also produce electron-positron pairs but experience more photons losses from Compton scattering. The pair production cross section scales roughly as Z^2 [24] while the Klein-Nishina cross section scales as Z. Thus the ratio of pair production to Compton scattering increases roughly linearly with atomic number, at high energies. A photon energy greater than 1.022 MeV is required for to create positron-electron pair. This is the rest mass energy of the positron and electron system [25]. The probability of pair production increases with increasing photon energy [15]. Figure 1.6 shows the different contributions to the total photon cross section for tungsten..

Pair production it the most commonly used method for generating high-current positron beams. Two main types of pair production sources exist. The first utilizes a linear accelerator (linac) while the second uses neutrons and/or gamma radiation from a nuclear reactor.

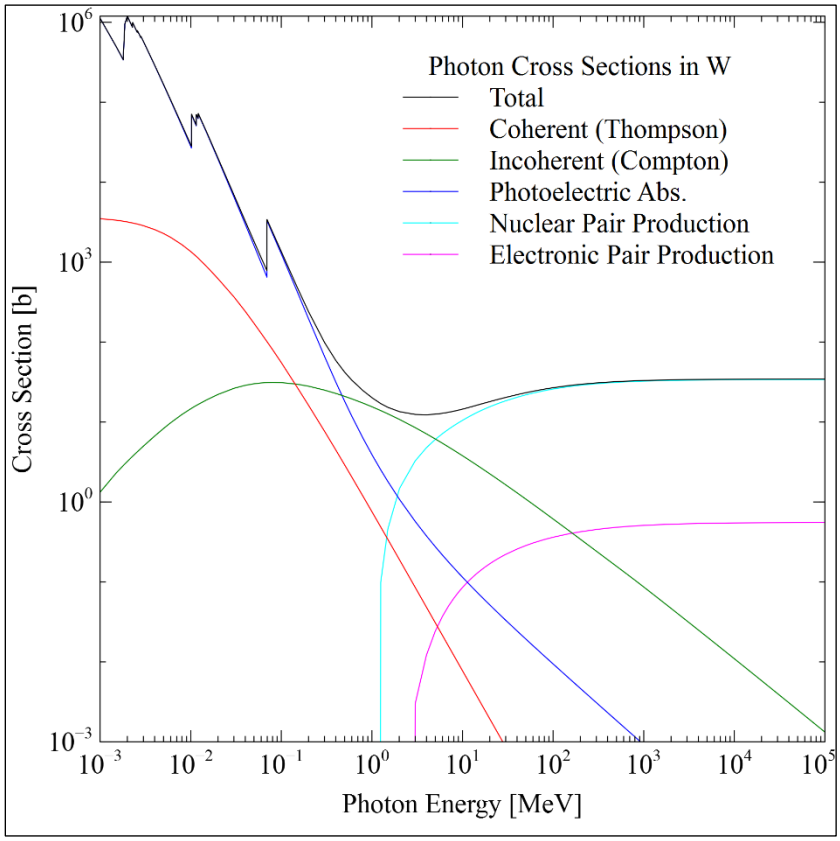

Figure 1.6. The Total Photon Cross Section for Tungsten [26].

1.4.2.1. Linear accelerator based positron sources. Positrons are produced when high-energy electrons hit a high-Z target (e.g. W or Ta). For electrons with energy above about 10 MeV, the majority of energy loss occurs through bremsstrahlung photon generation. At higher energies a greater fraction of energy radiative energy loss occurs. Moreover, the average energy of the bremsstrahlung spectrum increases with electron velocity. Typical linac electron energies used for positron production include: 100 MeV at Lawrence Livermore National Laboratory [27], 75 MeV at the Electrotechnical Laboratory in Tsukuba (Japan) [28], 40 MeV at the National Institute of Advanced Industrial Science and Technology (AIST) [29]. The ELBE facility positron source (EPOS) in Germany uses a 40 MeV electron beam [30]. The fraction of the intense

bremsstrahlung photons with energy above 1.022 MeV goes on to create positrons through pair production [31]. The fast positrons from the target can then be moderated and used as slow positrons [10]. A key distinguishing feature of linacs and other sources is the pulsed nature of linacs. Linacs tend to bunch charged particles causing them to arrive on the target at the same time.

1.4.2.2. Nuclear reactor-based positron sources. With nuclear reactor based positron sources, the supply of positrons is continuous over time. Pair production is achieved in a nuclear reactor-based positron source in one of two ways. The uses the high energy prompt gamma rays from fission directly in the pair production target. The POSitrons at the Hoger onderwijs reactor (POSH) is an example of a facility that uses this approach. At POSH tungsten foils convert high energy gamma radiation close to reactor core in electron positron pairs [32]. The second approach converts thermal neutrons to prompt gamma radiation. This is typically done using a cadmium foil which has large thermal cross section for radiative capture and produces spectrum of high energy prompt gamma rays. These gamma rays are then converted into a electron positron pairs using a high-Z material. The PULSTAR nuclear reactor at North Carolina State University is an example of a reactor-based positron source. The PULSTAR source has a cadmium foil neutron to gamma-ray converted and a tungsten foil pair production target [33]. The NEutron induced POsitron source at Munich (NEPOMUC) also uses cadmium as a neutron to gamma converter but uses a platinum pair production target [34].

The large thermal radiative capture cross section for cadmium mostly comes from the ^{113}Cd isotope. The ^{113}Cd(n, γ)^{114}Cd thermal averaged cross section is nearly 26,000

barns (20,000 b at 0.0253 eV). The natural abundance of ^{113}Cd is 12.2%. The average number of prompt photons emitted per captured neutron is 2.3. The average photon energy is 1.9 MeV [31]. The prompt gamma spectrum from ^{113}Cd is shown in Figure 1.7. More details about the design for different facilities will be discussed in Section 2.

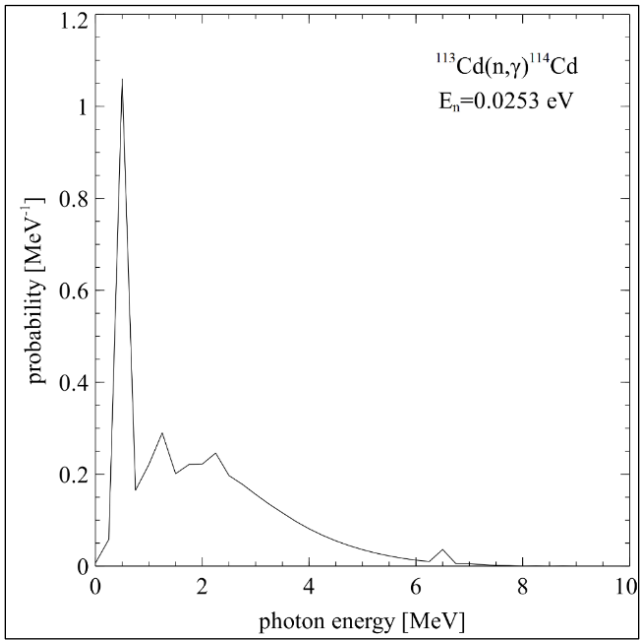

Figure 1.7. The Prompt Gamma Spectrum from ^{113}Cd.

1.5. OUTLINE OF THIS DISSERTATION

The remainder of this dissertation proceeds as follows. Section 2 reviews much of the relevant literature on slow positron sources and positron moderators. The design considerations and intensities of various strong positron sources at linear accelerators and nuclear reactors are described in Sections 2.2-2.4. Section 2.5 summarizes past and future efforts made to design, model and optimize positron moderators. Sections 3-5 present the experimental and computational modeling tasks performed in the present dissertation

work. The experimental efforts to characterize the neutron flux at the MSTR beam port is described in Section 3. This information was needed to develop a computational model of a proposed slow positron apparatus at the MSTR reactor. Section 4 describes computational methodologies developed to calculate moderation efficiencies for tungsten foils. It also presents efficiency tables that were needed to complete Monte Carlo radiation transport simulations for predicting positron yield. These simulations and optimization of moderator geometry is detailed in Section 5. This dissertation concludes with a discussion of the optimization strategies for a slow positron source and several suggestions for improving the slow positron yield at the MSTR are given.

2. LITERATURE REVIEW

2.1. OVERVIEW

There are several high intensity positron sources in the world. Some of them produce positrons by the pair production route while other facilities produce positrons by generating β+ emitting radionuclides. A very large number of benchtop positron annihilation systems use commercially available sources, though those systems and the production of those sources will not be mentioned here. As mentioned in the introduction, both nuclear reactors and linear accelerators can be used to produce positrons via pair production. Accelerators can also be used to produce large activities of short lived β+ emitting nuclei which can also integrated into positron sources. Some prominent examples of strong positron sources in the world include The Munich Intense POsitron Source (MIPOS) and The NEutron induced POsitron source at Munich (NEPOMUC) at FRM-II in Germany, high-intensity positron facility (HIPOS) in Petten in the Netherlands, the positron source at the Kyoto University Research Reactor at Japan, the slow positron beam at the NC State University PULSTAR reactor and the The POSitrons at the Hoger onderwijs reactor (POSH) facility at the TU Delft reactor in the Netherlands.

The next three subsections of this section discuss each of these technologies with particular attention paid to reactor-based pair production sources (Section 2.4). The last section discusses positron moderation.

2.2. POSITRON PRODUCTION BY ACCELERATOR-BASED TARGET ACTIVATION

Stein *et al.* [35] first tried the technique of using accelerators to activate a target and produce positrons in 1974. They use 4.75 MeV protons incident on a boron target to produce ^{11}C through a $^{11}B(p,n)^{11}C$ reaction. ^{11}C is a nearly pure β+ emitter and has a half-life of 20.4 min. Positrons with low energies were observed to be emitted from the irradiated boron target without any additional moderating materials. Later, Xie *et al.* [36], Hunt *et al.* [37] and Cassidy *et al.* [38] used deuterons to produce ^{13}N through the $^{12}C(d,n)^{13}N$ reaction. Like ^{11}C , ^{13}N is an almost pure β+ emitter but has a shorter half-life of 9.97 min.

The basic system design proposed by Hunt *et al.* proposed is shown in Figure 2.1 shows the source design. A similar system was used by Cassidy *et al.* Two diamond or graphite targets are brazed onto opposite sides of a rotating copper cooling drum. At any given time one target is facing the deuteron beam and being activated while the other is facing a tungsten moderator and the positron beamline on the opposite side. After one target is sufficiently activated the drum is rotated such that the ^{13}N nuclei may decay into the tungsten moderator on the positron beamline side. Cassidy *et al.* were able to achieve a positron intensity of 10^8 e^+ s^{-1} using 0.5 mA deuteron beam.

Before deuteron beam with currents greater than a few μA were available alternative nuclear reactions were also considered. Higher energy proton beams from cyclotrons have been used. In 1993 a compact cyclotron-based slow positron beam was developed by Sunitomo Heavy Industries (SHI) using the $^{27}Al(p,n)^{27}Si$ reaction. Though the cyclotron was compact the actual positron beam line was large (25m) and the efficiency was low [39]. In 1995, Hirose *et al.* [40] modified the slow positron source

making it more compact and giving it an intensity of $2\times10^{6}\ e^{+}\ s^{-1}$ [39, 40]. Moreover, Saito *et al.* [41, 42] designed a system based on the $^{18}O(p,n)^{18}F$ reaction with 14 MeV protons. They expected an intensity of $10^{7}\ e^{+}\ s^{-1}$.

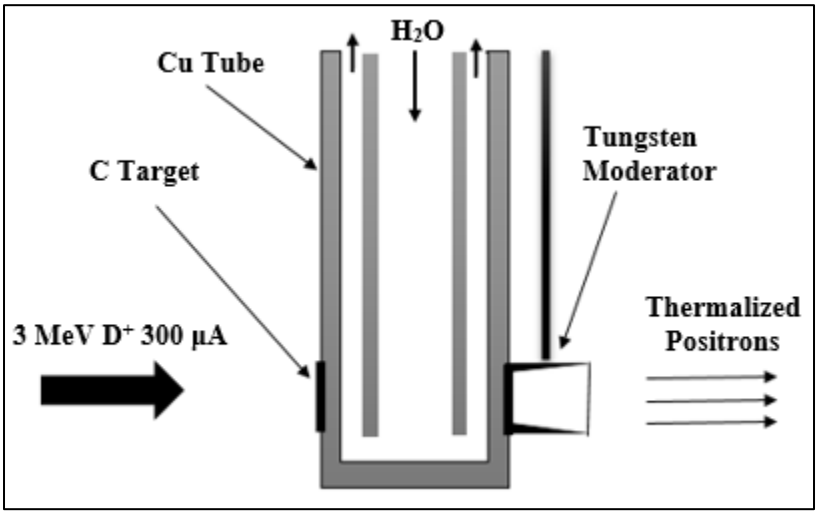

Figure 2.1. The Carbon Target Design to Produce Positrons Beam [37].

2.3. LINEAR ACCELERATOR-BASED PAIR PRODUCTION

There are several linear accelerator facilities around the with pair production sources. A pulsed linac is used for pair production in a tantalum target at Mainz University in Germany [43], the Institute of Materials Structure Science, High Energy Accelerator Research Organization (KEK) in Japan [44] and at Forschungszentrum Rossendorf near Dresden, Germany [30].

Gräff *et al.* [43] produced positrons by pair production in a tantalum foil converter by using an electron linac in an energy range from 80 to 260 MeV. Within the Ta target, electron energy is converted to bremsstrahlung radiation. The bremsstrahlung radiation is then converted into electron positron pairs. Three tungsten vanes were placed

behind the tantalum target to thermalize the fast positrons. The thickness of each tungsten vane was 25 μm. They found about 10^7 fast positrons per second could detected at an average electron current of 1 μA.

Wada *et al.* [44] experimentally modified the KEK converter and moderator for an 55 MeV electron linac positron source. They replaced the tantalum converted with titanium and used tungsten foils to moderate the positrons. They also modified the moderator geometry into a finer foil grid. They found that the modified converter and moderator improved the intensity of the positron beam.

Krause-Rehberg *et al.* [30] studied the design parameters for an intense multi-purpose positron beam using a linac producing 40 MeV electrons. A tungsten target was used for pair production. Tungsten foils were designed to moderate the positrons. In their design the electron beam passes through a stack of 50 W foils each having a thickness of 0.1 mm and separated each other by 0.1 mm to allow for cooling water to pass through the foils. The tungsten moderator was designed as foil with 30 μm thickness. They modeled the electron beam energy loss using Monte Carlo simulations.

Yamazaki *et al.* [45] also used a tantalum foil converter and tungsten moderate to generate slow positrons from an electron beam. They achieved a slow positron yield of about 10^8 positrons per second. Also, they found that the pulsing efficiency for the positron experiments was not very high due to the large energy spread of the positron beam.

Chen *et al.* [46] used computer simulations (EGS4) to optimize the geometry for positron production in a 15 MeV electron beam and studied the positron energy and angle distributions. They found that the optimum thickness of the Ta converter for that energy

is about 2.0 mm at normal incidence. Also, they also discussed using the tungsten vanes as both converter and moderator. They expect to produce 10^{10} slow positron per second and the yield of positron can improved.

2.4. REACTOR-BASED POSITRON SOURCES

An important method for producing intense beams of slow positrons utilize the neutron or gamma radiation from a nuclear research reactor. Prompt gamma rays from nuclear fission may be used directly for pair production or else gamma rays can be converted from neutrons. In some designs both neutron-to-gamma conversion and prompt gamma rays are used.

Hugenschmidt *et al.* [47] presented a new design of the neutron induced the positron source NEPOMUC in Munich to supply an intense beam of slow positrons. They used a 3 mm cadmium cup to convert thermal neutron to high energy gamma-rays. Pt foils were used to convert high energy gamma-radiation into electron positron pairs. They expect to produce a monoenergetic positron beam with an intensity up to 3 $x10^9$ e^+ s^{-1}.

Lynn *et al.* working at the High flux Beam Reactor at Brookhaven [48] proposed using a copper source instead of cadmium. The copper converter approach is unique in that it provides both prompt gamma radiation from radiative capture from ^{65}Cu (n, γ) ^{66}Cu and ^{63}Cu (n, γ) ^{64}Cu reactions and produces ^{64}Cu as well. ^{64}Cu is a β+ emitter with a 12.8 h half-life, though its branching ratio for β+ is only 17.4%. In that work, the decay of ^{64}Cu would be used as the positron source. Either the Cu(111) source or a W(110) foil could be used moderate the positrons. An advantage of using a radioactive source is that

it provides positrons even when the reactor is not operating. This does require that the source be refreshed (re-irradiated) every three days due to the decay of ^{64}Cu.

Moxom *et al.* [49] designed an intense positron beam at the North Carolina State University PULSTAR reactor (see Figure 2.2). They designed the positron beam and calculated the positron production rate using the Monte-Carlo N-Particle (MCNP) radiation transport code. Cadmium was used as a neutron-to-gamma converter. Tungsten was used as both a pair production converter and moderator. With a tungsten thickness of 0.25 mm, they estimated the positron intensity to be 5.3 $x10^{8}$ e^{+} s^{-1}. In their design they placed the positron source within one of the positron beam lines near the edge of the core to maximize the flux of neutrons and gamma rays.

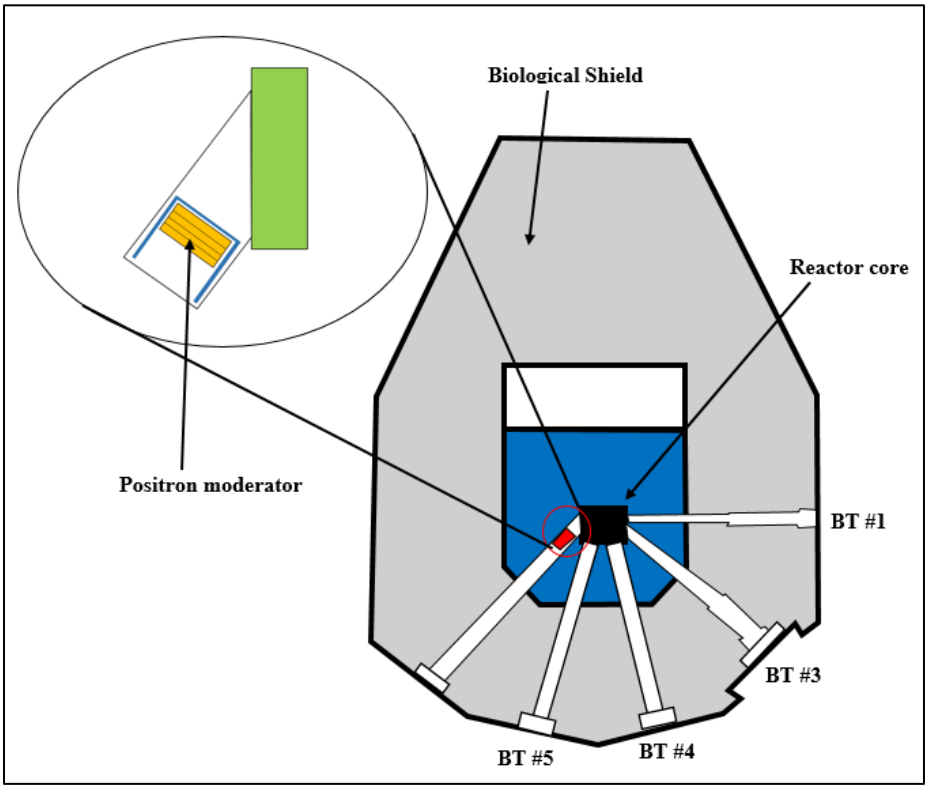

Figure 2.2. The Positron Beam at the PULSTAR Reactor [49-51].

Zeman *et al.* [52] studied the design for a high-intensity positron facility (HIPOS) at the High Flux Reactor (HFR) in Petten, Netherlands. A model for the reactor core, reflector and neutron beam tube were designed and used to calculate the photon and neutron flux. The design parameters for the source were estimated using MCNP-X and GEANT4. Their design also incorporated a cadmium converter and tungsten lattice moderator. The conversion of thermal neutrons to gamma rays was calculated and compared with MCNP-X and GEANT4. The neutron source was assumed to be monoenergetic. The tungsten lattice was rectangular instead of circular due to the limited geometry options in GEANT4. They found that the total positron current reaches a maximum at a cadmium converter thickness of 1 mm though they chose 2.5 mm due to the burn-up of cadmium. They predicted an unmoderated positron intensity of 10^{13} positrons per second.

Schut *et al.* [53] studied the damage in the tungsten converter and moderator foils at the positron source in the POSH source of Hoger Onderwijs Reactor (TU Delft, Netherland) after three years of operation. The POSH source uses 25 μm thick tungsten foils. They found that the diffusion length is reduced by factor of 2 to 3 after three years of operation indicating more positron trapping in defects. Also the S-parameter value in the near of surface region was higher than in the bulk, also indicating increased defect concentrations at the surface.

Van Veen *et al.* [54] discussed an earlier design of the POSH source. 6 mm diameter tungsten and tungsten coated copper cylinders were arranged in four 8 cm diameter disks within a 10 cm length cylinder. In this configuration, at full power the 2 MW HOR reactor was predicted to achieve 0.7×10^{8} e^{+} s^{-1} in a 10 mm beam spot.

2.5. THE TRANSMISSION AND BACKSCATTERING EFFICIENCIES FOR POSITRON MODERATORS

The moderator efficiency is an important factor in designing a strong positron source. As mentioned in the introduction it is necessary to first slow positrons before reaccelerating. Thus whether the positron source is slow, medium or high energy, positron moderation is usually used. The moderator efficiency is defined as the ratio of the number of the thermal positrons emitted from the moderator to the number of high energy positron incident on the positron moderator [55]. The positron moderator can be found in different forms such as thin films or wire meshes.

Lynn *et al.* [56] used 5000 Å thick thin films of tungsten as positron moderators with a ^{22}Na source. They observed a conversion efficiency of 4×10^{-4}. Gramsch *et al.* [57] used several thin films moderators with thicknesses between 0.3 and 7 μm with a ^{22}Na source. Their moderator efficiency ranged from 1- 9.1×10^{-4}. Zecca *et al.* [58] using tungsten and nickel moderators and a ^{22}Na source found a moderator efficiency range from $0.4\text{-}2\times10^{-6}$. Weng *et al.* [59] investigated three types of tungsten moderators with a ^{22}Na source. The first was a multi-folded W wire mesh, the second was a W(100) single crystal foil, and the last was a W polycrystalline foil. They found that the efficiency of the moderator depended on three important factors which are: the annealing pretreatments, the duration of chemical etching, and the number of layers. The wire diameter in the multi-folded mesh was 20 μm. Saito *et al.* [60] also tested a tungsten wire mesh. The wire diameter of their mesh was 10 μm. Williams *et al.* [61] compared the efficiency of wire meshes and foils for moderating a ^{22}Na source. They concluded that for the same thickness/diameter for meshes offered about 10 better efficiency than single crystal foils. It should be mentioned however, that in a pair production sources, the total

mass of tungsten is also important as it acts as a positron converter. Thus wire meshes may be optimal for radioactive sources while foils could be preferred in reactor or accelerator based sources. The calculations made by Williams *et al.* were based on a questionable approximation to the solution of the 3D diffusion Equation for positrons.

An earlier work by Vehanen *et al.* [62] used a W(l l0) single crystal as positron moderator with ^{58}Co positron source. They measured the backscattering efficiency and found it to be $(3.2 \pm 0.4) \times 10^{-3}$. Moreover, Anwand *et al*. [63] tested 9 μm thick polycrystalline tungsten foils with a ^{22}Na positron source. They found the moderator efficiency to be around 3×10^{-4}. Lee *et al.* [64] used 10 μm thick polycrystalline tungsten foils and measured a moderator efficiency around 2×10^{-4}. Reurings *et al.* [65] tested different thicknesses of tungsten with ^{22}Na positron sources. They measured moderation efficiencies in the range of 10^{-5} to 10^{-4}.

3. NEUTRON CHARACTERIZATION OF THE BEAM PORT AT MSTR

3.1. OVERVIEW

In order to develop a numerical method for predicting the performance of a slow positron source to be designed and tested at the Missouri University of Science and Technology Reactor (MSTR), it is necessary to first estimate the intensity of the proposed source. This dissertation investigates the possibility of installing a compact slow positron source in the beam port opening of MSTR. Unlike other designs which place the source at the end of the neutron beam tube near the fuel, it is desirable to develop a movable or modular positron source that can be removed from the beam port opening freeing up space for other neutron beam experiments. MSTR has only one neutron beam port. It is therefore important that the beam line has multi-use functionality. That said, placing the positron source further away from the core reduces the neutron flux substantially. It is therefore necessary to first estimate the positron yield in order to determine whether such a proposed facility would have sufficient strength to be of practical use.

3.2. MISSOURI UNIVERSITY OF SCIENCE AND TECHNOLOGY REACTOR

The Missouri University of Science and Technology reactor (MSTR) was built in 1961 for educational and research purposes [66]. MSTR is an open-pool research reactor that uses light water for moderation and natural convection cooling. The maximum thermal power of MSTR is 200 kW. This reactor has four control rods including a regulating rod [67, 68]. The facility has been used for different experiments such as isotope production, imaging studies, and neutron activation analysis (NAA). The MSTR contains the following irradiation facilities: a neutron beam port, thermal column, bare,

and cadmium pneumatic rabbit tubes, an isotope production element, in-core irradiation void tubes, and a moveable core access element. Experiments conducted at the MSTR beam port include measurements of dead-time for portable neutron spectroscopy and tomography imaging systems [69, 70]. Figure 3.1 shows top down view of the MSTR.

Neutron beamlines are routinely used in areas of materials science, physics and analytical chemistry [71]. Prompt Gamma Activation Analysis (PGAA) [72], and Positron Annihilation Spectroscopy [49, 73] are some examples of techniques that have been developed at beam ports of small research reactors [74]. For the purpose of designing beam port experiments and apparatus, it is necessary to know the magnitude and angular/spatial distribution of the neutron flux coming out of it. In the Oregon State University TRIGA reactor, this was measured using neutron activation of golds foils and by exposing neutron-sensitive radiograph imaging plates. The total flux and spatial distribution of neutrons at the beam opening was characterized in this way [72]. Gold foil activation and imaging have also been used to determine the neutron beam profile at other reactors [74-78]. This section describes experiments performed to characterize the neutron flux and two group energy spectrum at the MSTR beam port in its current configuration.

MSTR has one beam port protruding through the pool wall extending into a basement experimental area [68]. An evacuated aluminum beam tube 15 cm in diameter by 320 cm in length provides the path for neutrons to travel. Near the center of the tube, a 5.7 cm thick lead shield is inserted in order to attenuate the gamma flux in the basement experimental area [79]. A stainless-steel shutter assembly with a Boral-lined duct is used define a well-collimated neutron beam.

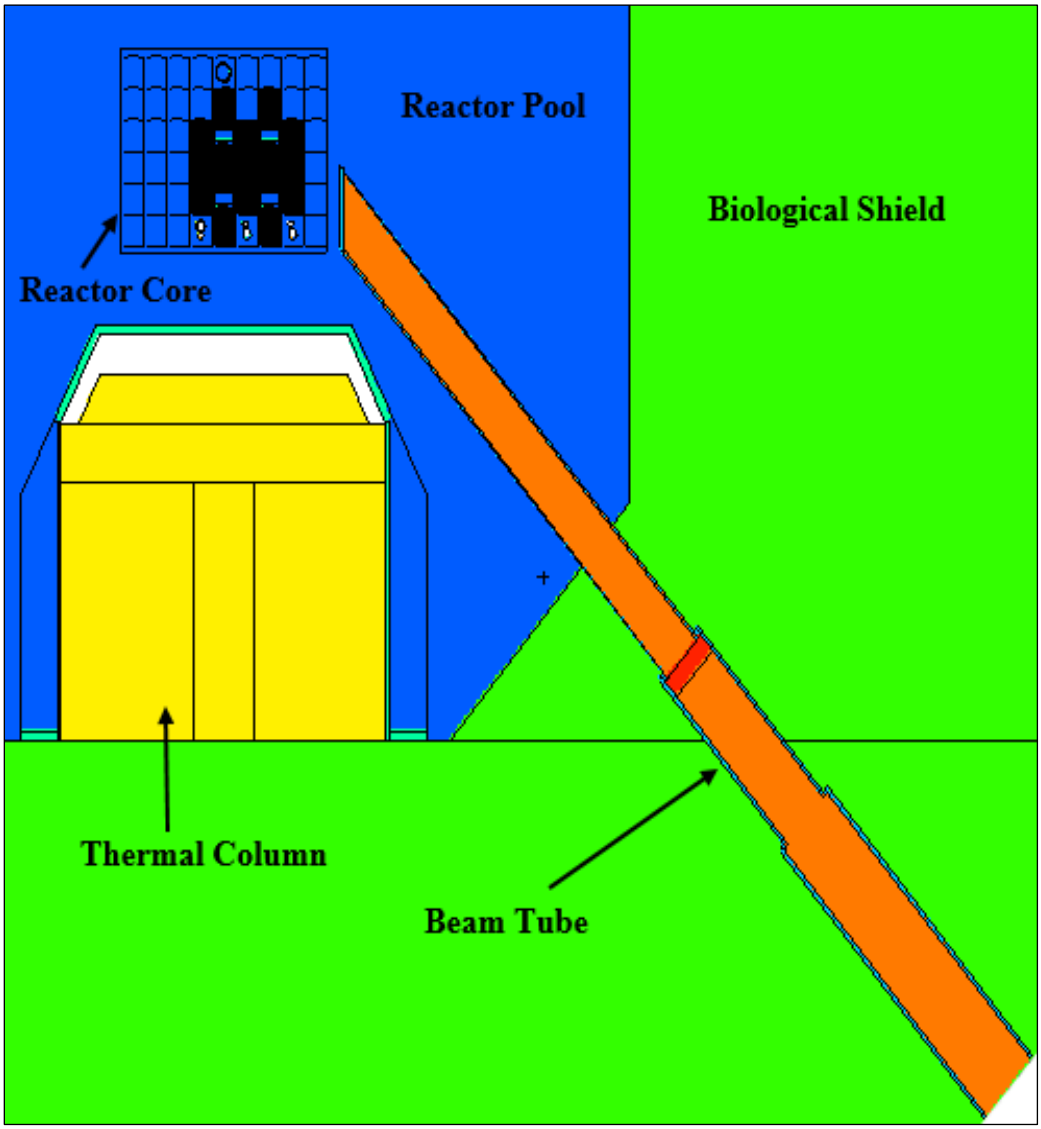

Figure 3.1. Top Down View of The MSTR.

It includes a fixed plug and a rotating shutter. The Boral-lined rectangular duct passes through both plug and shutter and has dimensions of 7 cm × 4.4 cm. The shutter assembly can be closed or opened by rotating the middle portion of the shutter assembly to cut the neutron beam path. Figure 3.2 shows the MSTR beam tube, shutter assembly and neutron beam path.

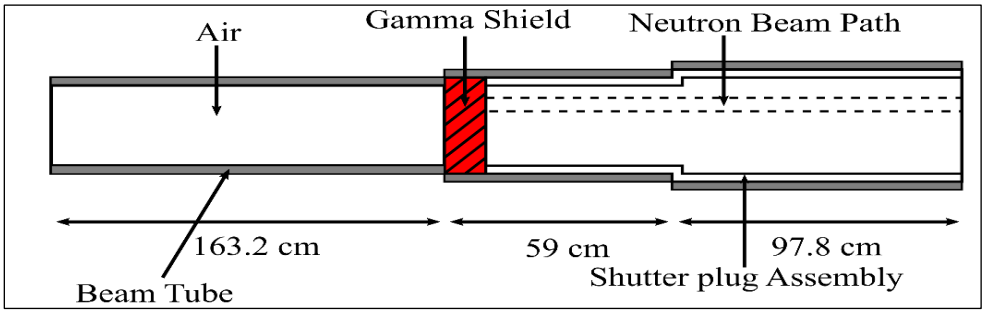

Figure 3.2. MSTR Beam Tube, Shutter Assembly and Neutron Beam Path.

3.3. CHARACTERIZATION OF NEUTRON BEAM FLUX USING NEUTRON ACTIVATION ANALYSIS

Neutron Activation Analysis is a technique that is usually used to determine the concentration of trace elements in a matrix given previous knowledge about the neutron source strength and neutron spectrum or indirectly by comparing to the activation rates for an acceptable set of similar standards. Moreover, the same process can be used to exactly characterize a neutron source given a known target, it's mass, and composition and appropriately weighted group cross sections and correction factors describing its activation [75, 80]. Techniques using activation of metallic foils, wires and solutions can be used to characterize a reactor flux [81-83]. Briefly, a flux monitor is irradiated in a neutron environment in order to activate radionuclei with decay radiations that can be quantified using standard spectroscopic methods. The neutron activation analysis technique was used to determine the thermal and epithermal neutron flux and its spatial distribution at the opening of the MSTR beam port.

3.3.1. Methodology. The neutron flux was experimentally measured by irradiating a set of high purity gold foils in the opening of the neutron beam port. The sample activity after irradiation is given by following formula

$$A(t_{ir}) = N\sigma\phi(1 - e^{-\lambda t_{ir}}) \quad (10)$$

$A(t_{ir})$ is the sample activity at the time the irradiation was finished, N is the number of target nuclei, σ is the target nuclei radiative capture cross section, ϕ is the neutron flux, λ is the decay constant of the activated nuclei, and t_{ir} is the irradiation time. The number of target nuclei, *N*, is given by the following formula:

$$N = \frac{a_i m_i N_A}{A_i} \quad (11)$$

a_i is the natural abundance of the isotope of an element, N_A is Avogadro's number, m_i is the element mass, and A_i is the isotope atomic weight. The sample activity after the sample has been allow to decay is:

$$A(t_d) = A(t_{ir})e^{-\lambda t_d} \quad (12)$$

where t_d is the decay time.The thermal and the epithermal flux were determined at the beam port of MSTR using ASTM standard E262-13 [84]. This method compares the activation rates of bare irradiated gold foils with irradiated cadmium covered gold foils to determine the thermal neutron flux at the beam port and the epithermal flux parameter. Gold is a neutron absorber. Therefore, self-shielding correction factors must be included in the flux determination. The thermal flux, ϕ_t, and epithermal flux parameter ϕ_e, are given by following formula

$$\phi_t = \frac{1}{g\sigma_t G_{th}}\left[R_b - R_{Cd}\left(1 + \frac{g\sigma_t f_1}{G_{res} I_o} + \frac{\sigma_t w'}{G_{res} I_o}\right)\right] \quad (13)$$

$$\phi_e = \frac{R_{Cd}}{I_o G_{res}} \quad (14)$$

g is the Westcott factor which accounts from ideal $1/v$ behavior of the cross section in the thermal zone. σ_t is the thermal cross section. R_b and R_{Cd} are reaction rates for a bare foil and foil with cadmium cover, respectively. f_1 accounts for $1/v$ activation in the 5kT to E_{cd} energy domain while w' accounts for non-$1/v$ behavior in the same energy range. G_{th} and G_{res} are thermal and resonance neutron self-shielding correction factors, respectively. I_o is the resonance integral. Though flux depression factors should usually be included when the activation foils are enclitic by a moderating medium, and moderation effects in present experiments are negligible due to behaved in air. Moreover, it should be mentioned that these Equations are used to calculate a two group fluxes.

While ϕ_t represents the thermal flux (i.e. the area under a Maxwellian flux curve), ϕ_e represents only a constant that parameterizes the flux energy dependence in the neutron slowing down region. In other words, the neutron flux can be approximated as ϕ_e/E above the thermal energy cutoff (about 0.5 eV) and below the fast energy cutoff (about 100 keV). Alternatively, one can think of ϕ_e as the magnitude of the epithermal flux per unit lethargy. Since the fission spectrum-averaged cross section for radiative capture in ^{197}Au (is about 51 mb).It is small compared to the resonance integral, this contribution is negligible to the epithermal flux. It was calculated to contribute to the measured value by about 2%.

3.3.2. Experimental. Gold foils were irradiated in the MSTR beam port. ^{197}Au is the only stable isotope of gold. It has a 98.7 b cross section for radiative capture (^{197}Au(n,γ)Au^{198}) [84, 85]. The large cross section for gold makes it well suited for measuring low neutron fluences. ^{198}Au has a 2.7 day half-life, β- decaying to Hg-198 and releasing a 411.8 keV gamma 96% of the time [84, 85]. Six gold foils (Shieldwerx) with 25 μm thickness were irradiated in each experiment. Table 3.1 shows the masses of each gold foil.

Table 3.1. The Masses of Gold Foils

Foil	Mass (g)
1	0.124
2	0.116
3	0.122
4	0.114
5	0.112
6	0.062

Two sets of gold foils were irradiated (see Figure 3.3). The first comprised six bare gold foils to determine the total flux. The second set of six bare gold foils was also irradiated bare but a cadmium filter was placed between the neutron beam and the foils in order to filter out the thermal neutrons. Though the ASTM standard calls for the foils being encapsulated in a Cd box, the Cd filter gives the same effect. The cadmium filter had a thickness of 1 mm If the cadmium thickness is correctly selected, it will allow most neutrons above a certain cadmium cutoff energy, E_{Cd}, to pass through and interact with

the flux monitor while most neutrons below this energy are absorbed. The cadmium thickness determines to some extent the cutoff energy, as well as the tabulated values of f_1 and w'. Moreover, it is important that the parameters of Equation (13) match the Cd thickness. In the ASTM standard, the cadmium cutoff energy is $E_{Cd} = 0.55\ eV$ for 1 mm thick of cadmium filter. Hence this is the value used in the experiment. Table 3.2 shows the cross section parameters for 25 μm thick high purity ^{197}Au for this cadmium thickness.

The irradiation positons of the foils are shown in Figure 3.3. The six foils were arranged in a 2-by-3 array in the rectangular beam port opening. For the second set of irradiations the cadmium filter was placed between the beam port opening and the gold foils. The space behind the foils in the basement experiment area was about 2 m of air, so the possibility of backscattering or moderation affecting the measurements was considered insignificant. The gold foils were irradiated at full reactor power (200 kW) for 4 hours. After irradiation, each was measured in a lead shielded High Purity Germanium Detector (HPGe, Canberra) to perform gamma spectroscopic analysis of the 411.8 keV ^{198}Au photopeak.

A multi-isotope europium source containing ^{152}Eu, ^{154}Eu, and ^{155}Eu isotopes was used to calibrate the detector efficiency as a function of energy. Canberra's spectroscopic acquisition and analysis software, PROSPECT, was used to analyze the spectra and calibration source [86].

The detector efficiency, ε, for each Eu photopeak was calculated by use following formula

$$\varepsilon = \frac{C}{\gamma A t_c} \tag{15}$$

Table 3.2. The Cross Section Parameters of 25 μm Gold Foil and a 1 mm Cadmium Filter [84, 87-89]

Parameter	Value
f_1	0.468
I_o	1550 b
w'	0.0500
G_{res}	0.539
g	1.005
G_{th}	0.991

C is the net photopeak counts, γ is the gamma-ray intensity for the photopeak, A is the source activity, and t_c is the live counting time. The dead time of the detector was below 10%. Equation (13) was used to calculate the thermal flux at each position at the beam port opening, while Equation (14) was used to determine the epithermal flux parameter at each position. The activation rate, R, for each bare and cadmium filtered gold foil was calculated by following formula

$$R = \frac{C\lambda}{N\theta\gamma\varepsilon} \tag{16}$$

$$\theta = \left(1 - e^{-\lambda t_i}\right)\left(e^{-\lambda t_d}\right)\left(1 - e^{-\lambda t_c}\right) \tag{17}$$

C is the number of 411 keV photopeak counts. λ is the decay constant for ^{198}Au and γ is the 411 keV gamma ray intensity. N is the number density of target nuclei (^{197}Au),

determined by Equation (11). ε is the efficiency interpolated to 411 keV from the Eu efficiency calibration. t_i is the irradiation time, t_d is decay time and t_c is counting time. The number of counts in the 411 keV photopeak was calculated with the following formula

$$C = G - B \tag{18}$$

$$B = \left(\frac{M}{2n}\right)(B_1 + B_2) \tag{19}$$

C is the net peak area, G is the gross counts in the region of interest (ROI) with M channels, and B is the number of continuum (background) counts in the same region of interest. The linear continuum counts,B, is determined from the sample spectrum from Equation (19). B_1 and B_2 are the sums of n continuum channels to the left and right of the ROI region, respectively. The uncertainty in the number of counts was calculated by taking the square root of the sum of the squared errors. It was propagated from the uncertainties of the gross counts and continuum counts. The majority of the uncertainty in the reaction rates is attributed to uncertainty in the efficiency calibration (about 5%) though counting statistics also contribute a few percent error. Other sources of uncertainty include dead-time correction factor; uncertainty in the irradiation, decay and count times; uncertainty in the foil mass; uncertainty in the gamma-ray intensity; and the uncertainty in the decay constant. These were all included in the uncertainty propagation but deemed to be insignificant contributors.

The thermal and epithermal flux value uncertainties were propagated from Equation (13) and Equation (14). Uncertainties in the parameters R_b, R_{Cd}, G_{res}, G_{th}, σ_t and the ratio $I_o/g\sigma_t$ were included in the error propagation as were the uncertainties on the activation rates discussed above. Some uncertainties were obtained directly from the

nuclear data (i.e. σ_t, $I_o/g\sigma_t$) while the uncertainties on G_{th} and G_{res} were estimated by determining the G_{th} and G_{res} values using ENDF/B-VII.1 data [89] along with the techniques explained in Fleming [87] and Lindstrom *et al.*[88] and propagating the uncertainties in the correction factors through the Equations reported in those references. Actually, most the uncertainty of the final flux values propagated from the experimentally determined activation rates, i.e. the uncertainty in the energy interpolation on the detector efficiency calibration curve.

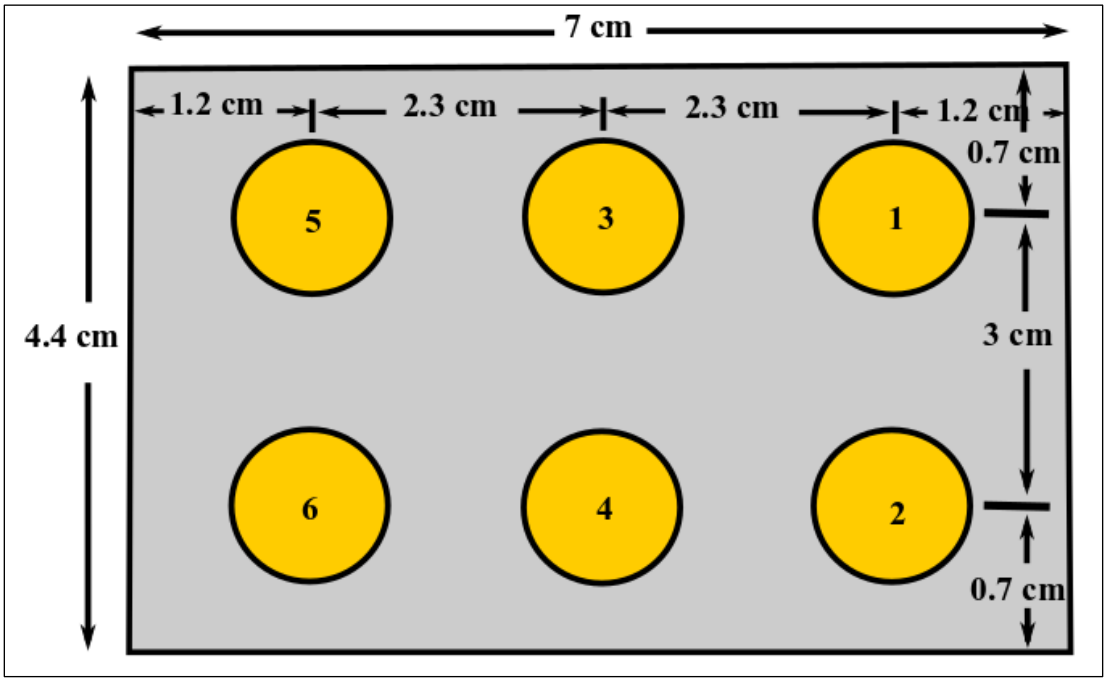

Figure 3.3. The Circles (1-6) Represent The Gold Foils Positions. The Outer Rectangle is The Rectangular Opening of The Beam Port.

3.4. MONTE CARLO SIMULATION

MCNP6 Monte Carlo models were used to simulate and calculate the neutron flux at the MSTR beam port. This was done using a combination of surface source write and read cards. The first MCNP model included the reactor core, fuel elements, control rods,

beam port, and pool water. Figures 3.1 and 3.2 show four parts in the reactor: the core of reactor, thermal column, beam port, and a beam tube.

Fresh fuel was assumed and the current core configuration was used. The ENDF/B-VI (.66c) cross-section library was used. A surface source write (SSW) card was used to write neutron histories to a surface nearer the beam port. The first model, including the whole reactor and the beam port was then simulate using the KCODE burnup and criticality card. There were 1,000,000 neutrons per cycle and 5000 cycles in the KCODE calculation discarding the first 50 cycles. Once enough particle histories were written to the SSW file, a Surface Source Read (SSR) file was created from the SSW card. To predict the flux at the experiment position, cells at the end of the beam port were modeled in a simplified geometry in the second model. The second MCNP model had only the beam tube, beam port, pool wall and part of the pool plus the surface source created from the first model. In other words, the second model treated the beam port as a fixed source problem, which greatly improves computational speed and tally convergence. Each run used approximately 10 billion particles (NPS). A F4 tally with energy binning (E card) was used to determine the neutron flux at each foil at locations matching those of the experiment. 69 energy bins were included with the flux tallies.

3.7. RESULTS AND DISCUSSION

The neutron flux results of the experimental and the Monte Carlo simulation are shown in Table 3.3. The flux values of thermal, epithermal and total (thermal+epithermal) are tabulated for each foil. The MCNP calculations were found to less than the experimental values for the thermal flux and total flux but overvalue for the

epithermal flux results. The diffrences between the experiment and the simulation is due to number of uncertainties and discrepancies between the actual core and the MCNP model. The most important factor to the discrepancies maybe is the assumption of fresh fuel in the MCNP model. To produce similar element-averaged fission rate as a fresh fuel element, due to the burnup of the actual fuel elements is required huge thermal neutron flux. Therefore, fresh fuel was assumed in the MCNP model, which underestimates the thermal neutron flux that required to obtain a specified power level. Also, at the same time, the fast flux is proportional to the fission rate, and therefore to the power, is also proportional to the thermal flux times the macroscopic fission cross section. Moreover, the ratio of the fast flux to the thermal flux decreases as neutron poisons are added and as the fuel is burnt which can be seeing in Table 3.3.

A normalized of the MCNP average flux was done to have better agreed with the average experimental flux. Figure 3.4 shown this normalization, but each foil flux was normalized by the average flux over all foils. The experiments and MCNP result has a qualitative a agreement for foils 1-5 except foil 6. After normalization was performed for the experimental and MCNP data, the relative error was 16% for foils 1-5.

Table 3.3. Experimental and MCNP Results of Neutron Flux for The Gold Foils

Foil	Exp. Thermal $\times 10^6$ cm^{-2} s^{-1}	Exp. Epi. $\times 10^5$ cm^{-2} s^{-1}	MCNP Thermal $\times 10^6$ cm^{-2} s^{-1}	MCNP Epi. $\times 10^5$ cm^{-2} s^{-1}	%Difference in total flux
1	7.9 ± 0.4	9.9 ± 0.4	5.2 ± 0.09	17 ± 1	23%
2	5.5 ± 0.3	8.2 ± 0.3	3.1 ± 0.06	9.8 ± 0.8	35%
3	7.6 ± 0.4	7.5 ± 0.3	4.1 ± 0.08	13 ± 1	34%

Table 3.3. Experimental and MCNP Results of Neutron Flux for The Gold Foils (cont.)

4	5.1 ± 0.3	6.8 ± 0.3	2.6 ± 0.05	8.1 ± 0.7	41%
5	5.0 ± 0.3	5.6 ± 0.2	2.6 ± 0.05	8.1 ± 0.7	39%
6	2.9 ± 0.2	5.6 ± 0.2	2.5 ± 0.05	8.1 ± 0.7	3%

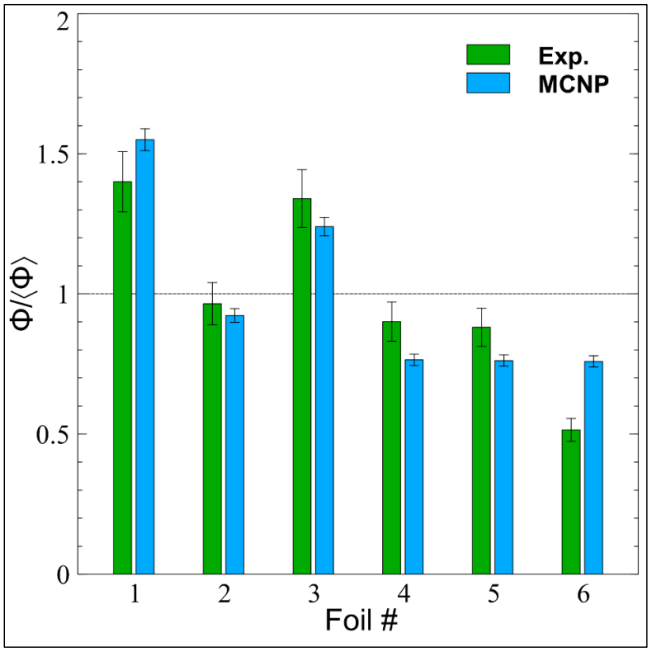

Figure 3.4. The Total Neutron Fluence per Activation Foil Normalized by The Average Fluence for All Foils.

Additional difference in the result values might be in how reactor power is defined. For the reactor power measurements of the MSTR are made with a pair of Compensated Ion Chambers positioned on either side of the core. More uncertainties in the experimental data not included in the results could include differences in the thickness foil and Cd, the duplicability of the foil positioning at the beam port opening and the flux profile differences between experiments due to neutron poison effects.

4. CALCULATION AND TABULATION OF EFFICIENCIES FOR TUNGSTEN FOIL POSITRON MODERATORS

4.1. OVERVIEW

As mentioned in the introduction, positrons produced by prompt gamma rays from neutron capture reactions tend to have a wide energy spectrum which extends from zero to several MeV. Figure 4.1(b) shows the predicted energy spectrum of positrons simulated using a rudimentary model of a neutron beam port-based positron source. The calculation was performed in the Monte Carlo of N-Particles radiation transport code, MCNP6. The majority of positrons are produced between 100 keV and 10 MeV though some can be found as low as 1 keV. In addition to the broad positron energy spectrum, the angular distribution of electron positron pairs is also broad. Radiative capture of thermal neutrons results in very nearly isotropic emission of secondary particles. Thus the flux of photons and positrons from a nuclear reactor-based positron source is broadly distributed in both energy and angle. For the purposes of extracting, focusing and reaccelerating positrons, this broad spectral and angular distribution is problematic. Fast positrons experience a much larger Lorentz force in a magnetic field than in an electric field. Therefore, magnetic focusing and steering is only a viable option for monodirectional and monoenergetic fast positrons. When the particle flux is neither monodirectional nor monoenergetic, the magnetic portion of the Lorentz force varies greatly in magnitude and direction and thus large geometric and chromatic inefficiencies are unavoidable. On the other hand, slow positrons can be more easily extracted and focused with electrostatic devices before being accelerated and controlled with magnetic lenses and other accelerator optics [10, 51]. It therefore becomes useful to slow down, or

moderate, the positrons to thermal energies. This is often accomplished using foils or wire meshes of high-Z elements such as tungsten or platinum [90].

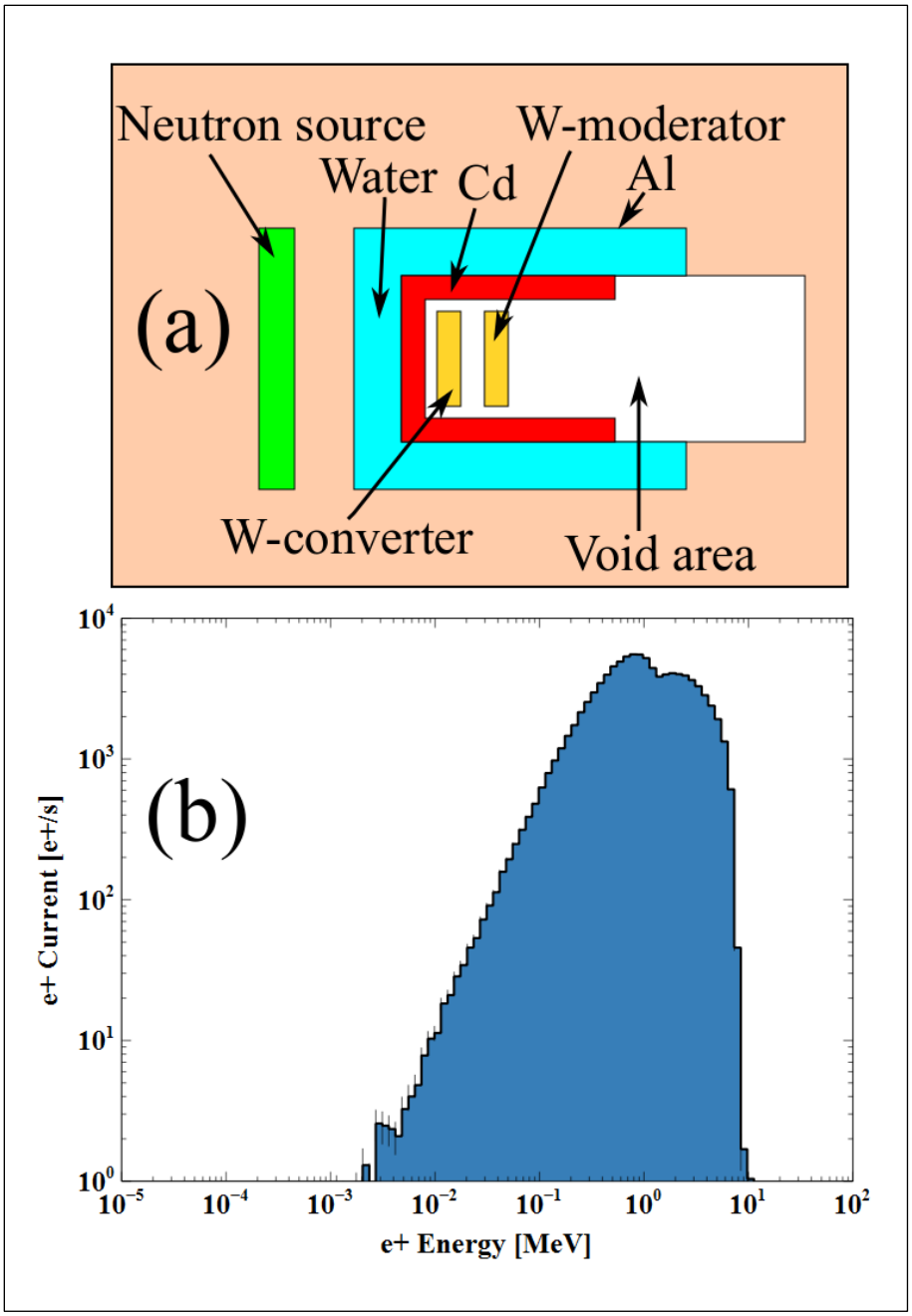

Figure 4.1. Positron generator design (a) Schematic of a Neutron Beamline-Based Positron Generator and (b) its Corresponding Energy Spectrum for a 5×10^{6} n cm^{-2} s^{-1} Neutron Flux.

This section presents a method for numerically predicting the moderation efficiency for tungsten foils. Using Monte Carlo simulations of a monoenergetic, monodirecitonal positron beam, efficiency tables were produced for both the backscattering and transmission foil geometries. These tables are implemented in the final yield calculations presented in Section 5. Additionally, the tables and the methodology behind their construction can be of use to the positron physics community in the design and development of new positron sources as well as in the optimization of current sources.

4.2. MODELING METHODOLOGY

Energy- and angle-dependent moderation efficiencies were calculated in three steps: (1) the positron stopping profiles in tungsten foils were obtained for combinations of incident angle and energy using Monte Carlo radiation transport simulations, (2) Makhovian profiles were then fit to the simulated stopping profiles, (3) the resulting best fit Makhovian profiles were processed by a code that performs numerical convolution with the Green's functions for the transmitted and backscattered moderation efficiencies in an infinite slab geometry. The final results were tabulated as a function of foil thickness, incident angle and positron energy. The unprocessed particle track tallies were also convolved with efficiency kernels derived from Green's functions though this resulted in considerably higher scatter in the resulting efficiencies.

A simplified model of a positron source and moderator was developed in the Monte Carlo of N-Particle radiation transport code, MCNP6. It comprises a tungsten foil of variable thickness. A monoenergetic and monodirectional positron beam source was

defined. The beam radius was 1 cm while the tungsten foil radius was chosen to be 10 cm to avoid edge effects. For each simulation, the tungsten foil thickness was chosen to be thick enough to stop all positrons. The positron energies were 10 keV, 100 keV, 300 keV, 500 keV, 800 keV, 1 MeV, 5 MeV, and 10 MeV. For each energy, simulations were performed for positron incidence angles of 0^o, 30^o, 60^o and 75^o from the surface normal (Figure 4.2). The energy range was chosen to cover a range relevant to both positron emitters (e.g. Na-22) as well as reactor-based sources (see Figure 4.1(b)). Each combination of energy and angle constituted a different simulation with a different foil thickness (10 μm for 10 and 100 keV, 60 μm for 300 keV, 100 μm for 500 keV, 200 μm for 800 keV, 350 μm for 1 MeV, 1500 μm for 5 MeV, and 3000 μm for 10 MeV). It should be mentioned that the thickness dependence in the calculated efficiencies is introduced through the Green's functions described below. To achieve statistical convergence in these calculations, a positron cutoff energy of 1 keV was chosen. In other words, positrons were considered "stopped" in the transport calculation once their energy fell below 1 keV. In reality, 1 keV positrons can travel a small distance (on order of nanometers) at this energy. Compared to the dimensions of the problem, however, a 1 keV cutoff yields almost the same stopping profile as a more physically realistic thermal energy cutoff (0.1-1 eV) but at considerably lower computational cost.

The physics options for positrons in MCNP6 were chosen so that the simulations were fully analog. MCNP6 does not have a built-in tally for determining the positions where particles are terminated by an energy cutoff. Instead, the particle tracking card, PTRAC, was used to track and filter terminal particle events inside the tungsten foil and write out the details of the terminal events to an output file. Using PTRAC rather than

tallies also has the advantage that the x, y and z coordinates of each terminal event are directly output, alleviating the need for a fine mesh tally or multiple cell or surface tallies. The authors will mention that an earlier attempt to use multiple surface tallies and determine the stopping rate of positrons by integrating the continuity Equation was partially successful. It was able to reproduce the general shape of the stopping profile though it also exhibited negative stopping probabilities. This is most likely due to the accumulation of numerical error and was therefore abandoned for the method described above.

The PTRAC output file was processed using a MATLAB script that parses the output file and creates a histogram of positron terminal events in depth bins spanning the thickness of the foil. This histogram thus represents the stopping profile. The script also convolves the coordinates of the terminal events with efficiency kernels derived from Green's functions of the diffusion Equation. The efficiency kernels are derived in the appendix. This method, which for lack of a better term will be referred to as the sampling method, combines analytical formulae for the efficiency kernels with a sample of particle histories from the PTRAC output file. The Green's functions are solutions of the 3D diffusion Equation for a point source placed at an given depth within an infinite slab of diffusing and absorbing medium. The depth, *z*, which is measured from the surface where the positron enters, represents the depth at which the positron stops and is thermalized. Infinite absorbing boundary conditions were chosen. The flux of thermal positrons to each surface of the foil was integrated over the surface areas to determine the total positron current in the transmission and backscattering geometries. The transmitted and

backscattered currents are given by Equations 20 and 21, respectively (Equations A.26, A.28 in the appendix)

$$J_+^{\mathrm{t}}(z;L) = \exp\left(-\frac{L-z}{L_+}\right) - \exp\left(-\frac{L}{L_+}\right)\frac{\sinh\left(\frac{L-z}{L_+}\right)}{\sinh\left(\frac{L}{L_+}\right)} \tag{20}$$

$$J_+^{\mathrm{b}}(z;L) = \exp\left(-\frac{z}{L_+}\right) - \exp\left(-\frac{L}{L_+}\right)\frac{\exp\left(-\frac{L-z}{L_+}\right) - \exp\left(-\frac{L+z}{L_+}\right)}{1-\exp\left(\frac{-2L}{L_+}\right)} \tag{21}$$

z is the depth that the positron is stopped and thermalized. L is the thickness of the moderator foil. L_+ is the positron diffusion length. A value of $L_+ = 0.135$ μm for tungsten was used in the analysis [62]. As these are the resulting positron currents for a source strength of unity (i.e. the current per particle), they also represent the moderator efficiency kernels.

Least squares fitting of the stopping profiles with Makhovian functions was also performed to determine the z_o and m parameters of Equation 4 as a function of energy and incident angle. The Makhovian functions were integrated numerically with the efficiency kernels (Equations 20 and 21) to determine the fraction of thermalized positrons diffusing to either face of the moderator foil. This fraction was then multiplied by the branching ratio for free positron emission into the vacuum. This gives the positron efficiency for the foil (Equation A.29 in appendix)

$$\varepsilon^i(L) = Y_0 \int_0^L J_+^i(z;L)p(z)dz \tag{22}$$

i indicates either transmitted or backscattering geometry and $Y_0 = 0.33$ is the branching ratio for emission of thermal positrons into the vacuum [62].

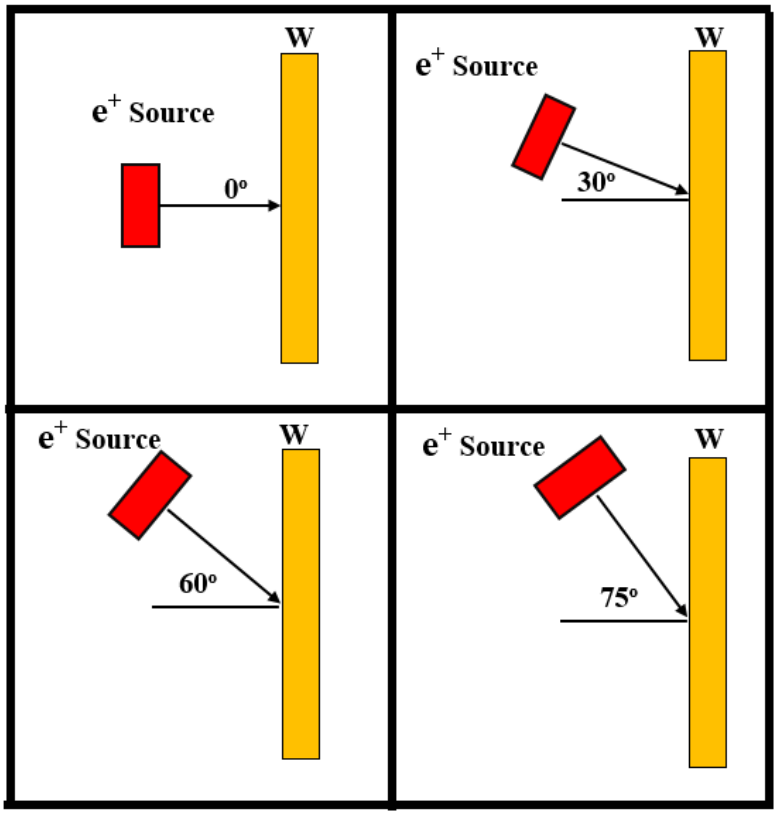

Figure 4.2. Positron Source and Moderator Geometries.

4.3. RESULTS AND DISCUSSION

The positron depth profiles calculated from the PTRAC output of the MCNP simulations are shown in Figures from Figure 4.3 to Figure 4.6 along with the best fit Makhovian theoretical profiles. Figure 4.3 shows the profiles for normally incident positrons (0^o). Those profiles are found to be in good agreement with the Makhovian shape. Also, Figures (4.4) and (4.5) shows the profiles for normally incident positrons (30^o) and (60^o). Figure 4.6 shows similar results at 75^o. The results for the other angles exhibited similar behavior. Table 4.1 contains the *m* values for each angle. There was little to no energy dependence on the *m* values. Therefore, the results of Table 4.1 represent the average over all eight energies. The z_o values are contained in Table 4.2 and

depend on both energy and angle. As expected, the z_o values decrease with increasing angle in accordance with the projected range along the axis normal to the foil surface. The observed increase in z_o with energy is also expected. z_o is proportional to the mean stopping depth and therefore varies, approximately, as a power of E.

Figure 4.7 compares two pairs of efficiency curves calculated by the sampling method (i.e. convolving the efficiency kernels with the terminal event coordinates sampled from PTRAC) with the method of integrating the efficiency kernels with the Makhovian profiles parameterized by the best-fit values of Tables 4.1 and 4.2. The comparison is only between the transmitted efficiency curves for 100 keV and 1 MeV at 0^o. These figures are representative of the low energy and high energy results. The variance is a consequence of the relatively small number of events written to the PTRAC output file and becomes more noticeable at high energies. As the mean separation of the terminal event coordinates becomes larger than the diffusion length, the underlying sample size effects become apparent. While the usual strategy for overcoming this type of unwanted variance in Monte Carlo radiation transport simulations would be to increase the number of particle histories, it is worth bearing in mind that the PTRAC card is not designed to efficiently and compactly contain particle history information like a conventional tally. Other radiation transport codes may not have this specific limitation.

Numerical integration of the best fit Makhovian profiles with the efficiency kernels resulted in much smoother efficiency curves, as can be seen in Figure 4.7 Given the advantage of this method and the ability of the Makhovian formula to capture the shape of the stopping profiles at all energies and angles with reasonable accuracy, all

tabulated efficiency values were based on numerical integration of the best-fit Makhovian profiles.

Figure 4.8 shows the transmission efficiencies for all simulated energies and angles. It is observed that, except for the 5 MeV and 10 MeV cases, the efficiencies have only weak angular dependence. At the highest energies, the positrons penetrate slightly deeper at lower angles. Table 4.3 shows the results for backscattering efficiencies for all energies and angles. The backscattering efficiencies increase with angle. The angular dependence is also more pronounced at higher energies. In light of these results, it might be reasonable to ignore the angular dependence in calculations of the moderation efficiency for lower energy sources such as ^{22}Na. Tables 4.4 - 4.7 contain the transmission efficiencies for positrons as a function of energy, angle and foil thickness. The backscattering efficiencies are shown in Figure 4.9. As the energy of the positron increases, its mean depth increases, placing more positrons at a greater number of diffusion lengths away from the surface. Therefore, the backscattering efficiencies decrease with increasing positron energy.

It is interesting to note that for a fixed thickness, the backscattering efficiency decreases monotonically with energy while the transmitted efficiency shows a maximum at the energy where the position of the peak in the stopping profile is equal to the foil thicknesses. Furthermore, for a fixed energy, the backscattering efficiency reaches a plateau above 2 μm. Positrons stopped after this depth are more than 14 diffusion lengths away from the back surface where their chances of diffusing to the back surface are negligible. Essentially, the backscattering efficiency depends only on the initial slope of the Makhovian profile in the first few microns of the foil. Considering these pieces of

information together, it can be concluded that for a monoenergetic positron source, the slow positron yield can be optimized by considering only the transmitted efficiency curve, provided the foils are thicker than 2 μm. For very thin foils (on the order of a few diffusion lengths), one would need to maximize the total efficiency vs. thickness curve.

The basic utility of these efficiency tables is that efficiencies can be interpolated over angle and energy and used in the determination of moderator efficiencies for an arbitrary positron flux. For example, one can integrate the energy spectrum of a specific β^+ emitter (e.g. ^{22}Na, ^{64}Cu) with the tabulated values to estimate the foil moderator efficiency for that particular source. This was done for both transmission and backscattering geometries in Figure 4.10 to compare the results of this work with values found in the literature [56-65, 91, 92] The diffusion length ($L_+ = 0.135$ μm) and branching ratio ($Y_0 = 0.33$), were both chosen to match those of Vehanen and Makinen [91]. Like this work, Vehanen and Makinen's calculations were based on Green's function solutions to the diffusion Equation, though the present work uses the 3D solutions and a slightly different parameterization of the Makhovian profiles. Nevertheless, our results are in good agreement with those of Vehanen and Makinen for both the transmitted and backscattered efficiencies. Reasonable agreement was also found with Weng *et al*.[59], Saito *et al*.[60] and Williams *et al*.[61] Other authors have reported much lower values for both backscattered and transmitted efficiencies. This may arise from variations in the microstructural properties of the moderator, its manufacture, and/or surface condition. Defects in the moderator can trap thermalized positrons reducing the diffusion length. This additional unknown variable, diffusion length, may have a large range of values between single crystal and polycrystalline tungsten and

between annealed and unannealed tungsten. Moreover, the condition of the surface will determine the density of surface trap states and the magnitude of the negative work function, both of which can have a significant effect on the value of Y_0. It is therefore likely that the large variation in efficiencies found in the literature stems from the wide variation in diffusion lengths and branching ratios that come with differences in moderator fabrication and surface condition.

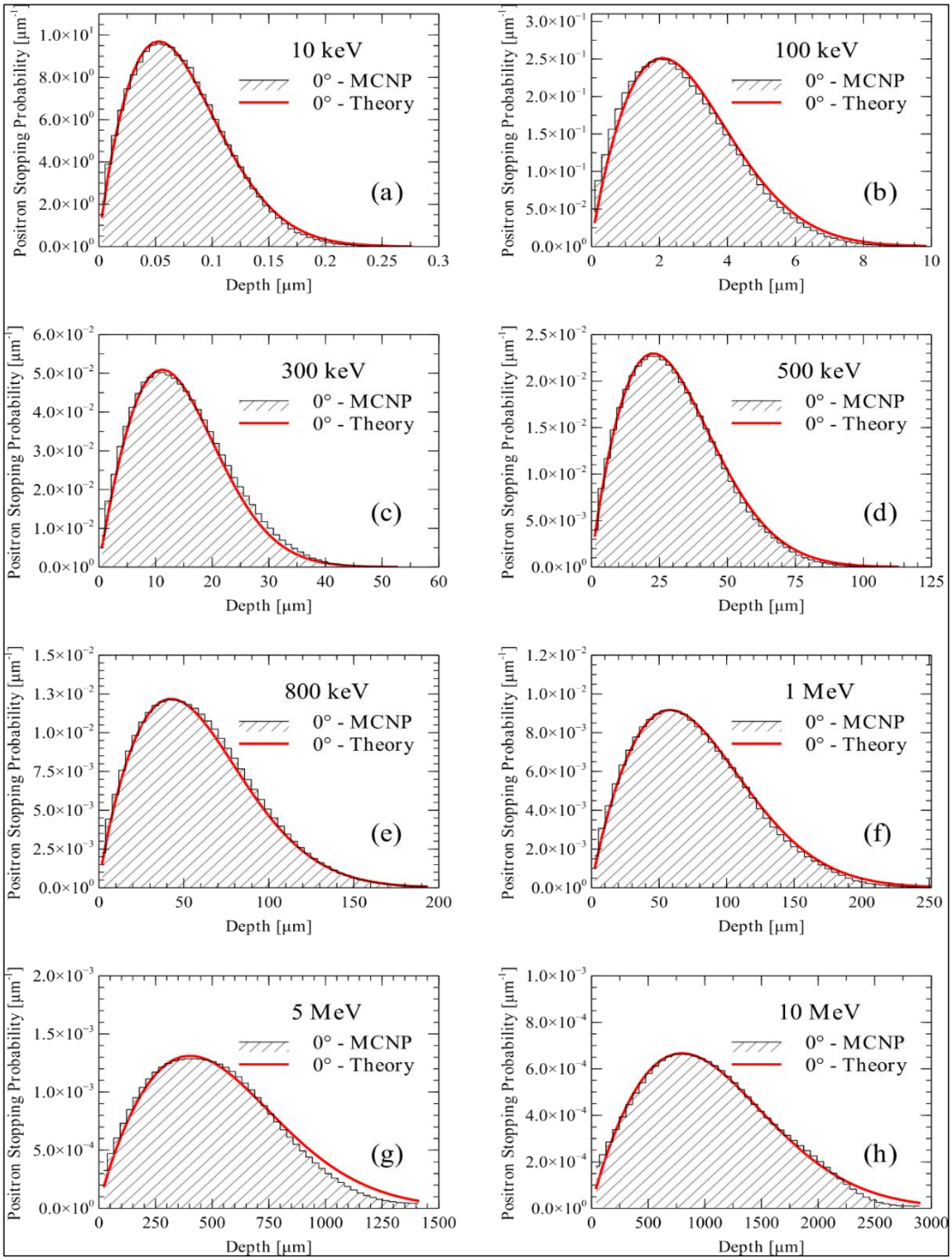

Figure 4.3. Positron Depth Profiles for (a) 10 keV, (b) 100 keV, (c) 300 keV, (d) 500 keV, (e) 800 keV, (f) 1 MeV, (g) 5 MeV, and (h) 10 MeV Normally Incident Positrons on Tungsten Calculated from Theoretical Expression and Using MCNP Radiation Transport Simulation.

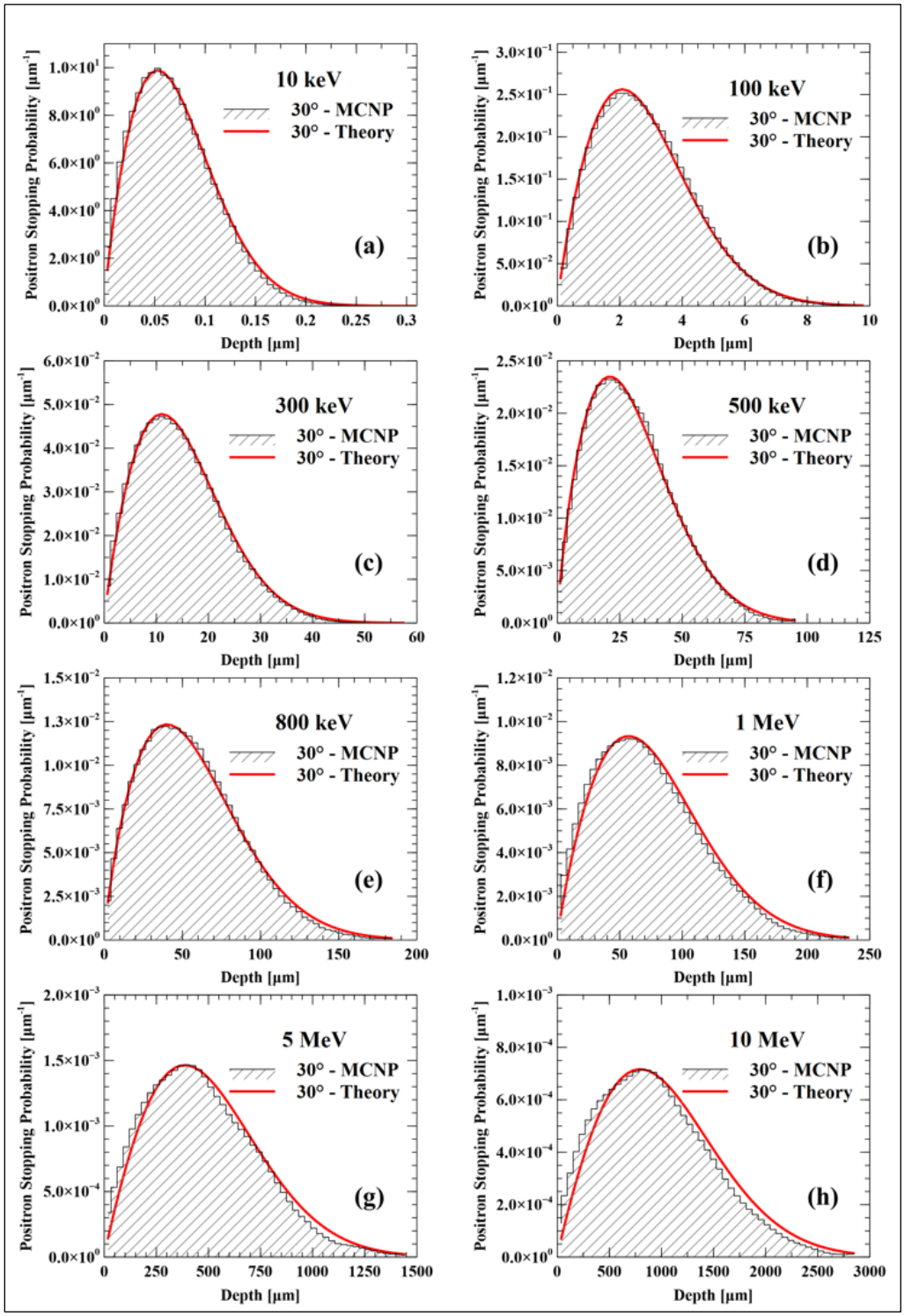

Figure 4.4. Positron Depth Profiles for (a) 10 keV, (b) 100 keV, (c) 300 keV, (d) 500 keV, (e) 800 keV, (f) 1 MeV, (g) 5 MeV, and (h) 10 MeV Positrons at 30° Incidence Angle on Tungsten Calculated from Theoretical Expression and Using MCNP Radiation Transport Simulation 30°.

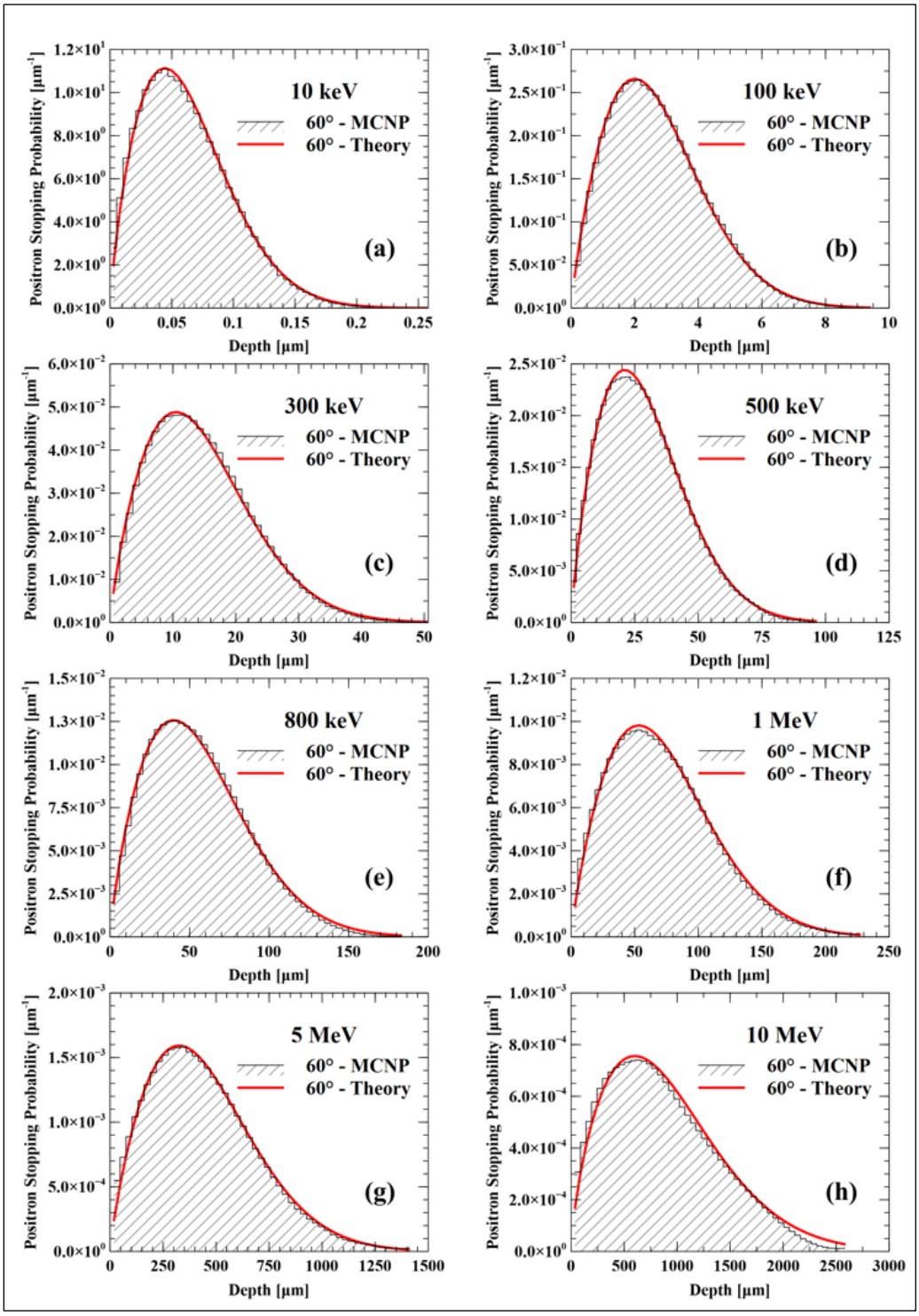

Figure 4.5. Positron Depth Profiles for (a) 10 keV, (b) 100 keV, (c) 300 keV, (d) 500 keV, (e) 800 keV, (f) 1 MeV, (g) 5 MeV, and (h) 10 MeV Positrons at 60° Incidence Angle on Tungsten Calculated from Theoretical Expression and Using MCNP Radiation Transport Simulation 60°.

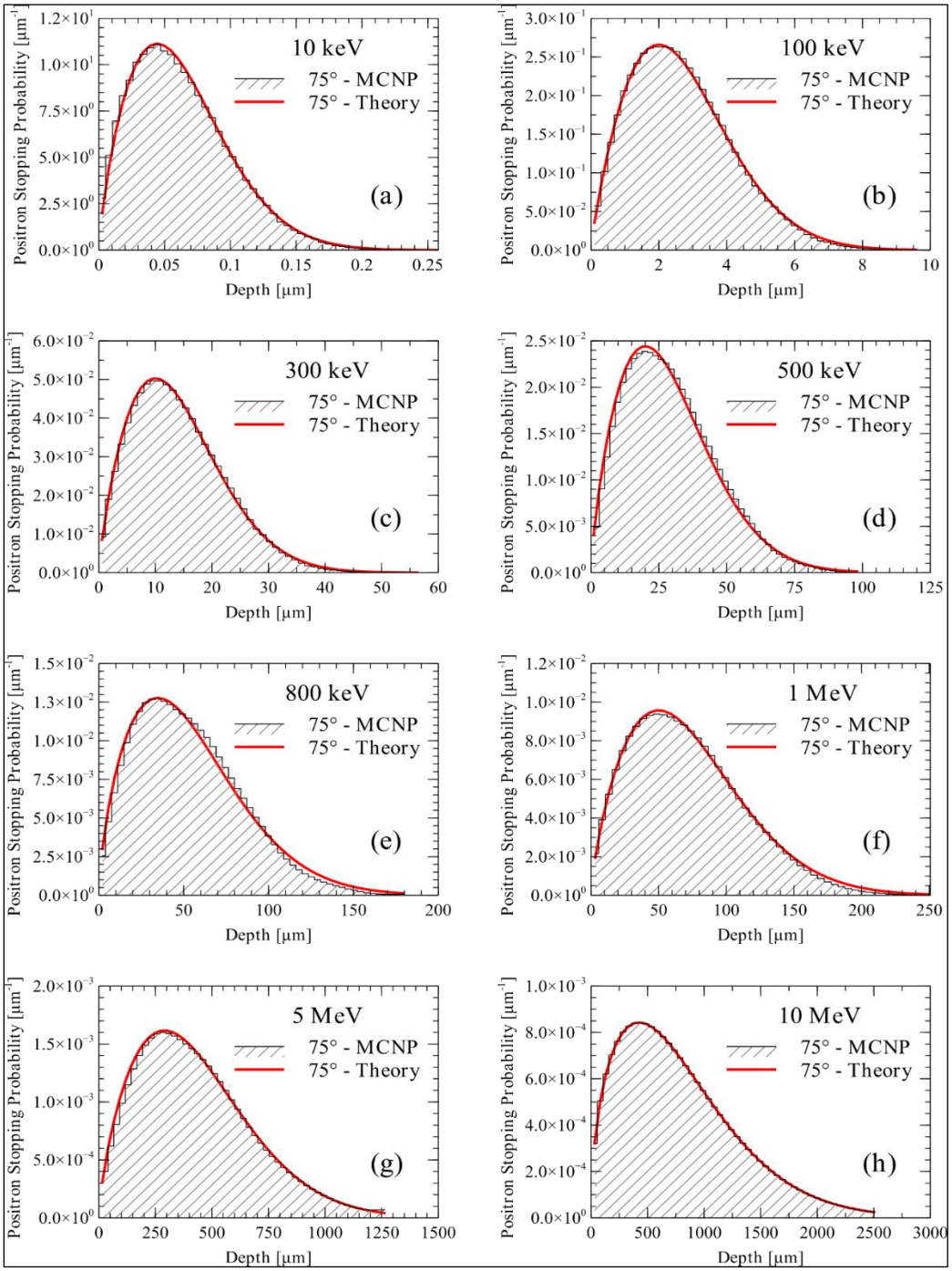

Figure 4.6. Positron Depth Profiles for (a) 10 keV, (b) 100 keV, (c) 300 keV, (d) 500 keV, (e) 800 keV, (f) 1 MeV, (g) 5 MeV, and (h) 10 MeV Positrons at 75° Incidence Angle on Tungsten Calculated from Theoretical Expression and Using MCNP Radiation Transport Simulation 75°.

Table 4.1. The m Values for Different Angle

θ	m
0^o	1.828 ± 0.019
30^o	1.835 ± 0.059
60^o	1.786 ± 0.049
75^o	1.715 ± 0.101

Table 4.2. z_o Values (in Microns) for Different Energies and Different Angles

z_0	**Energy**							
θ	**10 keV**	**100 keV**	**300 keV**	**500 keV**	**800 keV**	**1 MeV**	**5 MeV**	**10 MeV**
0º	0.083	3.22	16.5	35.24	66.27	88.8	619.2	1222.1
30º	0.082	3.18	16.9	33.84	64.46	87.29	569.08	1166.22
60º	0.075	3.06	16.4	32.9	63.59	82.47	506.77	1027.9
75º	0.072	3.06	15.9	32.46	60.5	82.33	484.88	884.04

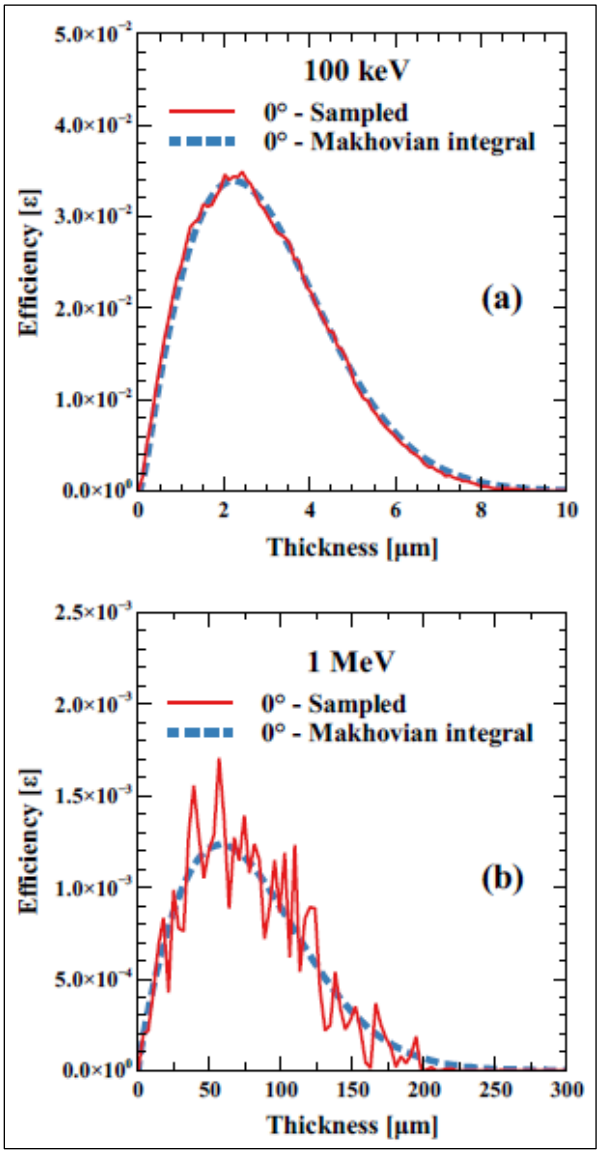

Figure 4.7. Comparison of the Efficiency Curves for (a) 100 keV and (b) 1 MeV Positrons as Generated from the Processed. PTRAC Output File (Solid Red Lines) and from Numerical Integration of the Best Fit Makhovian Profile (Dashed Blue Lines).

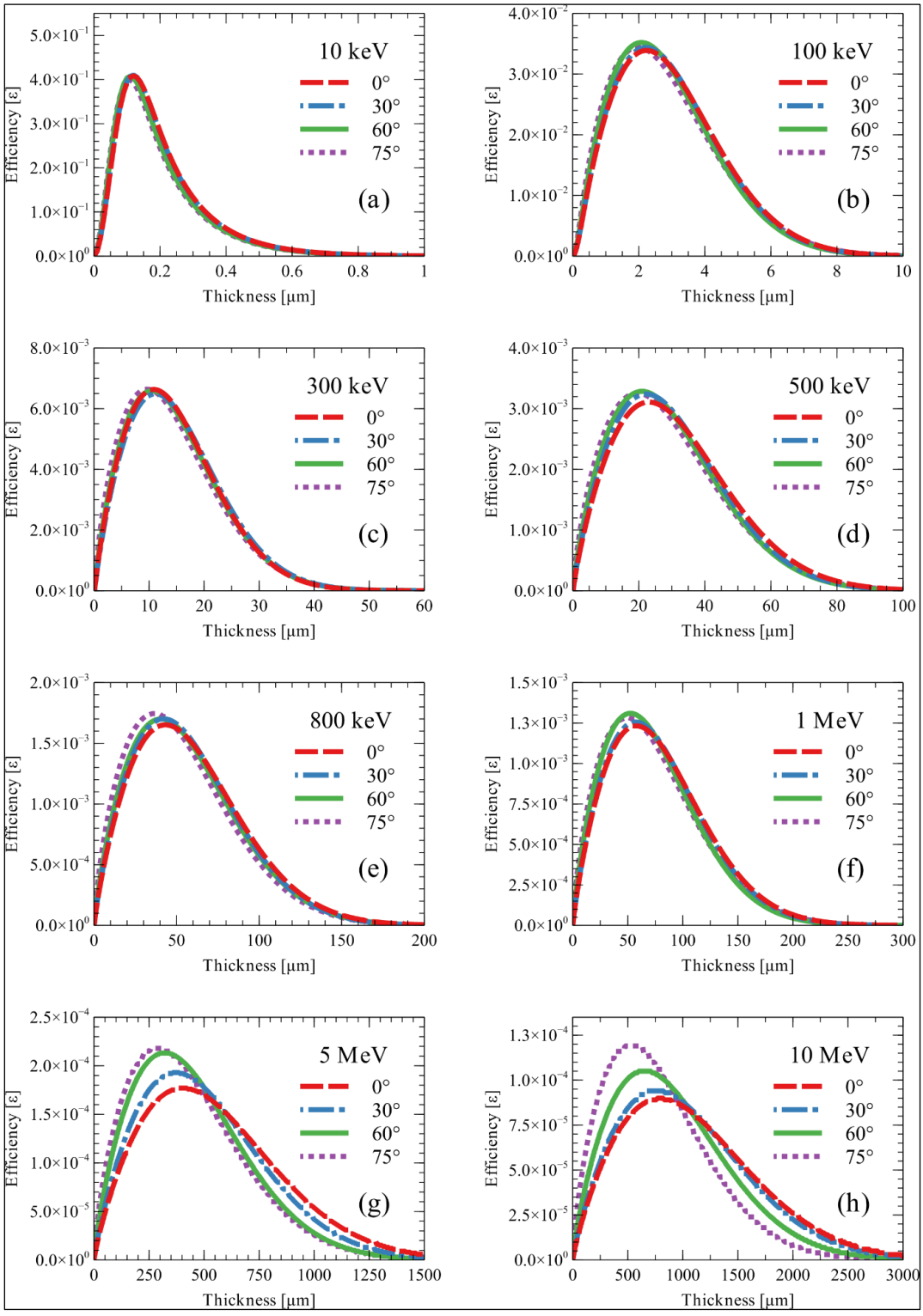

Figure 4.8. The Transmission Moderation Efficiencies for (a) 10 keV, (b) 100 keV, (c) 300 keV, (d) 500 keV, (e) 800 keV, (f) 1 MeV, (g) 5 MeV, and (h) 10 MeV Positrons at Different Angles.

Table 4.3. Backscattering Efficiencies for Different Positrons Energies and Different Angles

		Efficiency ε_b t > 2 μm						
θ	**10 keV**	**100 keV ($x10^{-3}$)**	**300 keV ($x10^{-4}$)**	**500 keV ($x10^{-5}$)**	**800 keV ($x10^{-5}$)**	**1 MeV ($x10^{-5}$)**	**5 MeV ($x10^{-7}$)**	**10 MeV ($x10^{-7}$)**
0º	0.6052	5.1	2.59	6.46	2.04	1.19	3.40	0.98
30º	0.6085	5.2	2.42	6.77	2.07	1.19	3.79	1.02
60º	0.6335	6.1	3.08	8.87	2.73	1.71	6.64	1.87
75º	0.6452	7.4	4.47	13.2	4.55	2.69	12.9	4.64

Table 4.4. Transmission Efficiencies for 10 keV Positrons

	Efficiency			
	10 keV			
t [um]	**0º $x10^{-3}$**	**30º $x10^{-3}$**	**60º $x10^{-3}$**	**75º $x10^{-3}$**
0.01	11.51	11.61	14.94	18.21
0.03	87.27	88.59	105.87	117.49
0.05	195.46	198.58	225.46	237.96
0.07	298.21	302.43	327.91	334.27
0.1	392.73	396.03	403.65	397.84
0.12	408.65	410.13	403.65	392.59
0.15	380.85	379.54	358.75	345.39

Table 4.4. Transmission Efficiencies for 10 keV Positrons (cont.)

0.18	323.61	320.69	295.59	283.68
0.2	282.60	279.32	255.00	244.64
0.25	194.61	191.78	173.49	166.51
0.3	133.03	131.02	118.37	113.63
0.35	91.31	89.92	81.23	77.98
0.4	62.86	61.91	55.92	53.69
0.45	43.34	42.69	38.56	37.02
0.5	29.91	29.45	26.61	25.54
0.55	20.64	20.33	18.37	17.63
0.6	14.25	14.04	12.68	12.17
0.65	9.840	9.69	8.75	8.40
0.7	6.79	6.69	6.04	5.80
0.75	4.69	4.62	4.17	4.01
0.8	3.23	3.19	2.88	2.77
0.85	2.23	2.20	1.99	1.91
0.9	1.54	1.52	1.37	1.32
0.95	1.07	1.05	0.95	0.91
1	0.73	0.73	0.65	0.63
2	0.00	0.00	0.00	0.00

Table 4.5. Transmission Efficiencies for 100 keV and 300 keV Positrons

	Efficiency							
	100 keV				**300 keV**			
t [μm]	**0º ($x10^{-2}$)**	**30º ($x10^{-2}$)**	**60º ($x10^{-2}$)**	**75º ($x10^{-2}$)**	**0º ($x10^{-3}$)**	**30º ($x10^{-3}$)**	**60º ($x10^{-3}$)**	**75º ($x10^{-3}$)**
1	2.3299	2.3697	2.5948	2.711	1.303	1.23	1.45	1.841
2	3.3548	3.4074	3.515	3.4371	2.372	2.25	2.56	3.054
3	3.096	3.1188	3.072	2.9374	3.345	3.185	3.54	4.061
4	2.2077	2.1932	2.0782	2.0043	4.181	3.994	4.362	4.862
5	1.2892	1.2562	1.1527	1.1531	4.926	4.721	5.079	5.524
6	0.6335	0.6023	0.5389	0.5744	5.439	5.228	5.562	5.944
7	0.2661	0.2456	0.2158	0.2517	5.904	5.693	5.989	6.291
8	0.0965	0.086	0.0748	0.098	6.232	6.029	6.281	6.502
9	0.0305	0.0261	0.0226	0.0342	6.47	6.282	6.482	6.617
10	0.0084	0.0068	0.006	0.0107	6.6	6.432	6.577	6.631
15	-	-	-	-	6.002	5.97	5.882	5.666
20	-	-	-	-	4.292	4.376	4.191	3.938
25	-	-	-	-	2.524	2.648	2.484	2.321
30	-	-	-	-	1.267	1.373	1.271	1.203
35	-	-	-	-	0.548	0.615	0.567	0.553
40	-	-	-	-	0.204	0.238	0.22	0.225
45	-	-	-	-	0.067	0.082	0.076	0.084
50	-	-	-	-	0.019	0.025	0.024	0.028
55	-	-	-	-	0.005	0.007	0.006	0.009
60	-	-	-	-	0.001	0.002	0.002	0.002

Table 4.6. Transmission Efficiencies for 500 keV, 800 keV and 1 MeV Positrons

	Efficiency											
	500 keV				**800 keV**				**1 MeV**			
t [μm]	**0º (x10^{-3})**	**30º (x10^{-3})**	**60º (x10^{-3})**	**75º (x10^{-3})**	**0º (x10^{-4})**	**30º (x10^{-4})**	**60º (x10^{-4})**	**75º (x10^{-4})**	**0º (x10^{-4})**	**30º (x10^{-4})**	**60º (x10^{-4})**	**75º (x10^{-4})**
1	0.32	0.34	0.41	0.54	0.10	0.10	0.13	0.19	0.62	0.62	0.83	1.14
2	0.61	0.64	0.75	0.93	0.19	0.20	0.23	0.32	1.17	1.18	1.52	1.97
3	0.86	0.91	1.05	1.24	0.27	0.28	0.33	0.43	1.66	1.69	2.13	2.66
4	1.09	1.17	1.32	1.52	0.35	0.36	0.41	0.53	1.98	2.01	2.51	3.08
5	1.31	1.40	1.57	1.77	0.42	0.44	0.49	0.63	2.43	2.47	3.05	3.67
6	1.52	1.62	1.79	1.99	0.49	0.51	0.57	0.71	2.86	2.91	3.56	4.21
7	1.71	1.82	1.99	2.19	0.56	0.58	0.64	0.79	3.27	3.34	4.05	4.72
8	1.89	2.01	2.19	2.37	0.62	0.65	0.71	0.87	3.68	3.75	4.52	5.20
9	2.10	2.19	2.36	2.53	0.68	0.71	0.78	0.94	4.06	4.15	4.96	5.66
10	2.20	2.35	2.52	2.67	0.74	0.77	0.84	1.00	4.44	4.54	5.40	6.09
20	3.06	3.22	3.28	3.25	1.22	1.28	1.33	1.49	7.48	7.67	8.76	9.31
30	2.92	2.98	2.93	2.81	1.52	1.58	1.61	1.71	9.81	10.06	11.15	11.4
40	2.22	2.18	2.09	1.99	1.65	1.70	1.70	1.73	11.32	11.59	12.52	12.5
50	1.42	1.32	1.24	1.20	1.62	1.66	1.64	1.62	12.14	12.41	13.08	12.8
60	0.78	0.68	0.64	0.64	1.49	1.51	1.47	1.42	12.31	12.54	12.92	12.5
70	0.37	0.31	0.28	0.30	1.29	1.29	1.25	1.18	11.94	12.11	12.2	11.7
80	0.16	0.12	0.11	0.13	1.07	1.05	1.01	0.93	11.15	11.24	11.07	10.5
90	0.06	0.04	0.04	0.05	0.84	0.81	0.78	0.71	10.1	10.13	9.76	9.33
100	0.02	0.01	0.01	0.02	0.63	0.59	0.58	0.52	8.86	8.81	8.31	7.97
110	-	-	-	-	0.46	0.42	0.41	0.36	7.59	7.49	6.92	6.69
120	-	-	-	-	0.32	0.28	0.28	0.25	6.31	6.17	5.57	5.46

Table 4.6. Transmission Efficiencies for 500 keV, 800 keV and 1 MeV Positrons (cont.)

130	-	-	-	-	0.21	0.19	0.19	0.16	5.15	4.99	4.41	4.39
140	-	-	-	-	0.14	0.12	0.12	0.11	4.08	3.91	3.39	3.44
150	-	-	-	-	0.09	0.07	0.07	0.07	3.16	2.99	2.54	2.64
160	-	-	-	-	0.05	0.04	0.04	0.04	2.41	2.26	1.88	2.00
170	-	-	-	-	0.03	0.02	0.03	0.02	1.79	1.65	1.35	1.48
180	-	-	-	-	0.02	0.01	0.01	0.01	1.32	1.20	0.96	1.09
190	-	-	-	-	0.01	0.01	0.01	0.01	0.94	0.84	0.66	0.78
200	-	-	-	-	0.01	0.00	0.00	0.00	0.66	0.59	0.45	0.56
210	-	-	-	-	-	-	-	-	0.45	0.4	0.30	0.38
220	-	-	-	-	-	-	-	-	0.31	0.26	0.19	0.26
230	-	-	-	-	-	-	-	-	0.20	0.17	0.13	0.18
240	-	-	-	-	-	-	-	-	0.13	0.11	0.08	0.12
250	-	-	-	-	-	-	-	-	0.09	0.07	0.05	0.08
260	-	-	-	-	-	-	-	-	0.05	0.04	0.03	0.05
270	-	-	-	-	-	-	-	-	0.03	0.03	0.02	0.03
280	-	-	-	-	-	-	-	-	0.02	0.02	0.01	0.02
290	-	-	-	-	-	-	-	-	0.01	0.01	0.01	0.01
300	-	-	-	-	-	-	-	-	0.01	0.01	0.00	0.01

Table 4.7. Transmission Efficiencies for 5 MeV and 10 MeV Positrons

	Efficiency							
	5 MeV				**10 MeV**			
t [μm]	**0º ($x10^{-5}$)**	**30º ($x10^{-5}$)**	**60º ($x10^{-5}$)**	**75º ($x10^{-5}$)**	**0º ($x10^{-5}$)**	**30º ($x10^{-5}$)**	**60º ($x10^{-5}$)**	**75º ($x10^{-5}$)**
1	0.2	0.3	0.4	0.7	0.1	0.1	0.2	0.4
10	1.3	1.5	2.2	3.1	0.3	0.4	0.5	1.0
20	2.2	2.6	3.6	4.8	0.7	0.7	1.1	1.8
30	3.2	3.7	5.0	6.5	0.9	1.0	1.4	2.3
40	4.1	4.7	6.4	8.0	1.1	1.2	1.8	2.8
50	4.8	5.5	7.4	9.2	1.4	1.5	2.2	3.4
60	5.6	6.5	8.6	10.4	1.6	1.8	2.5	3.8
70	6.4	7.4	9.7	11.6	1.8	2.0	2.7	4.2
80	7.1	8.1	10.6	12.5	2.1	2.3	3.1	4.7
90	7.8	9.0	11.6	13.6	2.3	2.5	3.4	5.0
100	8.5	9.8	12.5	14.5	2.5	2.7	3.6	5.4
200	13.7	15.6	18.9	20.3	4.3	4.7	6.1	8.4
300	16.7	18.7	21.3	21.8	5.8	6.3	7.9	10.3
400	17.7	19.2	20.5	20.2	7.0	7.5	9.2	11.5
500	17.0	17.8	17.8	17.0	7.9	8.5	10.1	11.9
600	15.1	15.1	14.1	13.1	8.5	9.1	10.5	11.8
700	12.6	12.0	10.3	9.5	8.9	9.4	10.5	11.3

Table 4.7. Transmission Efficiencies for 5 MeV and 10 MeV Positrons (cont.)

800	10.0	9.0	7.1	6.5	9.0	9.4	10.2	10.4
900	7.5	6.3	4.6	4.2	8.8	9.2	9.6	9.4
1000	5.4	4.2	2.8	2.5	8.6	8.8	8.9	8.3
1500	0.5	0.3	0.1	0.1	5.6	5.4	4.4	3.2
2000	-	-	-	-	2.6	2.3	1.5	0.8
2500	-	-	-	-	0.9	0.7	0.4	0.1
3000	-	-	-	-	0.2	0.2	0.1	0

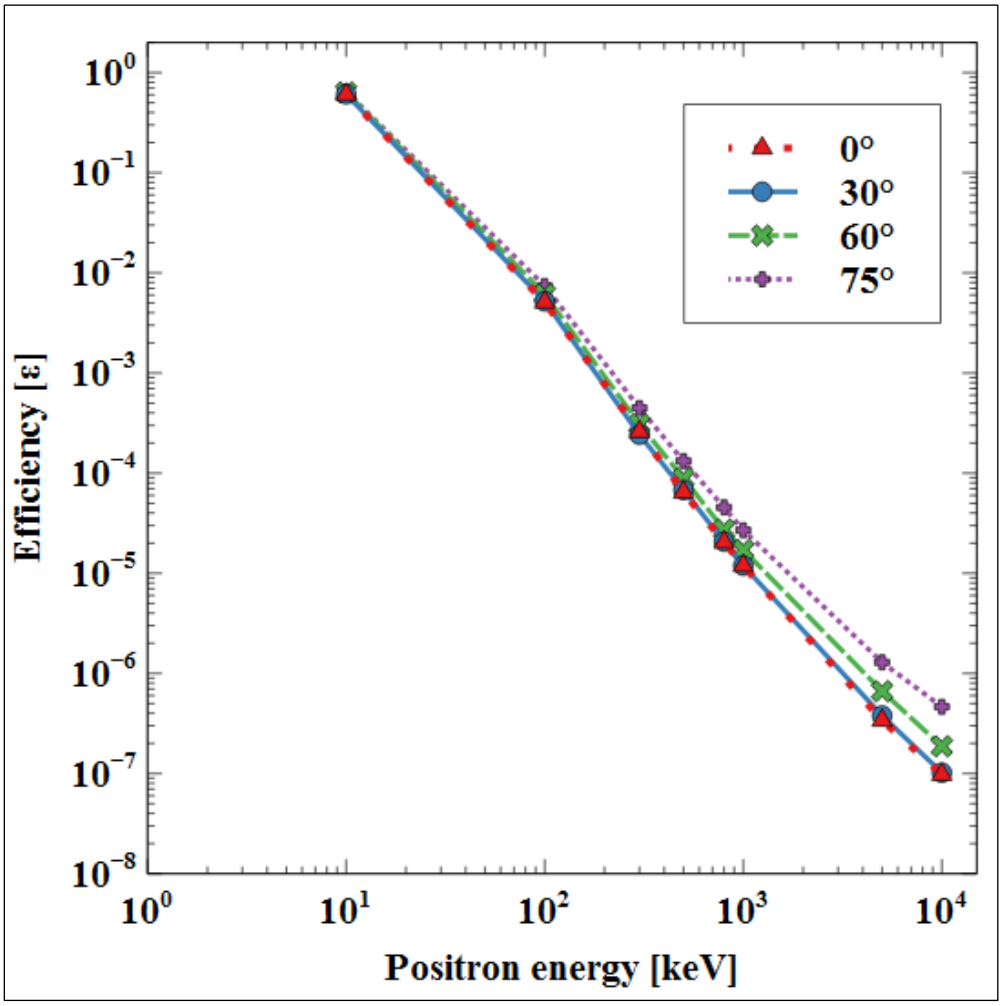

Figure 4.9. Backscattering Efficiencies as a Function of Positron Energy and Angle. These Results are Calculated for a Foil Thickness of 10 μm. Efficiencies for Foils Thicker than 2 μm (15 Diffusion Lengths) are Virtually Identical.

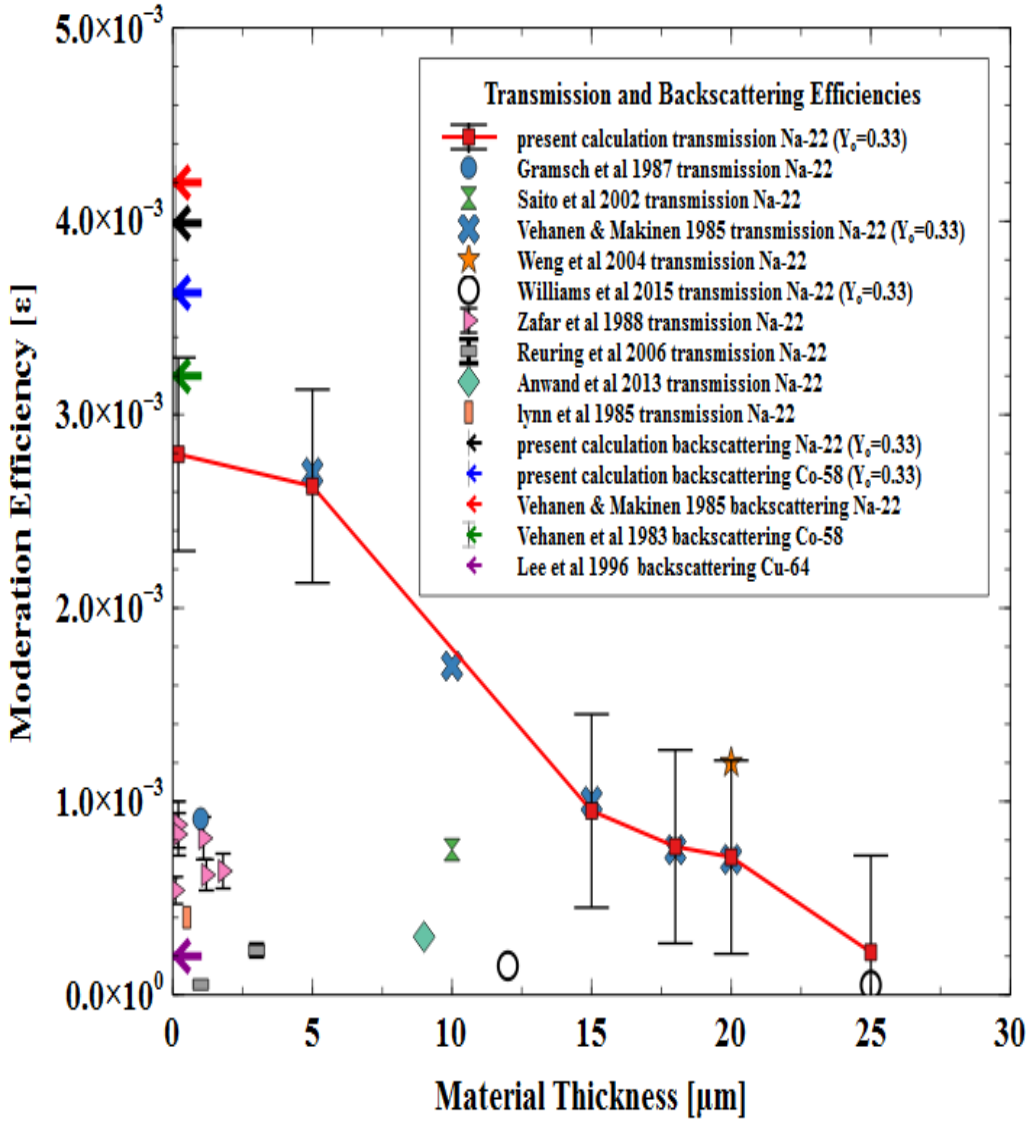

Figure 4.10. Moderation Efficiency as Function of Tungsten Foil Thickness for Transmission and Backscattering Geometries.

5. OPTIMIZING THE MODERATOR GEOMETRY AND THICKNESS FOR A REACTOR-BASED SLOW POSITRON SOURCE

5.1. OVERVIEW

This section is concerned with modeling the generation and extraction of slow positrons in a positron source at the MSTR beam port. The MCNP6 code was used to model a Cd (n,γ) converted and W foil moderator grid, with particular emphasis paid to the positron moderator. Tabular moderation efficiencies presented in Section 4 were incorporated into the calculation of the moderation rate. Analytical expressions for the extraction efficiency were also used to account for annihilation loses during electrostatic extraction.

5.2. THEORY

5.2.1. Extraction Efficiency of Tungsten Foil Grids. Supposing a thermalized positron is spontaneously emitted by the negative work function of a tungsten metal foil, it can be extracted using an electric field of sufficient strength.

During the process, the positron may make further collisions with other foils and surfaces in the grid during which it may either become trapped at surface states, annihilate with surface electrons, form positronium, or be reflected. Reducing the density of foils/wires in the moderator grid reduces the frequency of positron metal collisions. The production of slow positrons, however, roughly scales with the amount of tungsten present in the conversion grid. This presents an interesting optimization problem. The analysis of Weng *et al.* [59]. incorporated some of the extraction loss effects by assuming

a constant transmission probability, t, for a fast positron not stopping in a particular layer of a wire mesh with N layers

$$P_{\text{slow}} = \mathrm{N}\mu(1-t)t^{N-1} \tag{23}$$

μ is the probability that a fast positron, having stopped in the wire, is reemitted as a slow positron. Weng *et al.* assumed that the positrons were all moving in a constant direction (essentially a one-dimensional beam) and that the transmission probability was the same for fast positrons and slow positrons. They also assumed that each emitted slow positron that collides with a wire has zero probability of being re-emitted. In fact, experiments show that a free positron colliding with the tungsten surface has a high probability of being reflected back into the vacuum [93]. Essentially, as the positron nears the surface it again feels both the influence of the surface potential and the negative work function. The negative work function can repel the positron back into the vacuum while the surface potential has the capacity to trap the positron where it may form positronium or annihilate with a surface electron. Considering these effects, an expression of the extraction efficiency is derived below.

First, one must consider the velocities of slow positrons emitted in a grid of W foils. The positron at the surface of tungsten is presumed to be well thermalized. As such, its velocity profile can be approximated as a Maxwell-Boltzmann distribution having a mean thermal velocity of

$$\langle v \rangle = 2\sqrt{\frac{2kT}{\pi m}} \tag{24}$$

Ignoring Fermi-Dirac statistics is justified on the grounds that the positron density in the metal is low. The mass of the positron might be replaced with its effective mass in the

metal. Nevertheless, at room temperature the above expression gives a velocity on the order of 100 km s^{-1}. On the other hand, the positron gains energy when it acted on by the negative work function W at the surface. This gives a velocity component normal to the surface, $v_\perp$.

$$\frac{1}{2}mv_\perp^2 = W \tag{25}$$

$$v_\perp = \sqrt{\frac{2W}{m}} \tag{26}$$

$v_\perp$ is on the order of 1000 km s^{-1}. Given that the main portion of the velocity of the slow positron is normal to the surface, the thermal component of the velocity will be ignored in the remaining analysis. The probability of a positron being extracted from the moderator depends on the number of times it collides with another moderator foil before an electrostatic extraction field clears it from the moderator grid. The problem is one of a charged particle moving in an electric field with some initial position and velocity. To simplify matters further, the electric field is assumed to be uniform and a single channel (channel denoting the space between adjacent foils) of the grid is considered. The channel consists of two tungsten foils of length L and separation (foil-to-foil pitch) h. The extraction process is illustrated in Figure 5.1.

Under the influence of a uniform electric field, the position of the positron along the length of the channel is given by

$$x = x_0 + \frac{eE}{2m}t^2 \tag{27}$$

while the position of the positron between the parallel foils is

$$y = v_\perp t \tag{28}$$

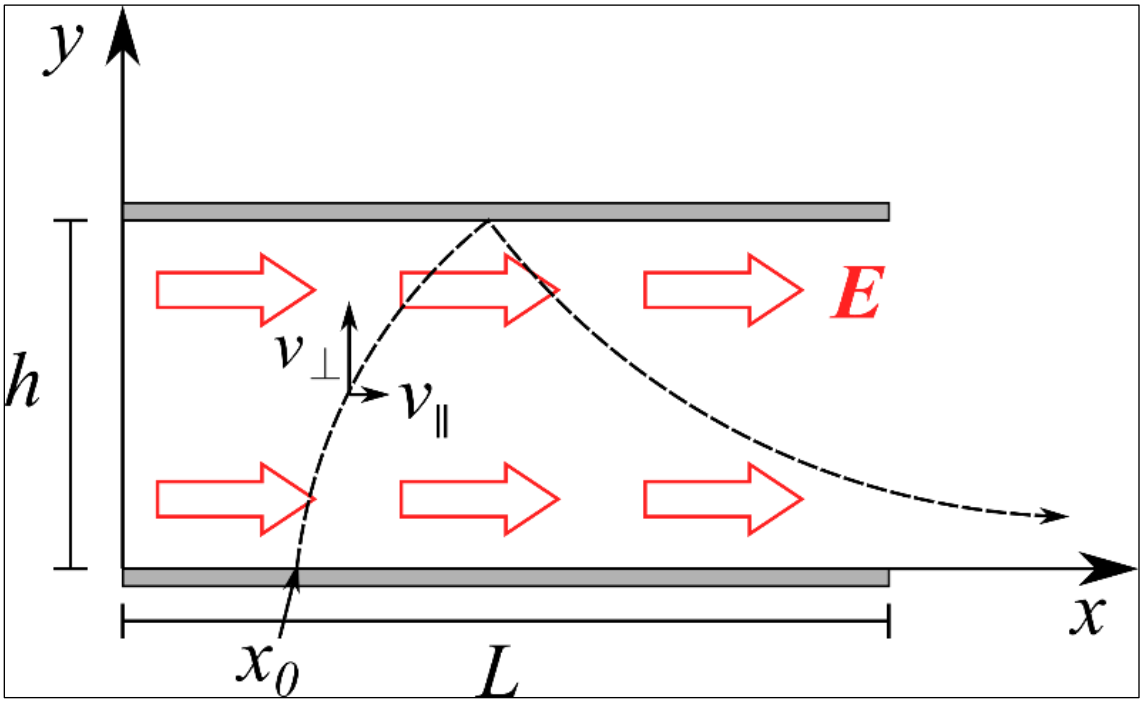

Figure 5.1. Positron Emission Inside Tungsten Grid.

E is the uniform electric field strength, parallel to the channel axis. x_0 is the position where the slow positron was originally emitted. These Equations describe the trajectory of the particle up to the point that it collides with an opposing face. The probability of the positron surviving the reflection is given by R_0 . The rate at which the positron travels down the channel depends on the nature of the reflection. If the positron does not interact with the orbital electrons long enough to dissipate a portion of its momentum component parallel to the channel direction, $p_{\parallel}$, it is reasonable to expect that reflection will be approximately specular as the potential varies only along the direction normal to the surface. Given that the width of the boundary double layer is on the order of a Wigner-Seitz radius, this possibility is plausible. In such a case, the velocity of the positron increases continuously over time until it exits the extraction field. On the other extreme,

if the positron is able to effectively re-thermalize in each reflection event, thereby losing its $p_{\parallel}$ component, it will be re-emitted with velocity normal to the surface and reaccelerated. Both of these extremes are considered.

5.2.2. Specular Reflection. The time, $'$, that it takes for the positron to clear the edge of the grid is given by

$$L = x_0 + \frac{eE}{2m} t'^2 \tag{29}$$

$$t' = \sqrt{\frac{2m(L - x_0)}{eE}} \tag{30}$$

In that time, the total distance the positron travels along the y direction is

$$y = v_{\perp} t' \tag{31}$$

The number of positron foil collisions (reflections), n, depends on the foil-to-foil pitch

$$n = \frac{y}{h} = \frac{1}{h} v_{\perp} \sqrt{\frac{2m(L - x_0)}{eE}} \tag{32}$$

Substituting Equation 26 into Equation 32 gives

$$n = \frac{2}{h} \sqrt{\frac{W(L - x_0)}{eE}} \tag{33}$$

Equation 33 only depends on the work function, the electric field, the pitch and length of the moderator grid.

5.2.3. Non-Specular Reflection. For non-specular reflection, the positron must be reaccelerated by the electric field between each re-thermalization event. The time between reflections is given by

$$t' = \frac{h}{v_{\perp}} \tag{34}$$

The distance traveled along the length per reflection is then

$$\Delta x = \frac{eE}{2m} t'^2 \tag{35}$$

$$\Delta x = \frac{eEh^2}{4W} \tag{36}$$

and so the number of reflections is given by

$$n = \frac{L - x_0}{\Delta x} \tag{37}$$

$$n = \frac{4W(L - x_0)}{h^2 eE} \tag{38}$$

Equation 38 is the square of the result for specular reflection (Equation 33). This suggests that it might be reasonable to treat the general case as

$$n = \left(\frac{4W(L - x_0)}{h^2 eE}\right)^a = A(L - x_0)^a; \qquad \frac{1}{2} < a < 1 \tag{39}$$

$$A = \frac{4W}{h^2 eE} \tag{40}$$

a depends on the ability of the moderator to absorb a fraction of the positron momentum parallel to the foil.The average probability that slow positrons, emitted uniformly along the length of the foil, are extracted is

$$P = \int_0^L R_0^{n(x_0)} dx_0 \tag{41}$$

5.3. METHODS

A simplified model of the MSTR beam port comprises a monodirectional and monoenergetic (0.0253 eV) thermal neutron source, a cadmium cup (n,γ) converter and tungsten grid for pair production and positron moderation. The model was developed in the Monte Carlo of N-Particle radiation transport code, MCNP6. The tungsten grid geometry was modified in order to find an optimal combination of foil thickness, length and pitch. The dimensions of the source were 4.4 cm × 7 cm, matching the dimensions of the beam port opening of the MSTR. The tungsten grid radius was 6.95 cm. The thickness of the cadmium cup was taken to be 1 mm. The thickness of the cadmium cup was varied to maximize the gamma ray flux. 1 mm was found to be close to the optimal thickness. Although the mass thickness of Cd can eventually be consumed by prolonged exposure to neutrons in high flux beam ports, simple calculations of the reaction rate showed that this is of minor concern at the MSTR beam port, which has a comparatively small thermal neutron flux of about 5×10^{6} cm^{-2} s^{-1}. After 1600 hours of full power operation at MSTR, the change in Cd mass thickness is negligible. The tungsten grid thicknesses (t) chosen were 5, 10, 25, 35, 50, 75, 100, and 125 μm. The tungsten grid lengths (L) were 1, 2, 3, 4, 5, and 6 cm, while the pitch (h) between tungsten foils were 0.1, 0.2, 0.3, 0.4, 0.5, and 0.6 cm. Each combination of length, pitch and thickness constituted a different simulation. Figure 5.2 illustrates some of the different combinations of grid geometry. In order to calculate the number of fast positrons that stop in the tungsten foils and are re-emitted as slow positrons, surface current tallies were integrated with energy-, angle- and thickness-dependent moderation efficiency tables.

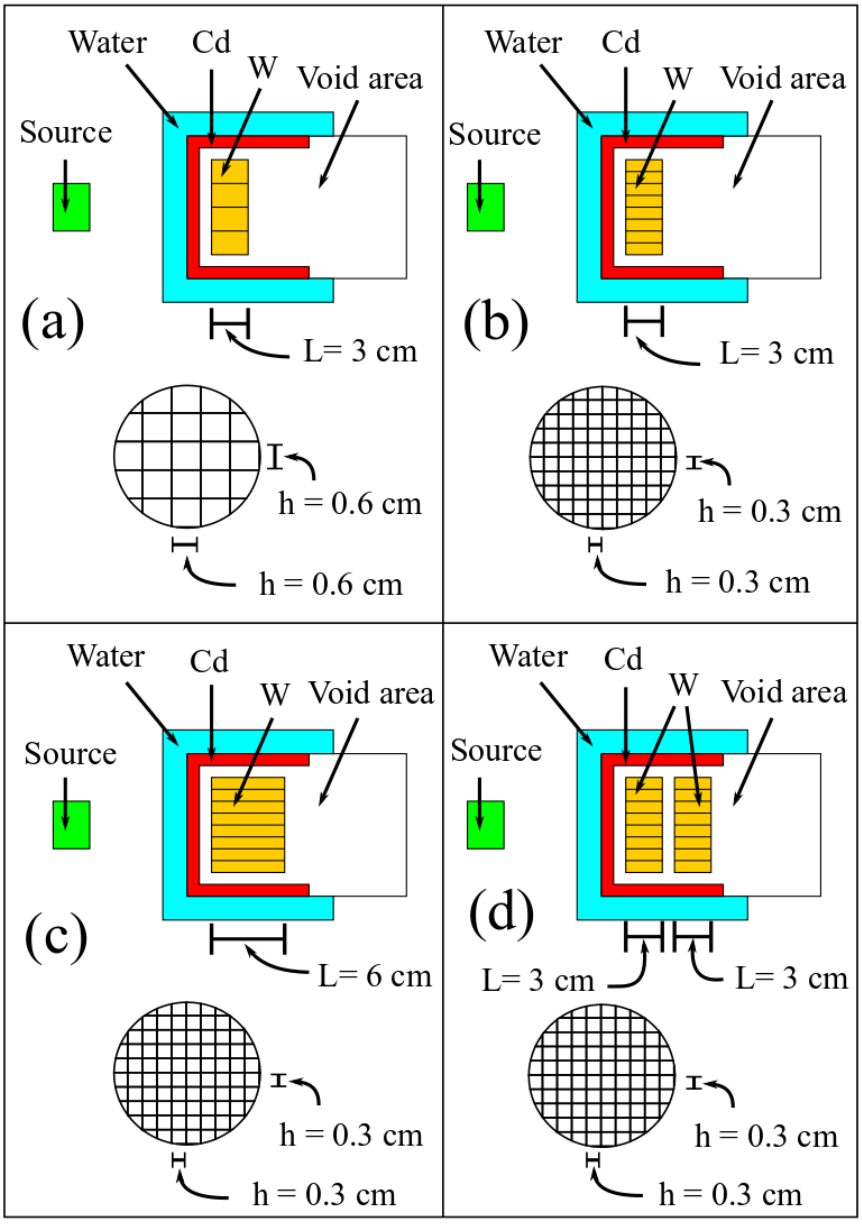

Figure 5.2. Tungsten Grids with Different Pitches and Lengths.

In a companion paper, calculations of the positron moderation efficiencies for tungsten foils were obtained by combining Monte Carlo stopping calculations in a single foil with analytical formulas of the slow positron surface flux derived by integrating

Green's function solutions of the diffusion Equation over the surface of an infinite slab foil. The Green's functions solutions assume a value of the positron diffusion length of $L_+ = 0.135$ μm for tungsten [62]. This was done in both the transmission and backscattering geometries for different combinations of incident positron energy, angle and for different thicknesses of tungsten foil. The resulting efficiency tabulations can be implemented with the tally energy multiplier and cosine multiplier cards in MCNP6 calculations with complex grid geometries. This procedure is described below.

A surface current tally (F1) was applied to both surfaces for each foil in the problem geometry to track the number of fast positrons entering the foils. A tally energy bin card (E card) was used to bin the incident fast positrons into 1000 logarithmically spaced energy groups from 1 keV to 10 MeV. The tabulated transmission and backscattering efficiencies were interpolated over the energy groups for the F1 tally and integrated with the incident fast positron current tallies using an energy multiplier (EM) card. A cosine multiplier (CM) card was also used with the F1 tally to reject contributions from fast positrons emerging from the surface of the foil and going into vacuum. Particles entering the foil were multiplied by 1 while particles leaving the foil were multiplied by 0 via the CM card (see Figure 5.3). In other words, only particles entering and stopping within a foil can contribute to emission of slow positrons from that foil. Positrons exiting a foil may still contribute to generation of slow positrons through surface tallies in adjacent foils.

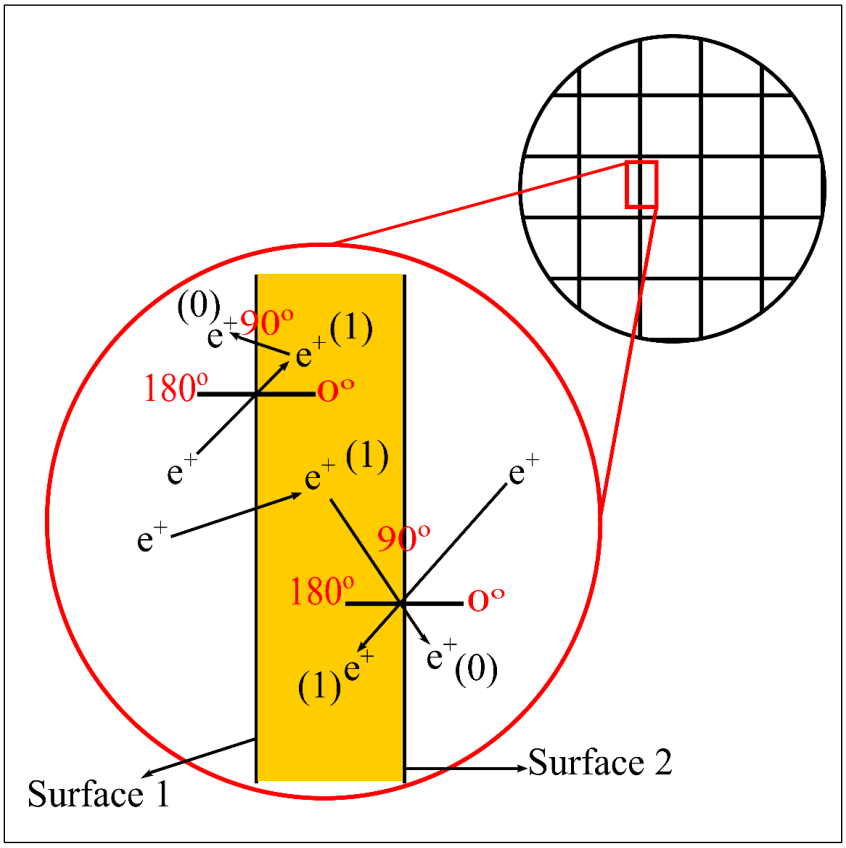

Figure 5.3. Cosine Multiplier Counting Only Positrons Entering a Tungsten Foil Within the Moderator Grid.

Table 5.1. Transmission Moderation Efficiencies for Different Tungsten Foil Thicknesses

	Efficiency ε_t							
t [µm]	**10 keV ($x10^{-3}$)**	**100 keV ($x10^{-3}$)**	**300 keV ($x10^{-3}$)**	**500 keV ($x10^{-3}$)**	**800 keV ($x10^{-3}$)**	**1 MeV ($x10^{-3}$)**	**5 MeV ($x10^{-4}$)**	**10 MeV ($x10^{-5}$)**
5	0	12.54	4.60	1.40	0.40	0.20	0.07	0
10	0	0.02	6.77	2.65	0.83	0.43	0.15	0
25	0	0	2.52	3.00	1.64	0.99	0.33	0
35	0	0	0.51	2.78	1.67	1.29	0.34	0

Table 5.1. Transmission Moderation Efficiencies for Different Tungsten Foil Thicknesses (cont.)

50	0	0	0.02	1.42	1.62	1.21	0.48	0.20
75	0	0	0	0.25	1.08	1.10	1.48	0.35
100	0	0	0	0.00	0.60	0.87	1.75	0.50
125	0	0	0	0	0.24	0.66	1.77	1.70

The interpolated thickness-dependent moderation efficiencies for transmitted positrons that were used in the MCNP tallies are given in Table 5.1.The moderation efficiencies for backscattered positrons that were used in MCNP simulation are given in Table 5.2

Table 5.2. Backscattering Moderation Efficiencies for Thickness of Tungsten (Thickness > 2 μm)

Positron energy (keV)	**Efficiency ε_b**
10	60.52×10^{-2}
100	5.10×10^{-3}
300	0.26×10^{-3}
500	0.65×10^{-4}
800	0.20×10^{-4}
1000	0.12×10^{-4}
5000	0.34×10^{-6}
10,000	0.98×10^{-7}

5.4. RESULTS AND DISCUSSION

The transmission and backscattering contributions to the slow positron current as a function of foil thickness are shown in Figure 5.4 for the grid with pitch size of 0.6 cm and length of 3 cm. The same results for the grid with pitch 0.3 cm and length 3 cm are shown in Figure 5.5 while the results for pitch 0.3 cm and length 6 cm are shown in Figure 5.6. Comparing these three results, it is evident that, for the given positron energy spectrum (Figure 4.1(b)), the backscattering contribution to the slow positron yield plateaus around 25 μm while the transmitted contribution is greatest for the thinnest foils. The total number of slow positrons emitted - which is most relevant as both transmitted and backscattered positrons can be extracted in the present design - exhibits a maximum at 5 to 10 μm thickness. Therefore a thickness of 10 μm was chosen as the nominally optimal thickness for subsequent calculations. The transmission contribution to the positron current decreases with increasing thickness of the tungsten grid. As Figures 5.4 and 5.5 show, increasing the mass of tungsten in the grid by increasing the number of moderator foils is a more efficient way of optimizing the source strength than increasing the foil thickness. Halving the pitch from 0.6 cm to 0.3 cm for 10 μm thick foils more than doubles the total slow positron yield while doubling the thickness from 10 to 20 μm while keeping the pitch fixed at 0.6 cm would have almost no effect on the source strength. Comparing Figures 5.5 and 5.6, one can see that for the same pitch and foil thickness, doubling the grid length less than doubles the yield. This is expected as there is some geometric attenuation in the fast positron flux further away from the Cd cup. Nevertheless, both the pitch and length can be more carefully optimized for a fixed foil thickness considering the effects of reflection probability and extraction voltage.

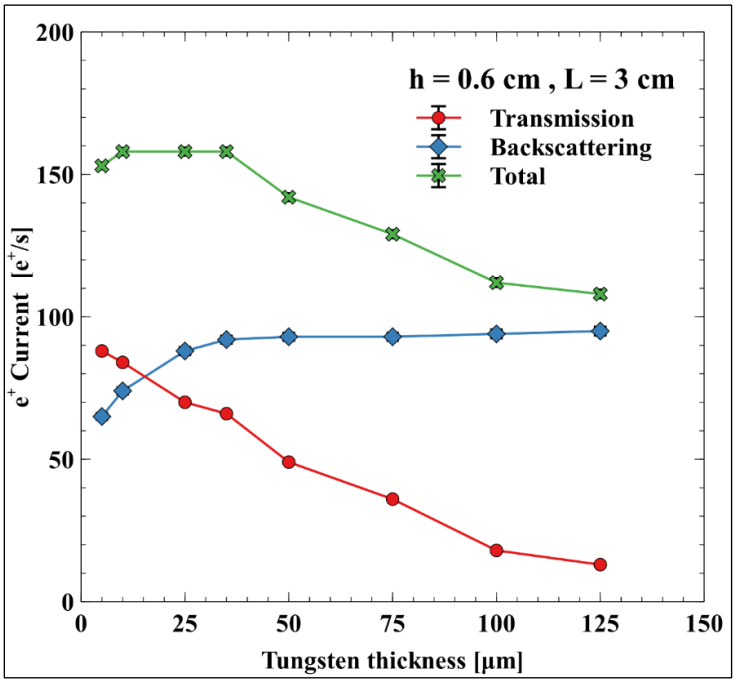

Figure 5.4. The Transmission, Backscattering, and Total Positron Current in a Tungsten Grid with Pitch 0.6 cm and Length 3 cm.

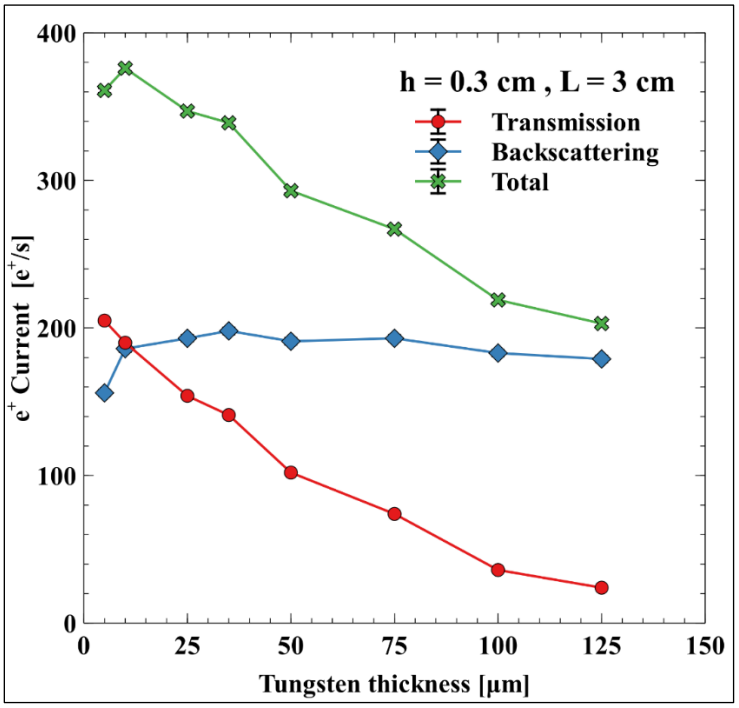

Figure 5.5. The Transmission, Backscattering, and Total Positron Current in a Tungsten Grid with Pitch 0.3 cm and Length 3 cm.

The configuration used in the data of Figure 5.7 is similar to that of Figure 5.6 except that instead of a single stage grid of length 6 cm, two 3 cm stages are used. Not surprisingly, the yield is lower than that shown in Figure 5.6 as the second 3 cm stage is further from the Cd cup than the second 3 cm of the 6 cm stage of Figure 5.6. The practical point must be made however, that such a configuration may still be advantageous in that it more easily permits for larger potential drops between stages, each stage being held at a different potential relative to ground and mitigating some of the electric field screening that may occur in a long conductive grid.

The total positron current calculated in these four designs is compared in Figure 5.8. The highest total slow positron current for all geometries was found for a pitch of 0.3 cm a length of 6 cm and thickness of 10 μm.

Figure 5.9 shows the transmission and backscattering contributions to the slow positron yields at each foil surface oriented perpendicular to the y-axis of the tungsten grid. All subfigures in Figure 5.9 have the same pitch (h = 0.3 cm) and foil thickness (thickness = 10 μm). The subfigures represent the yields for different foil thicknesses. The highest positron yield occurs in the middle layer in all Figures. As expected, from Figure 5.8 above, the largest slow positron yield is observed for the 6 cm long grid.

In Figure 5.9, the positron yield per foil increases roughly linearly (slightly sublinearly) with the length of the foil. This can be taken as evidence that the distribution of slow positrons is roughly uniform along each foil. Figure 5.10 also shows the slow positron yield per foil along the y-axis except for varying pitch sizes. The length is held fixed at 3 cm while the pitch varies from 0.1 to 0.6 cm.

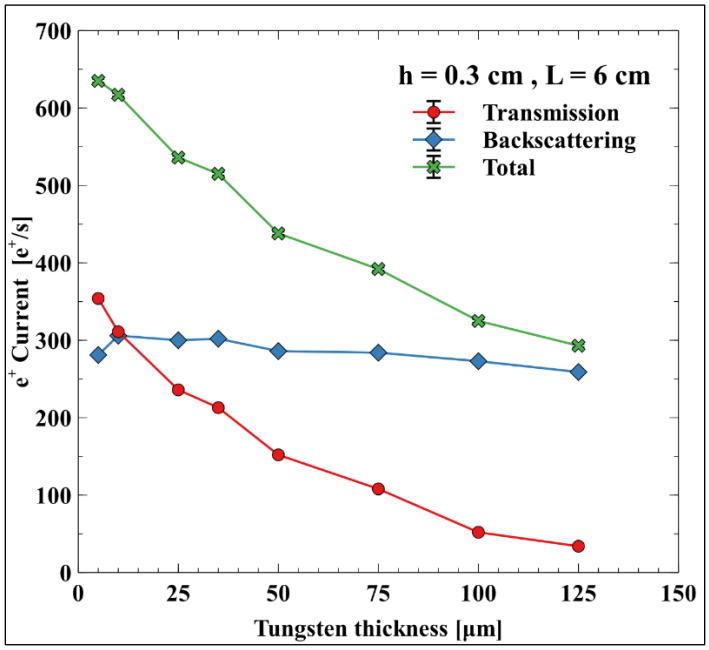

Figure 5.6. The Transmission, Backscattering, and Total Positron Current in a Tungsten Grid with Pitch 0.3 cm and Length 6 cm.

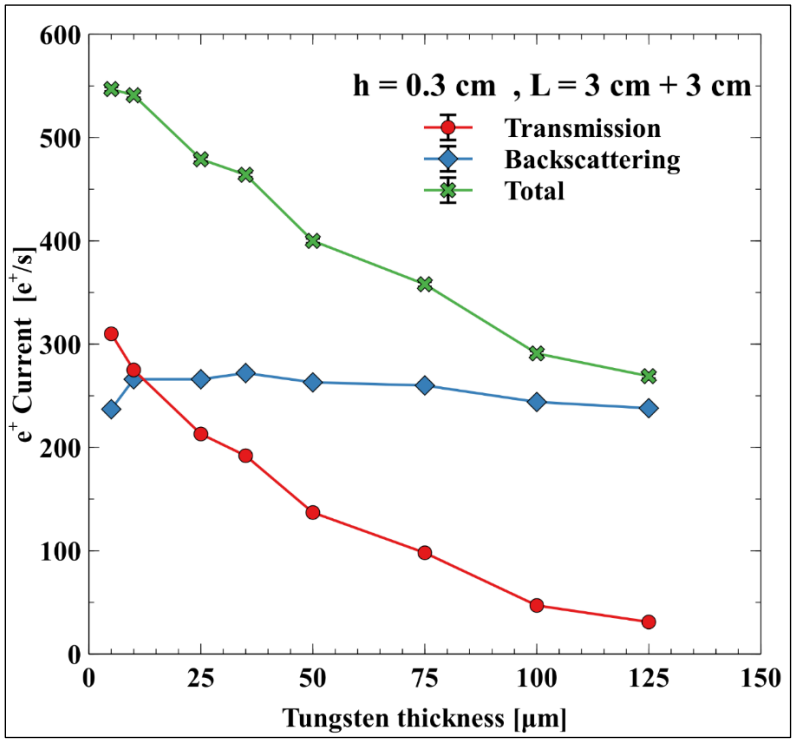

Figure 5.7. The Transmission, Backscattering, and Total Positron Current in a Two Stage Tungsten Grid with Pitch 0.3 cm and Length 3 + 3 cm.

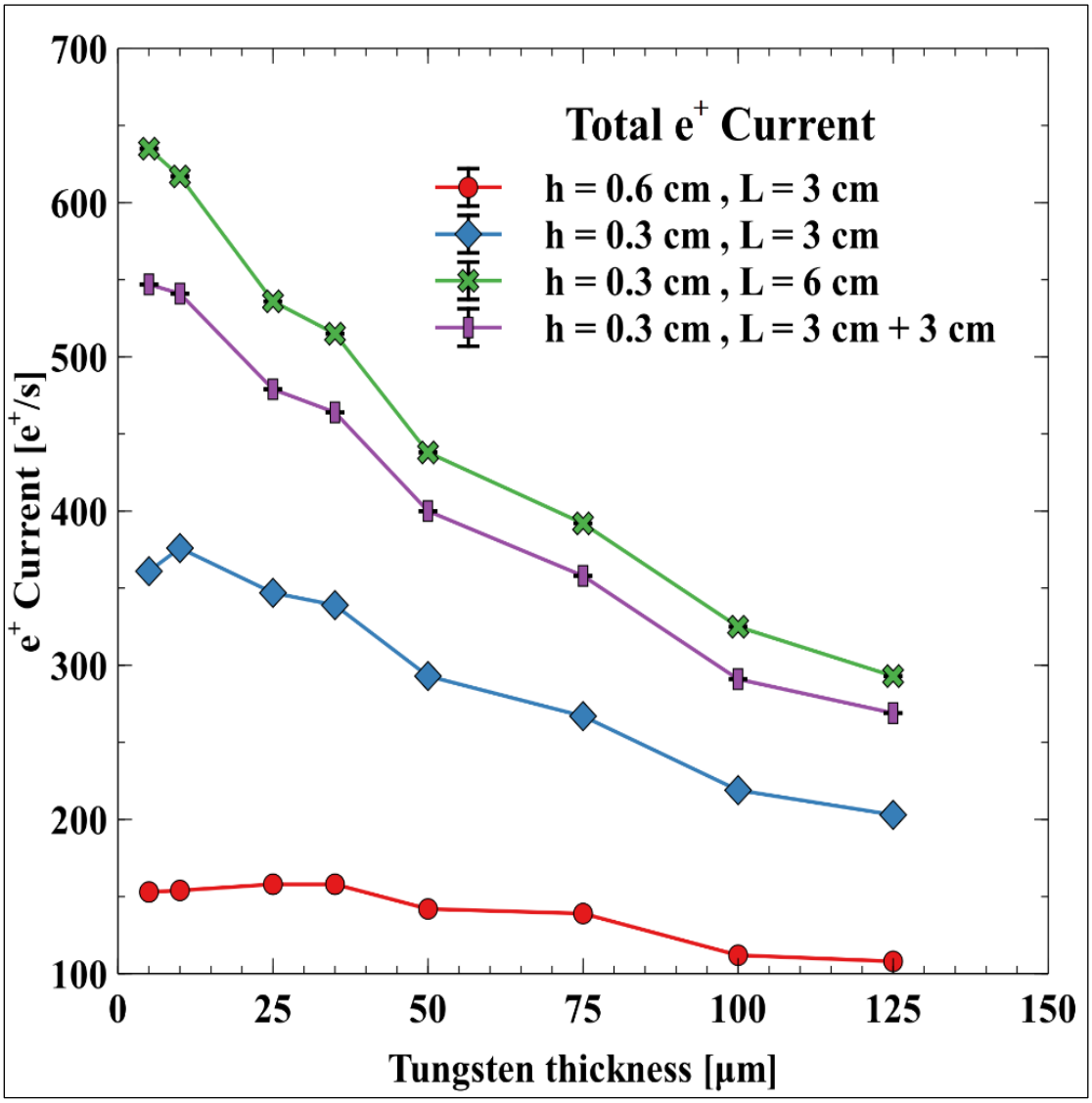

Figure 5.8. The Total Positron Current as a Function of Thickness for Four Grid Geometries.

Also, as expected from Figure 5.10, the smallest pitch size produces the largest number of slow positrons since the total number of foils is greater the closer together they are spaced. Interestingly, the yield per foil is also greater for smaller pitch sizes reflecting the fact that positron foils act as both gamma-to-e^+ converters as well as positron moderators.

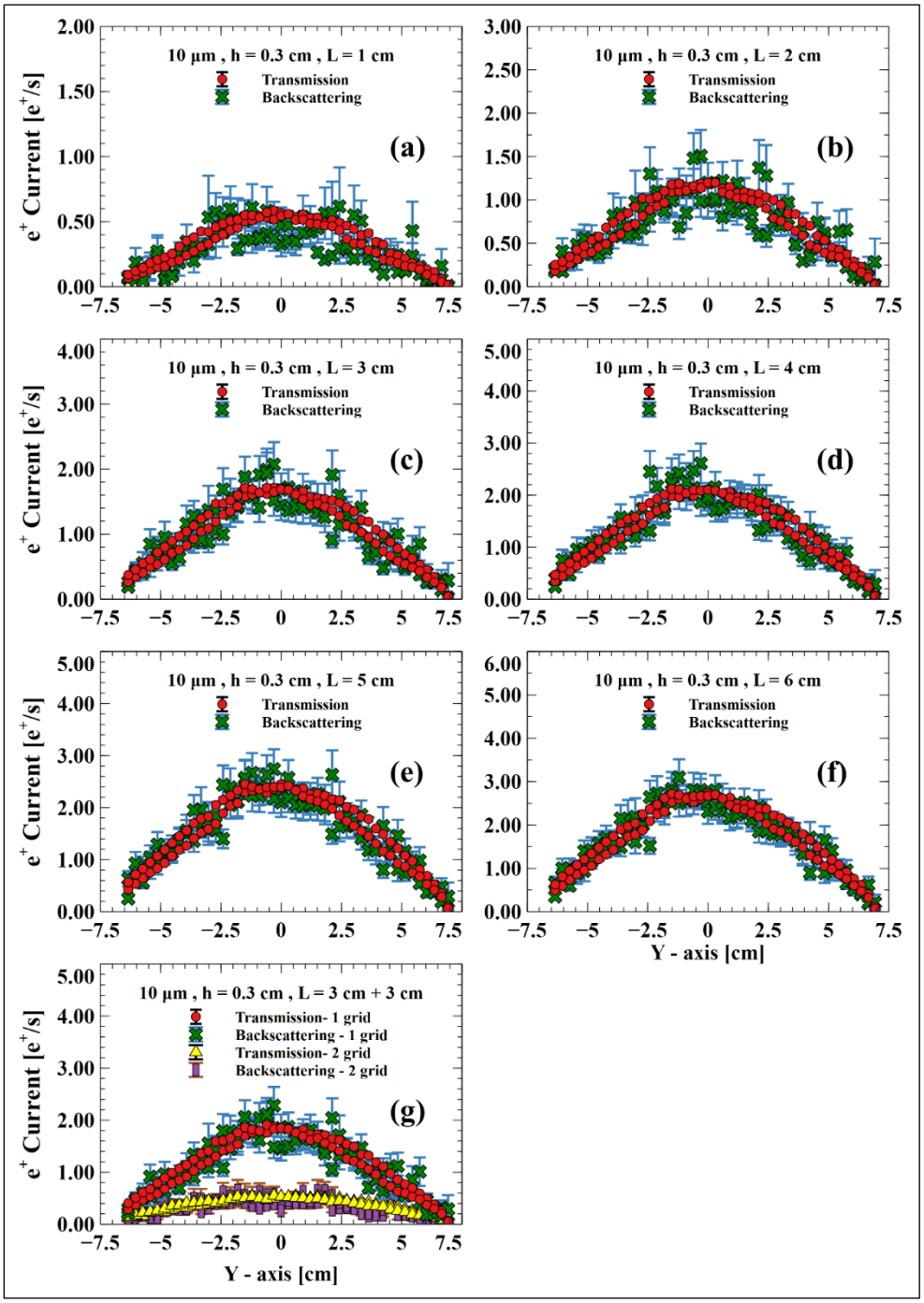

Figure 5.9. The Slow Positron Yields for Tungsten Foils Oriented Perpendicular to the Y-axis for Moderator Grids with Grid Lengths of 1 cm (a) 2 cm (b) 3 cm (c) 4 cm (d) 5 cm (e) 6 cm (f) 3+3 cm (g). The Foil Thickness and Pitch Sizes for Each Grid were 10 µm and 0.3 cm, Respectively.

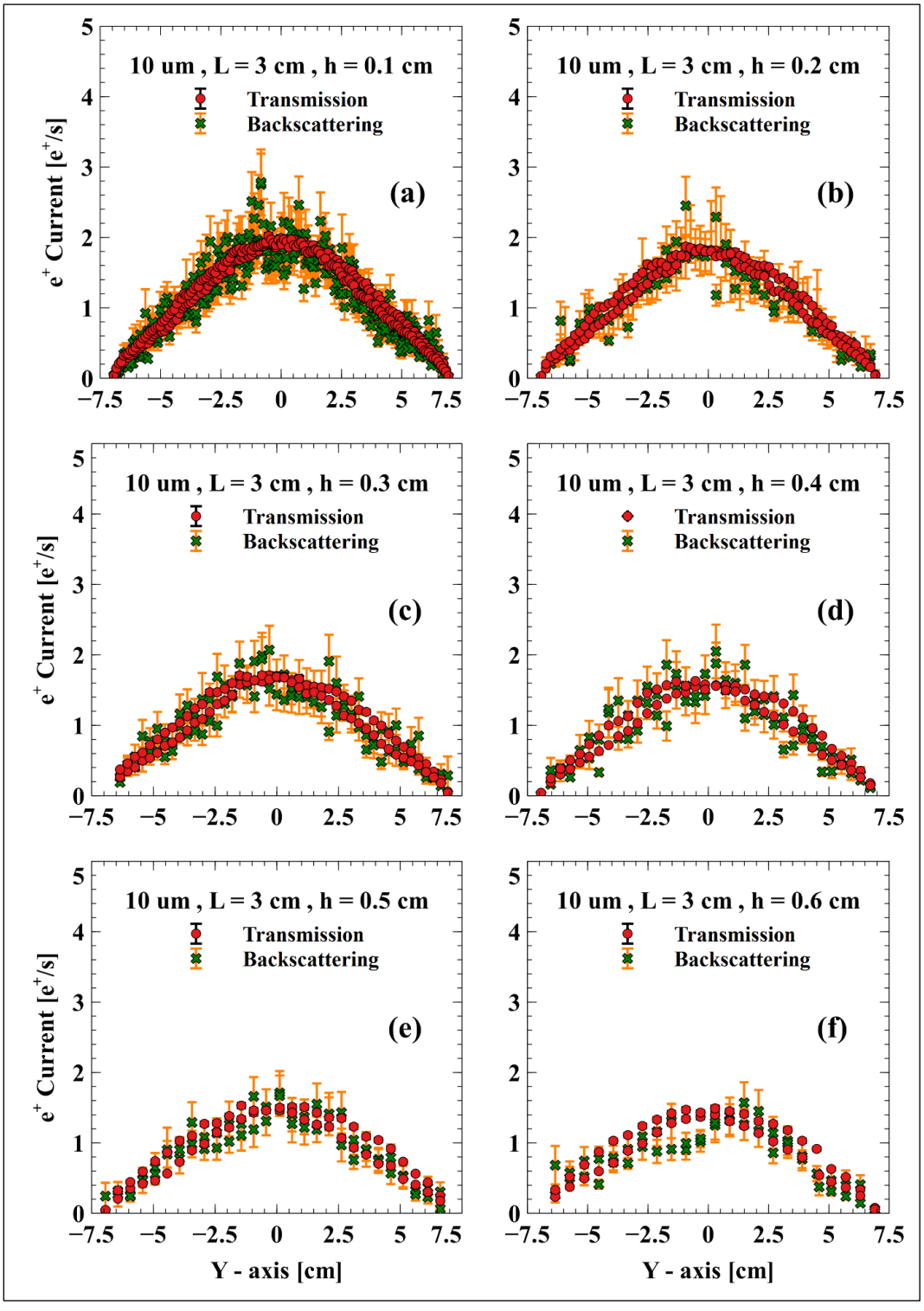

Figure 5.10. The Slow Positron Yields for Tungsten Foils Oriented Perpendicular to the Y-axis for Moderator Grids with Pitch Sizes of 0.1 cm (a) 0.2 cm (b) 0.3 cm (c) 0.4 cm (d) 0.5 cm (e) 0.6 cm (f). The Foil Thickness and Grid Lengths for Each Grid were 10 μm and 3 cm, Respectively.

To truly optimize the positron extraction, one should also consider loses incurred while extracting positrons from the grid. Based on the results above, it would appear to be the case that a small pitch and long moderator grid provides the largest yield of slow positrons. While this is true to an extent, small pitches and long grid also produce long and narrow channels that positrons must escape from before annihilating. In such channels, the positrons can be reflected many times, each time increasing the chances of annihilation or trapping in a surface potential. Thus while a large aspect ratio channel (length-to-pitch ratio) is desirable for slow positron yield, a small aspect ratio is desirable for improving the odds of positron extraction. In other words, a small L/h ratio decreases the number of reflections, n (see Equations 39 and 40).

The total extracted positron current as a function of extraction voltage was calculated for tungsten grids with 10 μm thick foils and 0.3 cm pitch for grid different lengths from 1 cm to 6 cm and assuming specular reflection (a = 0.5) (see Figure 5.11). The electric field in Equation 39 was taken to be the extraction voltage divided by the grid length. The reflection coefficient used was 0.55 [93] . In contrast to the results summarized in Figure 5.8, the 3 cm grid was found to give the highest yield from 100-300 V. From 300-700 V, the 4 cm grid performed best. Above 700 V, a 5 cm or greater grid is best. The optimal design of a tungsten moderator grid should, therefore, consider the available extraction voltage. It should also be mentioned that large extraction fields may be difficult to establish in thick grids as tungsten, being a conductor and tends to screen the electric field within the channel except near the ends where the electric field strength can be large due the edge effect. More detailed calculations using electrostatics solvers and single particle motion transport calculations may be beneficial in relating the

extracted positron current to the actual grid voltage. The assumption of a uniform electric field here also breaks down as the grid length increases and pitch decreases.

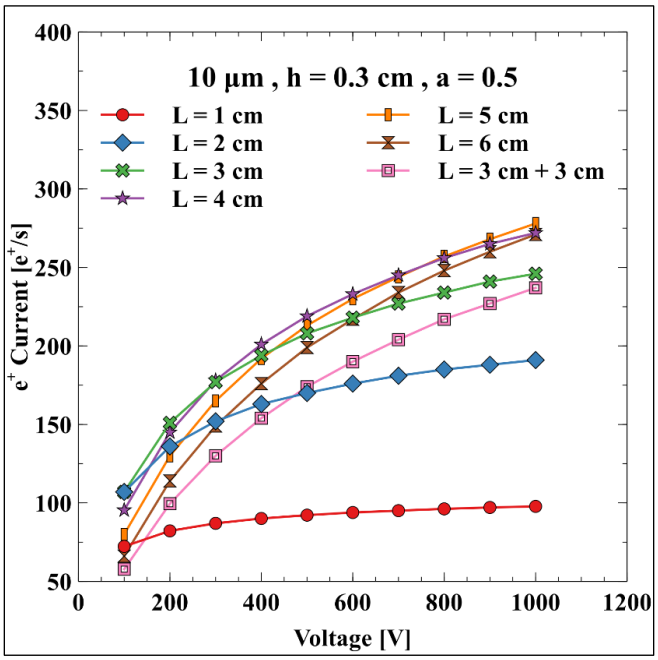

Figure 5.11. The Total Positron Current as a Function of Extraction Voltage for a 10 µm Thick Tungsten Grid with 0.3 cm Pitch and Various Grid Lengths. These Calculations Assume Specular Reflection (a = 0.5) with a Reflection Coefficient of 0.55.

The same calculations of extracted positron current were performed assuming non-specular reflection with a = 1. These are shown in Figure 5.12. The difference between the two reflection conditions is more pronounced for low extraction voltages. For non-specular reflection the extraction yield is lower. Qualitatively, the results are similar. The 3 cm tungsten grid is best suited for 300-600 V extraction voltage, while 2 cm performs better down to 100 V and 4 cm gives the best results up to 1000 V. The general conclusion that can be drawn from Figures. 5.11 and 5.12 is that for a single stage

moderator grid, the slow positron yield can be optimized by using as large an extraction potential as possible and matching the grid length to the potential.

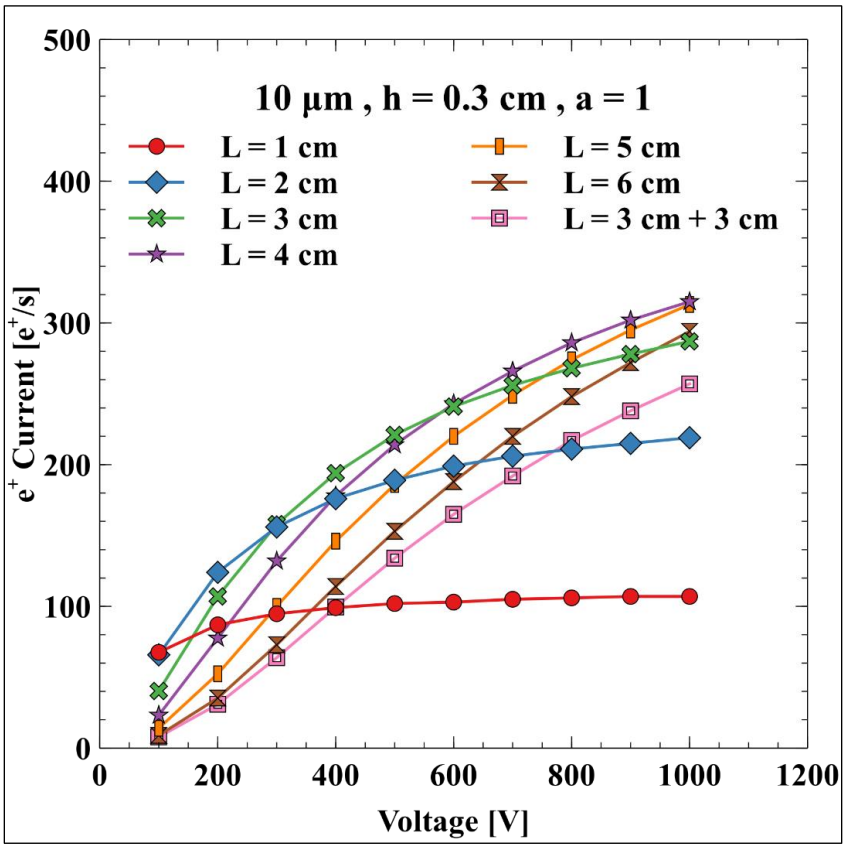

Figure 5.12. The Total Positron Current as a Function of Extraction Voltage for a 10 µm Thick Tungsten Grid with 0.3 cm Pitch and Various Grid Lengths. These Calculations Assume Non-Specular Reflection (a = 1) with a Reflection Coefficient of 0.55.

The practical limitations on strength of the electric field gradient that can be generated in a long and narrow conducting channel most likely introduce an additional constraint. Figure 5.13 shows the positron yield for a 3 cm long moderator grid with pitch ranging from 0.1 cm separation to 0.6 cm assuming specular reflection. Up to an extraction potential of about 400 V, the 0.2 cm gives the optimum yield. For higher voltages, 0.1 cm has the highest yield. Figure 5.14 shows the same calculations except for

non-specular reflection conditions. In this case, the 0.4 cm pitch has the best performance at low voltages. Comparing all results, one could say that for an extraction potential from 100-300 V a 3 cm long and 0.2 cm in pitch would be a nominally optimal grid geometry. As the extraction potential increases, the optimum yield is achieved with a larger aspect ratio channel (small pitch and longer grid). The actual number of positrons extracted is also expected to scale linearly with the thermal neutron flux. Though the beam port flux of the MSTR is comparatively weak (5×10^{6} cm^{-2} s^{-1} flux at full power) other reactor facilities with slow positron sources show similar source strengths when normalized by their flux. The Munich research reactor, FRM-II, has a thermal neutron flux up to 2×10^{14} cm^{-2} s^{-1} and a positron source strength of about 10^{10} positron per second [94]. The PULSTAR nuclear reactor at NC State University has a thermal flux of 2.5×10^{12} cm^{-2} s^{-1} and a positron source rate of 5.2×10^{8} positron per second [49]. Note that the positron source in the PULSTAR reactor is located near the fuel periphery. Scaling both neutron flux and extracted positron current by a factors of 10^{6} and 10^{8} gives order of magnitude agreement with these other facilities. In a previous MSTR core configuration where the fuel elements were located closer to the beam tube the average neutron flux at the beam port was measured to be 1.08×10^{8} n cm^{-2} s^{-1} [95]. Thus by reconfiguring the core, a source strength on the order of 10^{3} s^{-1} might be obtained. This is a weak source compared to some of those discussed in Section 2. Nevertheless, it may still be great enough in strength as to be useful for certain techniques using slow positrons. For example, with a compact linear accelerator, variable positron energy depth profiling techniques are possible.

A compact, variable energy Doppler Broadening of Annihilation Radiation (DBAR) system, for example, might be feasible. Such systems are used for defect depth profiling. DBAR systems require a high energy resolution gamma ray detector. Typically this means a High Purity Germanium Detector (HPGe). HPGe detectors have low inherent efficiencies (~1% at 511 keV is typical). Therefore it would be difficult to expect count rates greater than about tens of counts per second for a properly optimized positron source and fuel configuration. Such a count rate is on the lower end of usability. More detailed calculations considering loses in the accelerator optics, geometric efficiency of the detector(s) and interference from background counts should be considered to ascertain if such a system is truly feasible. Modern ACAR systems tend to have extremely low efficiencies and occupy a large amount of space making them unlikely candidates for MSTR.

An alternative approach to increase the positron intensity would be to locate the positron source closer to the fuel. This might be accomplished by removing the shutter assembly and lead shielding in the beam tube and inserting the positron source near the fuel. While this may be possible, additional biological shielding would likely be needed in the basement experimental area. Given that the biological shielding would need to attenuate unshielded neutrons and gamma rays from the beam tube, it is likely that the additional shielding would take up a substantial amount of space, which is already limited in the MSTR sub-level basement. Furthermore, such a modification of the beam tube would likely be semi-permanent and defeat the objective of making a modular apparatus that can be easily coupled and uncoupled from the beam port opening.

Another option would be to develop a source that can be lowered from above the core into a flux trap in the core. While such a configuration may produce an intense source of positrons, its design would likely be complicated by the fact that it would involve designing an approximately 20 ft long, vacuum system with high voltage electrostatic and possibly magnetostatic optical elements along its length.

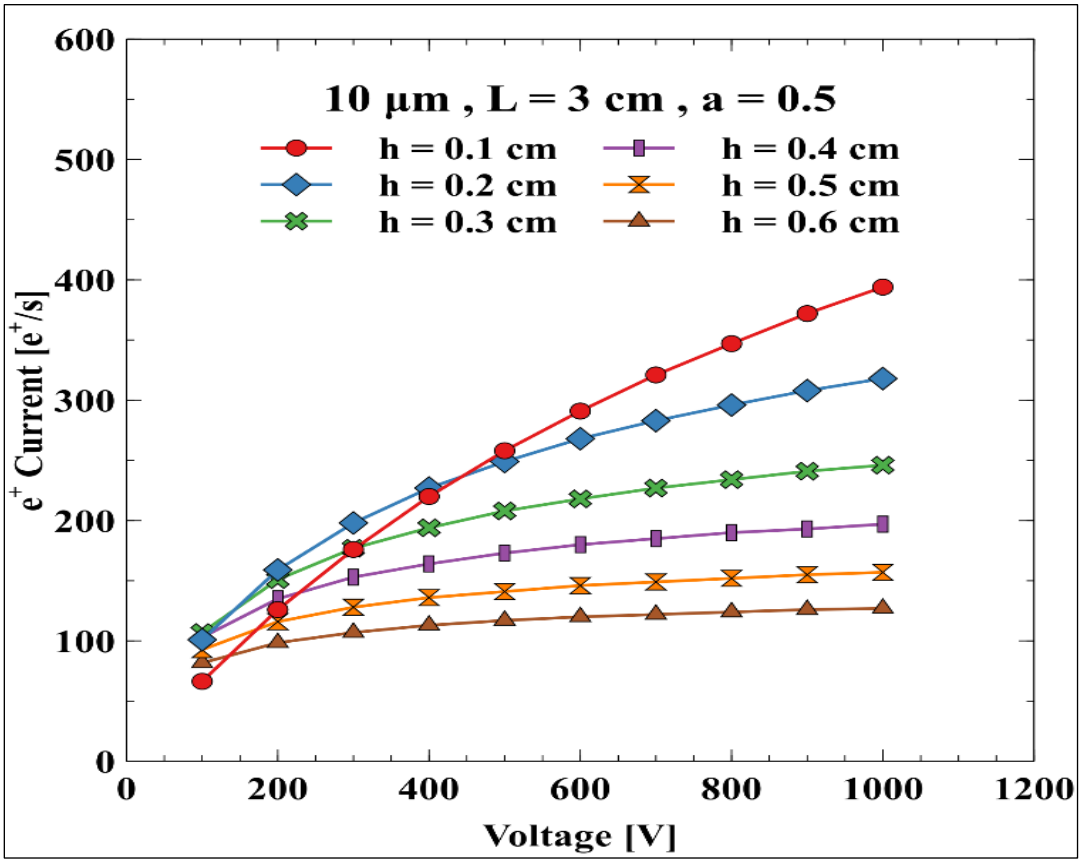

Figure 5.13. The Total Positron Current as a Function of Extraction Voltage for a 10 μm Thick Tungsten Grid with 3 cm. Length and Various Pitch. These Calculations Assume Specular Reflection (a = 0.5) with a Reflection Coefficient of 0.55.

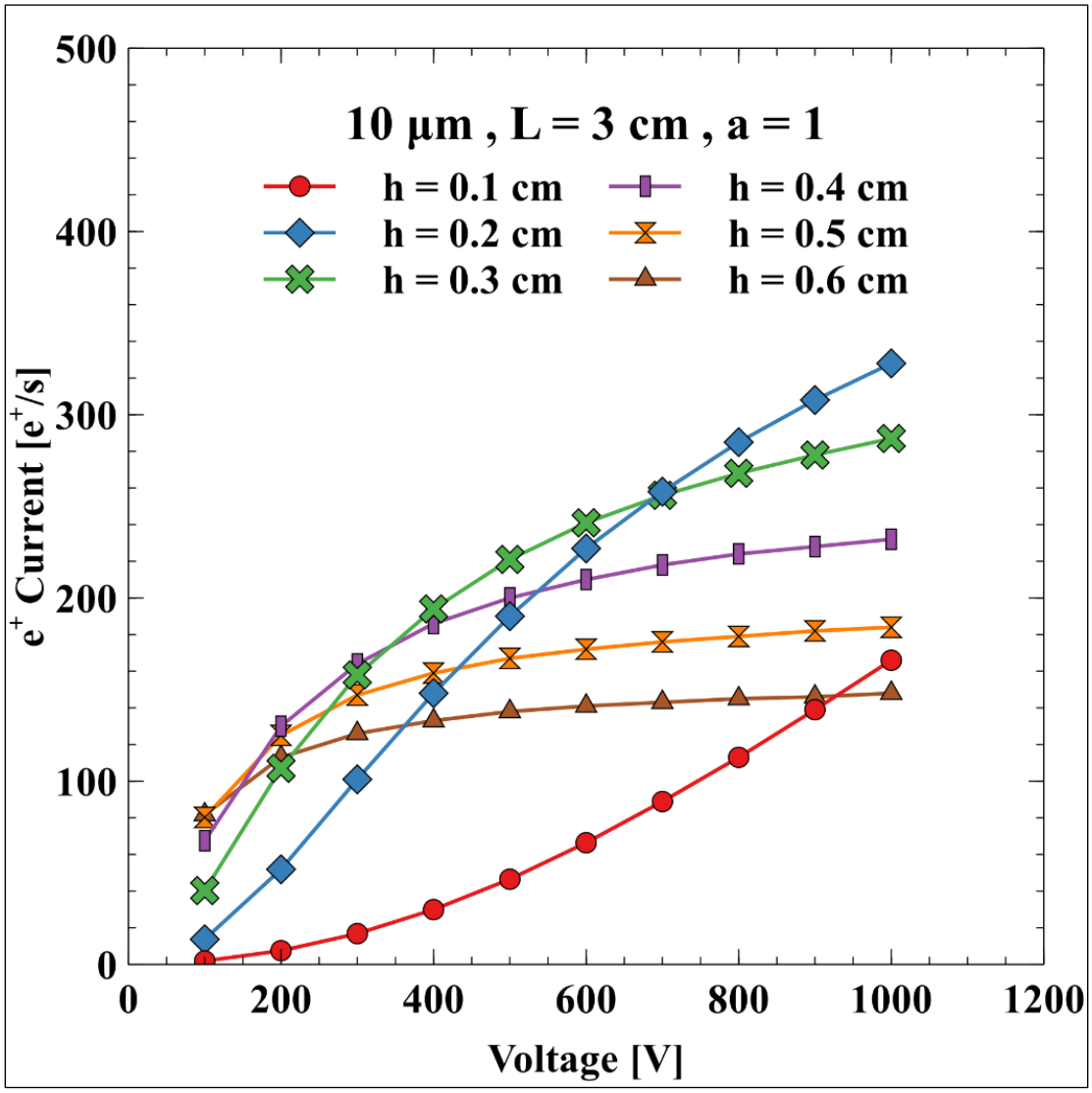

Figure 5.14. The Total Positron Current as a Function of Extraction Voltage for a 10 µm Thick Tungsten Grid with 3 cm Length and Various Pitch. These Calculations Assume Non-Specular Reflection (a = 1) with a Reflection Coefficient of 0.55.

6. CONCLUSIONS

This work explores the design and optimization of a slow positron source proposed for integration into the Missouri University of Science and Technology Reactor (MSTR). Several contributions to the scientific and engineering communities were made. A mixed analytical and numerical methodology for calculating the moderation efficiencies of foil positron moderators was introduced. Such calculations were used to obtain moderation efficiency tables in both the transmission and backscattering geometries for tungsten foils. These efficiency tables were then integrated into Monte Carlo radiation transport simulations for predicting the slow positron yield. The extraction efficiency of slow positrons by static electric fields was also considered in these calculations. Grid geometries were optimized to yield the highest intensity of positrons possible given the current MSTR core configuration. The neutron flux values used in the calculations were based on experimental characterization of the neutron beam port.

The thermal and epithermal flux components of the MSTR beam port were determined using the Neutron Activation Analysis of bare and cadmium filtered gold foils. Experimental results were also compared to MCNP calculations. Reasonable qualitative agreement was found in the spatial distribution of the flux though the MCNP values were systematically lower than the experimental results by about 29%, on average. Most of the discrepancy is attributed to the fuel material definition cards in the model which assume that all of the MSTR fuel is fresh.

The moderation efficiencies for the production of thermal positrons by thin tungsten foils were calculated by first performing Monte Carlo simulations of positron stopping in tungsten and subsequently integrating best fit Makhovian profiles with efficiency kernels derived from Green's function solutions of the 3D diffusion Equation for an infinite slab geometry. The efficiencies for both the transmitted and backscattering geometries as functions of energy, angle and foil thickness were tabulated. The resulting efficiencies showed excellent agreement with results from authors assuming the same diffusion length and branching ratio. Discrepancies with other values found in the literature can most likely be ascribed to wide variations in moderator foil quality. The availability of these tabulated efficiencies can be helpful in the design of tungsten moderators and the prediction of their efficiency for a positron flux with arbitrary energy and angular dependence.

The yield of extracted slow positrons from a tungsten moderator grid at a nuclear reactor-based slow positron source was calculated for different geometries of tungsten grid using Monte Carlo simulations with tabulated moderator efficiencies. The positron current decreases as the thickness of tungsten foils in the grid increase due to increased loses from annihilation in the foils. A 10 μm thick tungsten foil was found to produce the highest number of positrons for the positron energy spectrum generated by a Cd (n,γ) converter with pair production occurring in W. The foil-to-foil pitch size as well as the foil length (grid length) were varied to maximize the positron yield. Considering the physics of positron reflection as well as electrostatic extraction, the predicted positron yield vs. extraction voltage curves were calculated and used to determine the optimal moderator geometry for a given extraction voltage. A 3 cm in length by 0.2 cm pitch

moderator grid is the optimal geometry for 300 V extraction potential. As the extraction potential increases, the positron yield also increases as does the optimum aspect ratio of the grid channels. The maximum extraction voltage is likely limited by other practical constraints such as dielectric breakdown voltage.

Overall, in its current fuel configuration, the MSTR cannot provide a large enough flux to generate more than a weak source of slow positrons. Changing the core configuration to bring the fuel elements closer to the beam port would likely produce a significantly stronger source, probably in the range of a few thousand slow positrons per second. While still orders of magnitude smaller than the strongest positron sources at other facilities in the world, such a source may still be useful for certain select applications using slow positrons such as variable energy Doppler Broadening Annihilation Radiation (DBAR) for defect depth profiling.

APPENDIX

The calculation of the positron moderation efficiencies for both transmitted and backscattered foil geometries is based on finding Green's function solutions to the diffusion Equation for a positron stopped at position $\boldsymbol{r}'$

$$D_+\nabla^2 C_+(\boldsymbol{r}) - \frac{1}{\tau_+} C_+(\boldsymbol{r}) + \delta(\boldsymbol{r}-\boldsymbol{r}') = 0 \tag{A.1}$$

D_+ is the thermal positron diffusion coefficient, τ_+ is the positron lifetime and C_+ is the volumetric concentration of positrons (number density). The Green's function solution to Equation A.1 in an infinite medium is

$$G(\boldsymbol{r}-\boldsymbol{r}') = \frac{\exp\left(-\frac{|\boldsymbol{r}-\boldsymbol{r}'|}{L_+}\right)}{4\pi D_+ |\boldsymbol{r}-\boldsymbol{r}'|} \tag{A.2}$$

$$L_+ = \sqrt{D_+\tau_+} \tag{A.3}$$

L_+ is the diffusion length. For a single point source constrained to lie along the z-axis in a cylindrical coordinate system the Green's function solution is

$$g(\rho, z-z') = \frac{\exp\left(-\frac{\sqrt{\rho^2+(z-z')^2}}{L_+}\right)}{4\pi D_+ \sqrt{\rho^2+(z-z')^2}} \tag{A.4}$$

In the problem of interest, the positrons are deposited in a thin foil rather than an infinite medium. Since the thickness of the foil is typically orders of magnitude smaller than the area of the foil (microns versus centimeters), we treat the problem geometry as a slab with thickness *L* having infinite extent perpendicular to the z-axis. Positrons that do not annihilate eventually diffuse to the surface of the foil. A general (Robin) boundary condition at the surface of the foil is given by

$$D_+ \boldsymbol{n} \cdot \nabla C_+(\boldsymbol{r})|_{z=0 \text{ or } L} = -\alpha C_+(\boldsymbol{r})|_{z=0 \text{ or } L} \quad \text{(A.5)}$$

where $\boldsymbol{n}$ is the surface normal and α governs whether the boundary is fully reflecting ($\alpha = 0$, i.e. Neumann b.c.) or fully absorbing ($\alpha = \infty$, i.e. Dirichlet b.c.) or a mixture of reflecting and absorbing. Considering that positrons are likely to either be trapped in surface states, form free positronium or be spontaneously emitted by the negative work function – all forms which remove their identity as migrating thermal positrons – fully absorbing boundary conditions are a reasonable choice and adopted here. The boundary conditions then become

$$C_+(\boldsymbol{r})|_{z=0} = 0 \quad \text{(A.6)}$$

$$C_+(\boldsymbol{r})|_{z=L} = 0 \quad \text{(A.7)}$$

Assuming these Dirichlet boundary conditions, one must find a new Green's function solution to the diffusion Equation (Equation A.1). This is done using the method of images, recasting the single slab problem into an infinite medium problem with an array of positive and negative delta function source terms arranged in such a way that the positron concentration vanishes whenever $z = Ln$, where n is an integer. This is illustrated in Figure. A.1

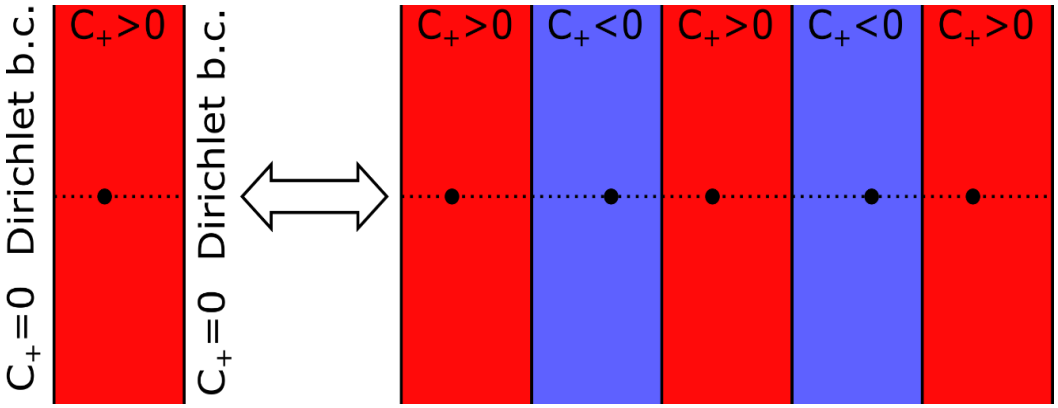

Figure A.1. Recasting Infinite Slab Diffusion Problem into an Infinite Medium with Images.

The red domains are shifted copies of the original infinite slab with positive valued solution. The solutions in the blue domains are inverted and negative.

Note that in this method, the domain is split into positive solution regions and negative solution regions. Only the positive solution region $z \in (0, L)$ is physically meaningful and will be taken as the solution of the original slab problem. The Green's function of the slab problem, G_+, is then a superposition of the positive and negative solutions of the diffusion Equation in an infinite medium, shifted by an amount corresponding to each domain.

$$G_+(\rho, z - z') = \sum_{n=-\infty}^{\infty} [g(\rho, z - 2Ln - z') - g(\rho, z - 2Ln + z')] \qquad \text{(A.8)}$$

For any interface between positive and negative domains, there is an antisymmetric arrangement of sources that ensures that the positron concentration at the interface cancels out. The current through the surface at $z = 0$ is given by the area integral

$$J(z') = D_+ \int da \frac{\partial G_+}{\partial z}\Big|_{z=0} = D_+ \int_0^{2\pi} \int_0^{\infty} \frac{\partial G_+}{\partial z}\Big|_{z=0} \rho d\rho d\varphi \tag{A.9}$$

Applying the z derivatives to the sum in Equation A.8 introduces terms like

$$D_+ \frac{\partial g}{\partial z} = -\frac{(z-z')\exp\left(-\frac{\sqrt{\rho^2+(z-z')^2}}{L_+}\right)}{4\pi[\rho^2+(z-z')^2]}\left(\frac{1}{L_+} + \frac{1}{\sqrt{\rho^2+(z-z')^2}}\right) \tag{A.10}$$

$$D_+ \frac{\partial g}{\partial z}\Big|_{z=0} = \frac{z'\exp\left(-\frac{\sqrt{\rho^2+z'^2}}{L_+}\right)}{4\pi(\rho^2+z'^2)}\left(\frac{1}{L_+} + \frac{1}{\sqrt{\rho^2+z'^2}}\right) \tag{A.11}$$

When performing the integrals over ρ, it is helpful to use the following substitution of variables

$$u = \frac{\sqrt{\rho^2+z'^2}}{L_+} \tag{A.12}$$

$$du = \frac{1}{L_+^2 u}\rho d\rho \tag{A.13}$$

$$j(z') = D_+ \int_0^{2\pi} \int_0^{\infty} \frac{\partial g}{\partial z}\Big|_{z=0} \rho d\rho d\varphi \tag{A.14}$$

which can be thought of as the partial current from one of the point sources

$$j(z') = \frac{z'}{2L_+} \int_{\frac{|z'|}{L_+}}^{\infty} \exp(-u)\left(\frac{1}{u} + \frac{1}{u^2}\right) du \tag{A.15}$$

This integral can be evaluated by the method of integration by parts

$$j(z') = \frac{z'}{2|z'|}\exp\left(-\frac{|z'|}{L_+}\right) \tag{A.16}$$

$$= z'\frac{1}{2}f(|z'|) \tag{A.17}$$

Inserting these back into the sum in Equation A.8

$$J_+(z') = \sum_{n=-\infty}^{\infty}[j(2Ln + z') - j(2Ln - z')] \tag{A.18}$$

$$= \frac{1}{2}\sum_{n=-\infty}^{\infty}[(2Ln + z')f(|2Ln + z'|) - (2Ln - z')f(|2Ln - z'|)] \tag{A.19}$$

$$= \frac{1}{2}\sum_{n=1}^{\infty}[(2Ln + z')f(2Ln + z') - (2Ln - z')f(2Ln - z')] +$$

$$\frac{1}{2}\sum_{n=1}^{\infty}[-(2Ln - z')f(2Ln - z') + (2Ln + z')f(2Ln + z')] \tag{A.20}$$

$$+ \exp\left(-\frac{z'}{L_+}\right)$$

$$J_+(z') = \sum_{n=1}^{\infty}\left[\exp\left(-\frac{2Ln + z'}{L_+}\right) - \exp\left(-\frac{2Ln - z'}{L_+}\right)\right] + \exp\left(-\frac{z'}{L_+}\right) \tag{A.21}$$

$$J_+(z') = \exp\left(-\frac{z'}{L_+}\right) - 2\sinh\left(\frac{z'}{L_+}\right)\sum_{n=1}^{\infty}\exp\left(-\frac{2Ln}{L_+}\right) \tag{A.22}$$

$$J_+(z') = \exp\left(-\frac{z'}{L_+}\right) - 2\sinh\left(\frac{z'}{L_+}\right)\sum_{n=1}^{\infty}\exp^n\left(-\frac{2L}{L_+}\right) \tag{A.23}$$

Seeing that the summation in Equation A.23 is a convergent geometric series the current has the following closed forms

$$J_+(z') = \exp\left(-\frac{z'}{L_+}\right) - 2\sinh\left(\frac{z'}{L_+}\right)\frac{\exp\left(-\frac{2L}{L_+}\right)}{1-\exp\left(-\frac{2L}{L_+}\right)} \tag{A.24}$$

$$J_+(z') = \exp\left(-\frac{z'}{L_+}\right) - \exp\left(-\frac{L}{L_+}\right)\frac{\sinh\left(\frac{z'}{L_+}\right)}{\sinh\left(\frac{L}{L_+}\right)} \tag{A.25}$$

Given that the source term is a Dirac delta function of unit strength, this current may be regarded as the probability that a positron stopping at a depth z' diffuses towards the surface at $z = 0$. In other words it is a kernel that might be convolved with the stopping profile to give the fraction or efficiency of stopped positrons reaching a free surface as slow positrons. Defining the beam direction as oriented along the positive z direction, this expression in the backscattering geometry, J_+^{b} becomes

$$J_+^{\mathrm{b}}(z'; L) = \exp(-z') - \exp\left(-\frac{L}{L_+}\right)\frac{\sinh\left(\frac{z'}{L_+}\right)}{\sinh\left(\frac{L}{L_+}\right)} \tag{A.26}$$

The current in the transmitted geometry, J_+^{t}, can be obtained by noting that

$$J_+^{\mathrm{t}}(z') = J_+^{\mathrm{b}}(L - z') \tag{A.27}$$

$$J_+^{\mathrm{t}}(z'; L) = \exp\left(-\frac{L-z'}{L_+}\right) - \exp\left(-\frac{L}{L_+}\right)\frac{\sinh\left(\frac{L-z'}{L_+}\right)}{\sinh\left(\frac{L}{L_+}\right)} \tag{A.28}$$

Normalizing the projected stopping profile by the number of source particles, one gets a probability distribution function $p(z)$ giving the probability of a positron becoming thermalized (stopping) at z. The efficiency of the foil is then

$$\varepsilon^{i}(L) = Y_0 \int_0^L J_+^i(z'; L) p(z') dz' \tag{A.29}$$

where i indicates either the backscattered or transmitted contribution to the current of thermalized positrons and Y_0 is a branching ratio for thermal positron emission.

BIBLIOGRAPHY

1. Dirac, P.A.M., A theory of electrons and protons. Proceedings of the Royal Society of London. Series A, Containing papers of a mathematical and physical character, 1930. 126(801): p. 360-365.

2. Anderson, C.D., Cosmic-ray positive and negative electrons. Physical Review, 1933. 44(5): p. 406.

3. Charlton, M. and J.W. Humberston, Positron physics. Vol. 11. 2001: Cambridge University Press.

4. Krause-Rehberg, R. and H.S. Leipner, Positron annihilation in semiconductors: defect studies. Vol. 127. 1999: Springer Science & Business Media.

5. Berko, S., R. Silver, and P. Sokol, Momentum distributions. Plenum Press, New York, 1989: p. 273.

6. Zeman, A., et al., High intensity positron source at HFR: Basic concept, scoring and design optimisation. Nuclear Instruments and Methods in Physics Research Section B: Beam Interactions with Materials and Atoms, 2012. 271: p. 19-26.

7. David, A., et al., Lifetime measurements with a scanning positron microscope. Physical Review Letters, 2001. 87(6): p. 067402.

8. Bailey, D.L., et al., Positron emission tomography. 2005: Springer.

9. Siegel, R., Positron annihilation spectroscopy. Annual Review of Materials Science, 1980. 10(1): p. 393-425.

10. Schultz, P.J. and K.G. Lynn, Interaction of positron beams with surfaces, thin films, and interfaces. Reviews of Modern Physics, 1988. 60(3): p. 701.

11. Asoka-Kumar, P., et al., Increased elemental specificity of positron annihilation spectra. Physical Review Letters, 1996. 77(10): p. 2097.

12. https://www.hzdr.de/db/Cms?pOid=35245&pNid=3225.

13. http://positrons.physics.lsa.umich.edu/nanopos/PALS-intro/psitronphysics.htm.

14. Kubica, P. and A. Stewart, Thermalization of positrons and positronium. Physical Review Letters, 1975. 34(14): p. 852.

15. Vehanen, A., et al., Profiling multilayer structures with monoenergetic positrons. Physical Review B, 1987. 35(10): p. 4606.

16. Nielsen, B., et al., Positron diffusion in Si. Physical Review B, 1985. 32(4): p. 2296.

17. Van Veen, A., et al., Testing of a nuclear-reactor-based positron beam. Applied surface science, 1997. 116: p. 39-44.

18. Nieminen, R. and C. Hodges, Positron work functions in transition metals. Solid State Communications, 1976. 18(8): p. 1115-1118.

19. Coleman, P.G., Positron beams and their applications. 2000: World Scientific.

20. Kluin, J., et al., Ortho-positronium lifetime studies of free volume in polycarbonates of different structures: influence of hole size distributions. Macromolecules, 1993. 26(8): p. 1853-1861.

21. Halpern, O., Magnetic quenching of the positronium decay. Physical Review, 1954. 94(4): p. 904.

22. Hugenschmidt, C., Positrons in surface physics. Surface Science Reports, 2016. 71(4): p. 547-594.

23. https://www.doseinfo-radar.com/RADARDecay.html.

24. Hugenschmidt, C., et al. Intense positron source at the Munich research reactor FRM-II. in Materials Science Forum. 2001. Trans Tech Publ.

25. Krane, K. S., & Halliday, D. (1987). Introductory nuclear physics.

26. M.J. Berger, J.H.H., S.M. Seltzer, J. Chang, J.S. Coursey, R. Sukumar, D.S. Zucker, and K. Olsen, XCOM: Photon Cross Sections Database - NIST Standard Reference Database 8 (XGAM). 2010.

27. Howell, R. H., Alvarez, R. A., & Stanek, M. (1982). Production of slow positrons with a 100-MeV electron linac. Applied Physics Letters, 40(8), 751-752.

28. Akahane, T., Chiba, T., Shiotani, N., Tanigawa, S., Mikado, T., Suzuki, R., ... & Tomimasu, T. (1990). Stretching of slow positron pulses generated with an electron linac. Applied Physics A, 51(2), 146-150.

29. Kuroda, R., Sei, N., Yasumoto, M., Toyokawa, H., Ogawa, H., Koike, M., & Yamada, K. (2008). Generation of 0.1 THz coherent synchrotron radiation with compact S-band linac at AIST. Infrared Physics & Technology, 51(5), 390-393.

30. Krause-Rehberg, R., et al., EPOS—An intense positron beam project at the ELBE radiation source in Rossendorf. Applied Surface Science, 2006. 252(9): p. 3106-3110.

31. Howell, R. H., Rosenberg, I. J., & Fluss, M. J. (1987). Production and use of low-energy, monoenergetic positron beams from electron linacs. Applied Physics A, 43(4), 247-255.

32. Falub, C. V., Eijt, S. W. H., Mijnarends, P. E., Schut, H., & Van Veen, A. (2002). Magnetic focusing of an intense slow positron beam for enhanced depth-resolved analysis of thin films and interfaces. Nuclear Instruments and Methods in Physics Research Section A: Accelerators, Spectrometers, Detectors and Associated Equipment, 488(3), 478-492.

33. Hathaway, A. G., Skalsey, M., Frieze, W. E., Vallery, R. S., Gidley, D. W., Hawari, A. I., & Xu, J. (2007). Implementation of a prototype slow positron beam at the nc state university pulstar reactor. Nuclear Instruments and Methods in Physics Research Section A: Accelerators, Spectrometers, Detectors and Associated Equipment, 579(1), 538-541.

34. Hugenschmidt, C., et al., The neutron induced positron source at Munich–NEPOMUC. Nuclear Instruments and Methods in Physics Research Section B: Beam Interactions with Materials and Atoms, 2004. 221: p. 160-164.

35. Stein, T., W. Kauppila, and L. Roellig, Production of a monochromatic, low energy positron beam using the 11B (p, n) 11C reaction. Review of Scientific Instruments, 1974. 45(7): p. 951-953.

36. Xie, R., et al., Production of a low energy positron beam using the 12C (d, n) 13N reaction. Nuclear Instruments and Methods in Physics Research Section B: Beam Interactions with Materials and Atoms, 1994. 93(1): p. 98-102.

37. Hunt, A., et al., The development of the intense positron beam at Washington State University. Applied surface science, 2002. 194(1-4): p. 296-300.

38. Cassidy, D., et al., Positron beam production with a deuteron accelerator. Nuclear Instruments and Methods in Physics Research Section B: Beam Interactions with Materials and Atoms, 2002. 195(3-4): p. 442-448.

39. Hirose, M. and T. Nakajyo, The SHI slow positron beam facility with a compact cyclotron. Applied surface science, 1999. 149(1-4): p. 24-29.

40. Hirose, M., M. Washio, and K. Takahashi, Production of an intense slow positron beam using a compact cyclotron. Applied Surface Science, 1995. 85: p. 111-117.

41. Saito, F., et al., Spot 18F positron source electro-deposited on a graphite rod. Nuclear Instruments and Methods in Physics Research Section A: Accelerators, Spectrometers, Detectors and Associated Equipment, 2000. 450(2-3): p. 491-494.

42. Saito, F., et al., Automatic 18F positron source supply system for a monoenergetic positron beam. Radiation Physics and Chemistry, 2000. 58(5-6): p. 755-757.

43. Gräff, G., et al., Intense source of slow positrons from pulsed electron accelerators. Applied Physics A, 1984. 33(1): p. 59-62.

44. Wada, K., et al., Increase in the beam intensity of the linac-based slow positron beam and its application at the Slow Positron Facility, KEK. The European Physical Journal D, 2012. 66(2): p. 37.

45. Yamazaki, T., et al., Production and application of pulsed slow positron beam using an electron linac. Radiation Physics and Chemistry, 1997. 49(6): p. 651-659.

46. Chen, H., et al., Intense slow positron production at the 15 MeV LINAC at Argonne National Laboratory. Applied surface science, 2006. 252(9): p. 3159-3165.

47. Hugenschmidt, C., et al., The NEPOMUC upgrade and advanced positron beam experiments. New Journal of Physics, 2012. 14(5): p. 055027.

48. Lynn, K., et al., A high intensity positron beam at the Brookhaven reactor, in Atomic physics with positrons. 1987, Springer. p. 161-174.

49. Moxom, J., A.G. Hathaway, and A.I. Hawari. Out of core testing of the North Carolina State University PULSTAR reactor positron beam. in Nuclear Science Symposium Conference Record, 2007. NSS'07. IEEE. 2007. IEEE.

50. Hawari, A.I., et al. Operation and testing of the PULSTAR reactor intense slow positron beam and PALS spectrometers. in Journal of Physics: Conference Series. 2011. IOP Publishing.

51. Hathaway, A., et al., Implementation of a prototype slow positron beam at the nc state university pulstar reactor. Nuclear Instruments and Methods in Physics Research Section A: Accelerators, Spectrometers, Detectors and Associated Equipment, 2007. 579(1): p. 538-541.

52. Zeman, A., et al. Scoring Analysis of Design, Verification and Optimization of High Intensity Positron Source (HIPOS). in Materials Science Forum. 2013. Trans Tech Publ.

53. Schut, H., et al. Long term performance of the reactor based positron beam POSH. in Materials Science Forum. 2004. Trans Tech Publ.

54. Van Veen, A., et al., Positron extraction and transport in a nuclear-reactor-based positron beam. Nuclear Instruments and Methods in Physics Research Section A: Accelerators, Spectrometers, Detectors and Associated Equipment, 1999. 427(1-2): p. 266-270.

55. de Lucio, O., et al., Study of tungsten based positron moderators. Nuclear Instruments and Methods in Physics Research Section B: Beam Interactions with Materials and Atoms, 2015. 354: p. 116-119.

56. Lynn, K., B. Nielsen, and J. Quateman, Development and use of a thin-film transmission positron moderator. Applied Physics Letters, 1985. 47(3): p. 239-240.

57. Gramsch, E., J. Throwe, and K. Lynn, Development of transmission positron moderators. Applied physics letters, 1987. 51(22): p. 1862-1864.

58. Zecca, A., et al., Procedures for conditioning W-and Ni-moderators for application in positron-scattering measurements. Nuclear Instruments and Methods in Physics Research Section B: Beam Interactions with Materials and Atoms, 2010. 268(5): p. 533-536.

59. Weng, H., et al., Tungsten mesh as positron transmission moderator in a monoenergetic positron beam. Nuclear Instruments and Methods in Physics Research Section B: Beam Interactions with Materials and Atoms, 2004. 225(3): p. 397-401.

60. Saito, F., et al., A high-efficiency positron moderator using electro-polished tungsten meshes. Applied surface science, 2002. 194(1-4): p. 13-15.

61. Williams, A., et al., Moderation and diffusion of positrons in tungsten meshes and foils. Journal of Applied Physics, 2015. 118(10): p. 105302.

62. Vehanen, A., et al., Improved slow-positron yield using a single crystal tungsten moderator. Applied Physics A, 1983. 32(3): p. 163-167.

63. Anwand, W., et al. Flash lamp annealing of tungsten surfaces marks a new way to optimized slow positron yields. in Journal of Physics: Conference Series. 2013. IOP Publishing.

64. Lee, K., et al., Practical usage of a W moderator for slow positron beam production. physica status solidi (a), 1996. 157(1): p. 93-98.

65. Reurings, F., et al., Compact positron beam for measurement of transmission moderator efficiencies and positron yields of encapsulated sources. Applied surface science, 2006. 252(9): p. 3154-3158.

66. Kulage, Z., et al., Characterization of the neutron flux energy spectrum at the Missouri University of Science and Technology Research Reactor (MSTR). Nuclear Engineering and Design, 2013. 261: p. 174-180.

67. Richardson, B., et al., Modeling and validation of approach to criticality and axial flux profile experiments at the Missouri S&T Reactor (MSTR). Nuclear Engineering and Design, 2012. 245: p. 55-61.

68. ALQahtani, M. and A.B. Alajo, Characterization of prompt neutron spectrum of the Missouri University of Science and Technology Reactor. Nuclear Engineering and Design, 2017. 320: p. 57-64.

69. Sinha, V., A. Srivastava, and H.K. Lee, A novel method for NDT applications using NXCT system at the Missouri University of Science & Technology. Nuclear Instruments and Methods in Physics Research Section A: Accelerators, Spectrometers, Detectors and Associated Equipment, 2014. 750: p. 43-55.

70. Akyurek, T., Tucker, L. P., Liu, X., & Usman, S. (2016). Portable spectroscopic fast neutron probe and 3He detector dead-time measurements. Progress in Nuclear Energy, 92, 15-21.

71. Shu, F., V. Ramakrishnan, and B.P. Schoenborn, Enhanced visibility of hydrogen atoms by neutron crystallography on fully deuterated myoglobin. Proceedings of the National Academy of Sciences, 2000. 97(8): p. 3872-3877.

72. Robinson, J., M. Hartman, and S. Reese, Design, construction and characterization of a prompt gamma activation analysis facility at the Oregon State University TRIGA® reactor. Journal of radioanalytical and nuclear chemistry, 2009. 283(2): p. 359-369.

73. Xu, Q., et al. Positron beam facility at Kyoto University Research Reactor. in Journal of Physics: Conference Series. 2014. IOP Publishing.

74. Turkoglu, D., et al., Characterization of a new external neutron beam facility at the Ohio State University. Journal of Radioanalytical and Nuclear Chemistry, 2011. 291(2): p. 321-327.

75. Craft, A.E., B.A. Hilton, and G.C. Papaioannou, Characterization of a neutron beam following reconfiguration of the Neutron Radiography Reactor (NRAD) core and addition of new fuel elements. Nuclear Engineering and Technology, 2016. 48(1): p. 200-210.

76. Bărbos, D., et al. The prompt gamma neutron activation analysis facility at ICN—Pitesti. in AIP Conference Proceedings. 2008. AIP.

77. Révay, Z., et al., Construction and characterization of the redesigned PGAA facility at The University of Texas at Austin. Nuclear Instruments and Methods in Physics Research Section A: Accelerators, Spectrometers, Detectors and Associated Equipment, 2007. 577(3): p. 611-618.

78. Morgan, S.W., J.C. King, and C.L. Pope, Beam characterization at the neutron radiography reactor. Nuclear Engineering and Design, 2013. 265: p. 639-653.

79. Bonzer, W. and C. Carroll, Safety Analysis Report for The Missouri University of Science and Technology Reactor-Revision 2. Rolla, MO, 2008.

80. Greenberg, R. R., Bode, P., & Fernandes, E. A. D. N. (2011). Neutron activation analysis: a primary method of measurement. Spectrochimica Acta Part B: Atomic Spectroscopy, 66(3-4), 193-241.

81. ASTM Standard E 720−16 (2016). Standard guide for selection and use of neutron sensors for determining neutron spectra employed in radiation-hardness testing of electronics. ASTM International, West Conshohocken.

82. ASTM Standard E 721−16 (2016). Standard guide for determining neutron energy spectra from neutron sensors for radiation-hardness testing of electronics. ASTM International, West Conshohocken.

83. McElroy WN, Berg S, Crockett T, Hawkins RG (1967) A computer-automated iterative method for neutron flux spectra determination by foil activation. Air Force Weapons Laboratory.

84. ASTM E262 − 13, 2013. Standard Test Method for Determining Thermal Neutron Reaction Rates and Thermal Neutron Fluence Rates by Radioactivation Techniques1. ASTM International, West Conshohocken, PA. www.astm.org.

85. Baum, E. M., Knox, H. D., & Miller, T. R. (2002). Nuclides and isotopes: chart of the nuclides. Schenectady, NY: KAPL.

86. ASTM Standard E 181−17 (2017). Standard test methods for detector calibration and analysis of radionuclides. ASTM International, West Conshohocken.

87. Fleming, R. F. (1982). Neutron self-shielding factors for simple geometries. International Journal of Applied Radiation and Isotopes, 33(11), 1263-1268.

88. Lindstrom, R. M., & Fleming, R. F. (2008). Neutron self-shielding factors for simple geometries, revisited. Chem. Anal, 53, 855-859.

89. Chadwick, M. B., Herman, M., Obložinský, P., Dunn, M. E., Danon, Y., Kahler, A. C., ... & Brewer, R. (2011). ENDF/B-VII. 1 nuclear data for science and technology: cross sections, covariances, fission product yields and decay data. Nuclear data sheets, 112(12), 2887-2996.

90. Hugenschmidt, C., et al., Positron experiments at the new positron beam facility NEPOMUC at FRM II. Physica status solidi (c), 2007. 4(10): p. 3947-3952.

91. Vehanen, A. and J. Mäkinen, Thin films for slow positron generation. Applied Physics A, 1985. 36(2): p. 97-101.

92. Zafar, N., et al., Experimentation with thin single crystal W foils as slow positron transmission mode moderators. Applied Physics A, 1988. 47(4): p. 409-412.

93. Jørgensen, L., et al., Evidence of very low-energy positron reflection off tungsten surfaces. Journal of Physics: Condensed Matter, 1998. 10(39): p. 8743.

94. Hugenschmidt, C., et al., Monoenergetic positron beam at the reactor based positron source at FRM-II. Nuclear Instruments and Methods in Physics Research Section B: Beam Interactions with Materials and Atoms, 2002. 192(1-2): p. 97-101.

95. Sinha, V., A.V. Avachat, and H.K. Lee, Design and development of a neutron/X-ray combined computed tomography system at Missouri S&T. Journal of Radioanalytical and Nuclear Chemistry, 2013. 296(2): p. 799-806.

VITA

Raed Atiah Alsulami received his bachelors of science degree in Computer Engineering in May 2009 from Umm Alqura University in Makkah, Saudi Arabia. He received his Master degree in May 2015 in Nuclear Engineering from Missouri University of Science and Technology. He received his PhD degree in July 2019 in Nuclear Engineering from Missouri University of Science and Technology. He continued working at the King Abdulaziz City for Science and Technology in Riyadh, Saudi Arabia as a researcher in Nuclear Science Research Institute.